BIOMICROFLUIDIC CHEMOEMITTER SYSTEMS: TOWARDS PHEROMONE COMMUNICATION

PROEFSCHRIFT

ter verkrijging van
de graad van doctor aan de Universiteit Twente,
op gezag van de rector magnificus,
prof. dr. H. Brinksma,
volgens besluit van het College voor Promoties
in het openbaar te verdedigen
op vrijdag 27 april 2012 om 16.45 uur

door

Nikolay Georgiev Dimov
geboren op 15 maart 1979
Kazanlak, Bulgarije

This dissertation has been approved by,

Promotor: Prof. dr. J.G.E. Gardeniers

To Zory

Acknowledgements

This thesis gradually evolved between January 2008 and December 2011 in the Mesoscale Chemical Systems group and the MESA+ Institute for Nanotechnology at the University of Twente. Herewith, I would like to acknowledge everyone who guided, supported and helped me along the way with bringing this work to a completion.

First and foremost, I would like to extend my gratitude to my advisor, Prof. Han Gardeniers, for giving me the unique opportunity to do research in your group, the academic freedom to express my own ideas, and the expert advices to realize these ideas. You have been a great advisor and a good person, who always keeps his office door open and finds time to indulge in inspiring discussions. I am sincerely grateful to you for helping me to improve intellectually and professionally during these four years.

The realization of the project would have been impossible without the financial support of the Sixth Framework Programme of the European Union through Information Society Technologies, FP6–IST 032276. I would like to thank deeply FP6 for their funding of the *i*CHEM project which allowed me to conduct my research.

Within the *i*CHEM project I was lucky to work with biology researchers from the CSIC group in Barcelona. Sincere gratitude to Prof. Angel Guerrero for welcoming me in his lab and for serving on my committee. Especially I would like to thank to Lourdes Muñoz, from his fantastic team, for running the GC-MS analysis during my whole study and for giving me insights on the work with moths. Special thank you goes to Gerard Carot Sans for sharing his knowledge on enzymes with me, and also for his patience and support.

I would like to acknowledge also the partners responsible for the development of the chemoreceiver, Marina Cole, Julian Gardner, Tim Pearce, Zoltan Racz for planting a true team spirit in the *i*CHEM. Thank you goes to Shannon Olsson and Linda Kuebler from the Neurobiology group of Bill Hansson in the Max Plank Institute of Jena.

Heartily thank you to my family, who brought me up as stubborn as it gets to persue my dreams, and to my brother for being there for me.

Finally, and above all, I would like to thank Zory for bearing with me through all our time together. You are the one, who taught me to distinguish between important and more important things in life. Your love and support mean more to me than anything else.

Contents

List of Figures

List of Tables

Glossary

Acetyl-CoA   An essential cofactor and carrier of acyl group, utilized in the enzymatic acetyl transfer reactions.

AFM   Atomic Force Microscopy

APTES   (3-Aminopropyl)triethoxysilane, organosilane used as an anchoring layer.

ATR-FTIR   Attenuated total reflection Fourier transform infrared spectroscopy

atf   Wax ester synthase/acyl coenzyme A: diacyglycerol acyltransferase

BE   Electron binding energy, presented in [eV]

BET   Surface area analysis technique; used to determine the specific surface area of powders, solids and granules, the values are expressed as $[m^2\ g^{-1}]$.

BSA   Bovine serum albumin is a protein with transport functions in the blood plasma. It has relatively good solubility in water (40 mg mL^{-1}) and molecular weight of 66 kDa.

CmAAT1   Recombinant enzyme alcohol acetyl transferase 1, originating from a plant *Cumis melo*

CNF   Carbon nanofiber

DITC   1,4-phenylene diisothiocyanate, implemented as a linker because of its thiocyanate groups in *para* orientation

DMF   *N,N*-dimethyl-formamide

DMSO   Dimethyl sulfoxide is a solvent that and cryoprotectant in cell culture. It readily passes through skin and latex gloves.

DRIE   Directed reactive ion etching is a microfabrication method utilizing accelerated gas ions.

DSS   Dextran sulfate sodium salt is a negatively charged polyelectrolyte. Among other functions its common use is to precipitate the nucleic acid from the volume of solution occupied by the polymer, thereby, increasing the effective probe concentration.

DVLO   A theory of interparticle interactions, named after its authors Derjaguin-Landau-Verwey-Overbeek, accorting to whom colloid stability is a balance of attractive van der Waals forces and repulsive electrical double-layer forces.

EAG   Electroantennography is an empirical method for measuring the voltage fluctuation between the tip and base of an insect antenna during stimulation. The effect is caused by electrical depolarisations of many olfactory neurons.

EDTA   Ethylene-diamine-tetraacetic acid; a chelating (two-pronged) molecule used to sequester most divalent (or trivalent) metal ions, such as calcium (Ca^{2+}) and magnesium (Mg^{2+}), copper (Cu^{2+}), nickel (Ni^{2+}), or iron (Fe^{2+} / Fe^{3+}).

EDSPA   [ethoxy(dimethyl)silyl]propylamine

F_{AD}   Adsorption coefficient used to describe the retention of enzyme on the agarose beads implemented in the current study.

FIA   Flow injection analysis

FID   Flame ionization detector, creates ions by combustion in the presence of fuel and oxygen; ion detection occurs via current measuring circuit.

FTIR   Fourier transform infrared spectroscopy

GA   Pentane-1,5-dial, a.k.a glutaraldehyde

GC   Gas chromatography, analytical method for separation based on differences in time of retention inside a chromatography column.

GC-MS   Gas chromatography coupled to mass spectrometry

His_6-EGFP Enhanced green fluorescent protein with tag of six consecutive histidines, in general the value in subscript denotes the number of residues.

HDMS   Hexamethyldisilazane, in the current work is used as adhesion reagent for photoresist.

HR-SEM   High resolution scanning electron microscope

ICP   Inductively coupled plasma

IDA	Iminodiacetic acid, is a molecule that can be used to chelate metal ions, as it is prone to bind metals with complex formation.
IMAC	Immobilized metal affinity chromatograpphy
IMER	Immobilized micro enzymatic reactor
I.S.	Internal standard; a compound that has a properties regarding the analytical method but at the same time is easily distinguishable from the analyte.
$\mathbf{K}_M$	Characteristic concentration of substrate at which the rate of an enzymatic reaction is half of the maximum. It is named after the two scientists, Michaelis and Menten, who invented a model for describing the kinetics of invertase.
$\mathbf{K}_D$	Deactivation constant of the enzyme after immobilization on the agarose beads
$\mathbf{k}_d$	Dissociation constant, serves as a criteria the affinity between ions, ligands and/or proteins. The rule of thumb is that the lower the value, the stronger the binding.
LbL	Layer-by-layer deposition technique
LPCVD	Low pressure chemical vapor deposition; used for nitride layer formation in the presence of dichlorosilane (SiH_2Cl_2) and amonia (NH_3).
MCT	Mercury-cadmium-telluride detector, typically with extremely low noise levels
MES	Monohydrate; buffer with pK_a value of 6.10 at 25°C, and effective range of pH 5.5–6.7
MEMS	Micro-electro-mechanical systems
MS	Mass spectrometry, a powerful analysis technique based on ion separation according to their mass to charge ratios (m/z)
MW	Molecular weight; measured in [Da]
NTA	N_α,N_α-*bis*(carboxymethyl)-L-lysine, chelating agent for transition metals
ODE	Ordinary differential equations
PAC	Poly(acrylic acid); negatively charged polyelectrolyte
PCR	Polymerase chain reaction, method for amplification and analysis of nucleotide sequences
PE	Polyelectrolyte is the generic name of multiple charged polymers
PEI	Poly(ethyleneimine); positively charged polyelectrolyte
PEM	Polyelectrolyte multilayer

PID	Proportional-integral derivative-controller; the action is proportional to the error (P), its change (D) and continues if residual error is present (I).
S65T	Enhanced green fluorescent protein with induced point mutation, serine exchanged for threonine at position 65 of the amino acid chain, see EGFP.
SDS-PAGE	Sodium dodecyl sulfate polyacrylamide - gel electrophoresis, common technic for protein separation by size based on the mobility of denatured protein; possible due to the fact that sodium dodecyl sulfate binds two aminoacids thus creating uniform electronegative charge around the protein.
SEM	Scanning electron microscopy
SPR	Surface plasmon resonance, on-gold measurement system for characterization of binding events; measured are shifts in the resonance from the natural frequency of surface electrons.
TEM	Transmission electron microscopy
TMSPEDA	N-[3-(trimethoxysilyl) propyl]ethylenediamine
Tris Cl	2-amino-2-hydroxymethyl-propane-1,3-diol chloride, a popular buffer with effective range pH 7.1–9.0; pK_a value of 8.06 at 25°C
XPS	X-ray Photoelectron Spectroscopy

1

Introduction

The overarching objective of the project presented in this book is to engineer functional equivalents of the molecular machinery comprising the synthesis of pheromone production and dissipation in a single animal. This will form the basis for a new branch of information technology for communicating chemicals over space and in time, using mixtures of infochemical ligands in precisely controlled ratios of concentration to encode multiple channels of information. Potentially, the long-term implementations of this approach will lead to novel implications for automatic identification and data capture, product labeling, search and rescue, data storage or even unexploded ordinance and mine localization.

In **Chapter 2** are introduced the definitions of allelochemicals, their immense variety and classification. Given are examples of the complex biological pathways for pheromone synthesis, dissipation and decoding, as these are inspirational for the design of the microfluidic devices. For the biosynthetic chemoemitter, a module-based design is chosen. An overview of the enzyme immobilization techniques inside a microreactor is presented together with approaches for kinetic studies on enzymes. Shortly discussed are the up-to-date pheromone-dissipation devices that are available to researchers. This chapter summarizes the necessity for a generic technological platform that will mediate unexplored forms of communication and will shift the paradigm of today entomology studies.

Chapter 3 presents a bottom-up-approach for surface modifications. Six types of modifications for metal affinity-based protein immobilization are generated on flat Si surfaces, after each stage of the processing the samples are characterized with X-ray photoelectron spectroscopy (XPS). Through broad and elemental analysis the number of binding sites for each of the modifications is evaluated. Furthermore, in the same chapter is studied the adsorption of (*Z,E*)-9,11-tetradecadienyl acetate, the main pheromone compound of *Spodoptera littoralis*, on untreated Si surface by using *in situ* Fourier transformation infrared spectroscopy (FTIR).

Implementation of the established protocols for surface modification inside silicon-glass microreactor is shown in **Chapter 4**. Explored are the abilities of the generated layers to immobilize

hexahistidine-tagged enhanced green fluorescent protein (His$_6$-EGFP). Discussed are the layer imperfections on the walls of the microchannel and the non-specific adsorption of the fluorescent protein. Preliminary activity tests are performed with immobilized recombinant enzyme alcohol acetyl transferase (CmAAT1). The findings lead to the conclusion that alternative protective coating and immobilization methods are required to solve partitioning.

Chapter 5 deals with the established bottle-necks by developing adsorption protective polyelectrolyte multilayer (PEM) and implementing functionalized agarose beads for the protein immobilization. Explored is the layer formation in terms of thickness as a function of: the molecular weight of the cation polymer building block; the pH during deposition; the time of incubation. Moreover the morphology and stability of the layers are investigated by atomic force microscopy and ellipsometry. In this chapter, the detailed microfabrication process of the silicon glass microreactor is conveyed. After implementation of the PEM inside the biomicroreactor its functionality is evaluated.

The optimal PEM protocol is implemented inside a silicon-glass microreactor, the last is described in **Chapter 6**. The conversion and stability of another enzyme, hexahistidine-tagged wax ester synthase/acyl coenzyme A: diacyglycerol acyltransferase (His$_6$ *atf*) is characterized in a long-term assay after immobilization on beads outside of the microreactor. The conversion inside the biomicroreactor is studied next and a numerical model is developed, that describes the experimental data. We adapt stable-state Michaelis-Menten kinetic equations that are modified in accordance with the partitioning and the stability of the enzyme. Based on this model and experimental data, the apparent kinetic parameters of the immobilized His$_6$ *atf* inside the microreactor are determined.

Chapter 7 describes the design, fabrication and implementation of the microevaporator as an artificial model of a pheromone gland. Also here is studied the passive evaporation of the main pheromone acetate from surfaces with different morphology under static conditions. Porous Si, "black" Si and carbon nanofibers (CNF) are considered as potential surface modification on the membrane of the microevaporator to enhance the release rate of pheromone at room temperature. The microevaporator is tested with both common solvents and the pheromone acetate. Finally the pertinence of the chemoemitter is proved in electroantennography (EAG) and behavioral studies on live male moths.

The concluding **Chapter 8** summarizes the content of this monograph and the findings reached throughout this work. A brief comparison is presented between the project aims and the obtained results. Discussed are several key aspects concerning infochemical communication, that can be useful for improvement of future work on the topic.

2

Literature review

Semiochemicals are chemical compounds that allow the transfer of information between or within the same species. These compounds are produced by one individual, i.e. the emitter, to elicit a behavioral and/or physiological response in another individual or group of individuals, i.e. the receiver. Often, the semiochemicals are air-borne and are transported within a stream of air, and they are typically molecules with relatively short chain-lengths and low molecular weight. However, a second type of compounds exists with large chains and high molecular weights - the so called contact semiochemicals. According to Nordlund and Lewis, the semiochemicals are subdivided into two major groups, pheromones and allelochemicals, depending on whether the interaction is intraspecific or interspecific, respectively (1).

The allelochemicals are divided in four groups depending on the emitter, receiver, and which party is beneficiary as a result of the communication, these are: allomones, kairomones, synomones, and apneumones. For instance, allomones evoke in the receiver a behavioral or physiological reaction adaptively favorable to the emitter, as formulated by Beth (2). These can be venoms, antibiotics and repellents originating from plants or animals. In contrast, the kairomones are semiochemicals that benefit the receiver. Synomones belong to the intraspecific semiochemicals meriting emitter and receiver. The last subgroup, apneumones, are semiochemicals derived from a non-living source, bringing advantages to the receiver. This classification has been summarized in the work of Nordlund and Lewis (1), and describes the types of semiochemicals in general. Intriguingly, a pheromone, that is taken out of the context of intraspecific communication can be listed under any of the above categories. One example would be the response of a wasp *Trichogramma pretiosum* towards a host moth *Mamestra brassicae*, the sex pheromone of which causes wasps to land shortly after take-off (3).

2.0.1 Pheromones and temporal coding

Pheromones have separate classification according to the reaction they trigger in an individual or group of individuals from the same species. In literature, dating back to the 70's, variations of behavioral response to pheromones are described such as: trail-marking or trail-following, causing alarm, dispersants, marking territoriality, synchronization, species aggregation, and sex pheromones (4; 5).

The interest towards pheromone communication back then has been related mostly to practical application of the pheromones in pest control because many of the pheromone-producing insects are pests (6). Equally important is the understanding of the pheromone communication, and of the mechanisms of encoding and decoding of semiochemical signals. By using lures with synthetic pheromones, entomologists and neurobiologists have gained advanced knowledge for many different insects. Yet, there is no answer to fundamental questions, like the one stated in the work of Carlson and Hansson, on the response of the male moths who are able to follow the rapid changes in stimulus intermittency when moving upwind in pheromone plumes in search of a calling female (7).

A step forward in that direction is taken by Christensen and coworkers, who in their study on the temporal structure of a physiological response to a stimulus in male *Manduca sexta*, discovered that the co-activity of neurons depended strongly on the physical context in which various stimuli were delivered. More importantly, different temporal patterns were evoked as the concentration of the same stimulus was varied. Additionally the patterns resulting from a blend could not be predicted from the responses to its constituent compounds. The neuron response was found clearly dependent on the time scale of the stimuli (8). In another moth *Heliothis virescens* subjected to a wind-tunnel assay, it was demonstrated how well single neurons followed the temporal characteristics of a natural odor plume. In the same work it is proved that the timeline of occurrence of a stimulus heavily influenced the temporal structure of the response to a stimulus. The time course of the projection neurons spike pattern of the *H. virescens*, had been significantly altered by both stimulus intensity and dynamics of the odor plume (9). To this end, it can be stated that the control of the stimuli blend, concentration and temporal pattern substantially influences the response of moths to olfactory acting pheromones.

Considering olfaction sensing in moths, many questions still remain unaddressed. For instance, it is still questionable whether the neuron responses to non-pheromone odors are similar to those already obtained for pheromones or is there some fine-scale differentiation their perception. Similarly important is the question of how likely it is for different coding mechanisms to evolve in various taxonomic divisions (11). Advances in the technology of plume generation and pheromone synthesis will only facilitate and accelerate the research towards answers to these questions. Moreover, the mechanisms and tools for synthesis and dissipation occurring in nature can become inspirational models towards novel design (Fig. 2.1). In the current work, this interconnection is realized by implementing the to-date knowledge on pheromone communication with top-notch microfabrication techniques. A successful design, however, relies on knowledge and consideration of the natural process related to pheromones and their sensing *in vivo*.

2.0.2   Pheromone - antennae interaction

Something that has puzzled both neurobiologists and entomologists for a long time is the natural process that occurs when a male insect encounters a pheromone plume. Walter Leal states in his work,
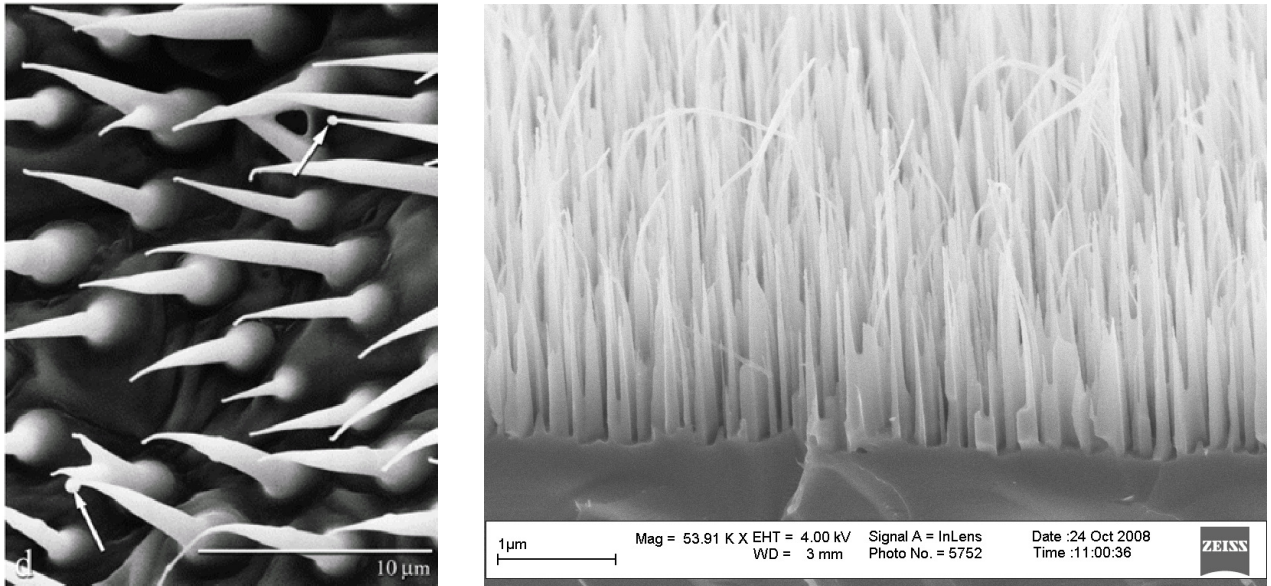
Figure 2.1: Inspiration by nature. SEM micrographs comparing the cuticular hair of *Helicoverpa zea* (courtesy of Raina *et al.* (10)) with droplets of pheromone forming on the top of cuticles, with a microfabricated surface covered with "black" silicon.

that insect antennae are biosensors *par excellence*, which integrate a controlled network of complex molecular interactions (12). The complexity comes from the fact that moths have to discriminate the pheromone, rarely a single compound, among other odors; and to sense scarce amounts of this blend while performing odor-oriented navigation. Such a flight requires dynamic processing of signal and fast inactivation to avoid saturation of receptors and consecutive loss of trace. In the same study, the pheromone signal is described as short bursts of high flux separated by zero flux; on *vs* off neuron firing. Murlis *et al.* suggest that, the average duration of spikes within puffs of pheromones occurs on the millisecond scale and becomes shorter as the male moth approaches to the source (13); therefore, detection must have the same time scale or shorter, otherwise moths would have been extinct. Despite the growing body of literature about encoding, as Olsson and coworkers point out (14), for gaining insight in the neurological responses of insects to semiochemicals it requires novel technological platforms for olfactory experiments and dissipation of volatiles in particular.

2.0.3 *In vivo* pheromone synthesis and dissipation

According to Ma and Ramaswamy (11), sex pheromone gland cells can be individual cells on the body or clusters of cells forming glandular tissue. In the different species the cells are scattered on the head, thorax, abdomen and even antennae. These cells and glandular tissue have been studied by Noirot and Quenedey, who found that there are three types of cells, depending on the route followed by the pheromonal secretions through the cuticular barrier (15).

First are the Class I cells, usually adjacent to the perforated outer epicuticule or cuticulin. The matrix of the cuticle is claimed to be overlaying Class I cells, which host enzymes that convert

secretions occurring from underlying glandular cells and diffusing through (16).These cells contain the lamellae form of smooth endoplasmic reticulum characteristic for passive transport, a.k.a. non-protein secreting system.

Next, Class II cells, are not in direct contact with the cuticle and their secretions pass through Class I to reach the cuticle and beyond. Both classes aggregate to form an extracellular reservoir to function as a secretion storage. Some studies claim Class II cells are associated with the cycling hydrocarbon from pools in the hemolymph to the cuticle; in some species lipid droplets are found that likely contain pheromone precursors (11; 17; 18).

Last, Class III constitutes a group of cells connected to the cuticle by a cuticular duct, their main function is to deliver secretions to the outside. The cuticular duct has an extracellular receiving canal, bounded by sponge-like microvilli where secretions are stored, and also a conducting canal in touch with the outer cells. In addition, Class III cells are reported to contain large Golgi complexes and abundant secretory vessels as well as an abundant system of endoplasmic reticulum (smooth and rough). However, their role in the synthesis and release of the pheromonal secretion is yet to be deciphered (11). The biosynthetic pathway of pheromones is too complex to be mimicked entirely; nevertheless, the concept for compartmentalization can be implemented in MEMS modules for multienzyme catalysis towards pheromone production. Moreover, in a study by Lee *et al* designed and implemented a microreactor that was capable of bio catalysis in three consecutive steps: invertase–glucose oxidase–soybean peroxidase system was used to yield H_2O_2 from glucose (19).

Looking back at the natural dissipation strategies in correlation with the three types, the cells can be ordered in pheromonal glands, the organs related to the synthesis and secretion of volatiles as is stated earlier, or can be scattered. Intriguingly, the different species exploit pheromonal glands with various architectures, not all of which are understood. However, some parts of the gland architecture can be reproduced by MEMS design. For instance, the gland of the leiodid beetle, *Speonomous hydrophilus*, has a porous plate consisting of an epicuticular layer perforated by tiny pores, located at the opening of the gland. The intricate cuticular structures are also termed pseudomembranes, supposedly they have the same function as a secretion apparatus in a Class III cell (20). Another interesting example of pheromone dissipation is described by Zhu *et al.* in the female psychid bagworm moth, who secretes sex pheromone on to deciduous hairs on its thorax. These pheromone laden hairs attracts the males for courtship as the volatiles enter a wind stream (21).

From the studies above, it can be concluded that the general process entails secretion of the pheromone blend to the outside, then evaporation from the enhanced surface of the pheromone gland and passive transportation downstream from an emitter to a receiver. Similar strategy is implemented in the MEMS based system developed in this thesis; the pheromone is synthesized from a precursor in a biomicroreactor module, then it is pressure driven to the surface of a microevaporator, these two components comprise the further described chemoemitter.

2.1 Intercepting MEMS with entomology

Scientists with multidisciplinary background have concentrated their efforts towards microfluidics and MEMS based research after discovering the potential of miniaturization. Microfluidics have revolutionized studies in Proteomics (22), Genomics (23), single cell measurements and manipulations (24; 25), tissue regeneration on nanopatterned of surfaces (26) , even lung function regeneration on a chip (27), point of care diagnostics and analytical techniques (28; 29). However, these advances are not yet comprehensive among all biological studies. Even though the current technology has a potential of great magnitude, in many research fields the frontiers are not yet reached and archaic methodology is still in use. One such gap is found in the sphere of entomology: MEMS are widely underutilized when it comes to infochemical communication. In the current work we present a novel microfluidic platform for biocatalytic pheromone synthesis and controlled dissipation, that will facilitate entomology studies and will become a solid base for the starting field of the infochemical communication. Several key points are addressed as the most important for the design and investigation of this microfluidic platform.

2.1.1 Enzyme immobilization

The merits of enzyme immobilization have been explored in many high quality research studies in the last decades. Excellent overview on enzyme immobilization strategies was presented in the book authored by Cao (30). Other apt sources are available on the numerous immobilization approaches that follow the development and implementation throughout the years for analytical (31), biotechnological (32) and other more general purposes (33; 34). Independently of the favored immobilization strategy, most of the methods target similar usability goals such as: increased functional stability; reaction specificity; and last but not least, multi-time usage of the immobilized enzymatic reactor or microreactor (35). Currently we focus on controlled immobilization approaches through the interaction of histidine with Ni^{2+} chelated in nitrilotriacetic acid (NTA).

Pioneered by Hochuli, the polyhistidine tag, is perhaps the most popular genetically encoded affinity tag (36). It is well-known for its facile application and reversibility of binding; as NTA or iminodiacetic acid (IDA) can functionalize the surface of a support, consecutively a treatment with a solution of a transition metal ions (37) leads to formation of complexes and a surface suitable for immobilization of a His_n tagged protein (n = 6 to 12). This immobilization strategy is broadly implemented for reversible capture and purification of proteins, which can be re-solubilized with imidazole. This approach is called immobilized metal affinity chromatography (IMAC) (33)-(40). The small tag allows flexibility of the protein design, as it can be located at either the N-terminus or C-terminus as well as at exposed loops (33; 41). A disadvantage is, that the binding of histidine to NTA/Ni^{2+} is characterized by weak interaction with K_d (desorption constant) in the micromolar range (1-10 μM). In spite of that, the immobilization system based on IMAC can be used for sensors,

catalysis and analysis inside microreactors (38; 39). According to Wong *et al.* (33) one possibility to circumvent the relatively high value of K_d, and to achieve stronger bond formation, is to increase the number of histidines in the tag concomitantly with the number of binding sites on the carrier. The popularity of the method is justified by all the above stated arguments but also by the great number of commercially available plasmids that contain the polyhistidine tag and also IMAC platforms for purification or microrarray analysis.

2.1.2   Biomicroreactors for kinetic measurements

This section focuses on fundamental continuous flow approaches to determine the kinetic parameters of enzymes immobilized inside microreactors. The first reported flow injection analysis (FIA) microreactors with integrated enzyme, glucose oxidase, on porous Si, were intensively studied in the early 90's by Laurell *et al*, who developed a porous Si immobilized enzyme microreactor system for continuous glucose determination based on absorbance measurements (42; 43). In a later research, Seong and Crooks implemented a PDMS packed-bead microreactor and fluorescence measurements for studying the kinetics of immobilized horse radish peroxidase and β-galactosidase on microbeads, functionalized with aminocaproyl spacer coupled to biotin (44).

The classical approach for characterizing immobilized enzyme is to vary the concentration of substrates, inhibitors and co-enzymes with consecutive determination of the product formation. Knowing the amount of immobilized enzyme and using the collected data points, functions can be fitted and the type of kinetics, reaction mechanisms and inhibition as well as the related parameters can be established. Significant difference from the classical enzymatic studies is that for the characterization of immobilized enzyme in continuous flow conditions the kinetic properties can be determined through varying the flow rate instead of changing the concentration of substrates. The classical approach is also applicable as proved in the work of Chen and coworkers who change the concentrations of the flow-through fractions of acetylthiocholine, by using an automated injection method, to determine the kinetic parameters of the immobilized enzyme acetylcholine esterase (45). However, another approach is also possible based on the flow-through rate and conversion (46).

Fundamental research had been conducted by Lilly-Hornby, in their work they described a method to achieve the enzyme kinetics in a flow-through microreactor system without varying the concentration of substrate (46). As one of the conclusions from that work was that the rate of reaction was affected by rate of diffusion to the active site of the enzyme and away. In the same study, Lilly-Hornby proved that the $K_M{}^{app}$ for the cellulose-ficin was dependent on the flow rate through the packed column. Independently, in a later study on β-galactosidase and horse radish peroxidase the validity of the model was demonstrated when utilizing streptavidin-coated microbeads trapped inside a microreactor (44). The process of conversion of 6,8-difluoro-4-methylumbelliferyl phosphate by alkaline phosphatase in a microreactor was later explored by Kerby *et al.* They demonstrated convincingly that high substrate conversion limits the Lilly-Hornby approach as the mass transfer

to the immobilized enzyme on glass beads became more complex (47). Another example of the flow dependent enzyme kinetics was found for glucose oxidase immobilized on exchanger resin inside a packed-bed reactor; in that case the value of K_M for the immobilized enzyme decreased when flow-rate through the column increased (48), which is a direct consequence of the depletion of the diffusion layer. In principle, if diffusion constants are known, the apparent kinetics can be modeled, e.g. by numerical methods (49). Although, the flow-through approach might not be the optimal pathway for determination of the immobilized enzyme kinetics, it would lead to better understanding of the system under operational conditions.

2.1.3 Devices for pheromone release and communication

Until recently, the release of chemical stimuli in wind tunnel experiments on insect flight behavior relied mainly on the passive evaporation of volatile chemicals from a lure, usually made from a filter paper or a rubber septum (50). A key drawback of the approach is that only the initial dose applied to these lures is specified, while other factors such as chemical affinity to the substrate used, the kind and amount of solvent in application, temperature, airflow above the lure and time of evaporation are often overlooked. Therefore, establishing compound ratios and their emission rates is cumbersome, time consuming and poorly reproducible, especially for low concentrations of volatiles released from such traditional lures. The main aim of the described study was to tackle such problems. The microevaporator described in this book is a tangible solution to some of the key underlying problems. It controls the exact composition of the pheromone solution used during an experiment. This allows quick, easy and timely definition of the content of the evaporated plumes in terms of ratiometrical and temporal coding.

In the same class of devices the closest would be an evaporator with ultrasound. Even though ultrasonic devices allow to control the release of volatiles, it is often the case that insects are sensitive to the ultrasound emanating from the device. Some species respond to ultrasound within the working frequency range of the devices during mate orientation and courtship (51; 52). To circumvent such source-related side effects it is necessary to exchange the piezo in order to have the system adjusted to an insect species (53).

Another alternative system is the one for multicomponent blend formation suggested by Olsson and Kuebler. However, their method is based on too many control parameters, that could result in experimental errors. An additional drawback is that each change of the evaporated compounds requires time-consuming calibration (14). Building upon this fundamental piece of work, it is possible to use the same approach for the design of the microevaporator, especially if the evaporated compounds are temperature sensitive. When this is the case, evaporation is based on the pressure differences and is controlled by adjusting the vapor pressure for the 8 odours. The process is described in more detail by Cometto-Muniz (54). In contrast, with the microevaporator at hand the parameters that have to be adjusted are: the temperature of the device, from a controller; the flow rates of the pheromone or

other odor, from a syringe pump; optionally, the air flow above the membrane by varying the amount of purging gas in the headspace. Naturally, if the number of odors is higher there will be more flow rates to control, however the process could be automated.

2.2　Summary of the literature review

The literature review touched upon the classification of the vast number of naturally occurring pheromone compounds and the rich variety of chemical communication strategies among insect species. Despite the boost of knowledge in entomology, there are still many pending questions, and research utilizing this knowledge can trigger an adequate response in the technological development of new devices towards more efficient experimental ideas. Having looked at the current stage of immobilization of enzymes inside microreactors through IMAC the merits of their implementation was considered. Next were argued the benefits, drawbacks, and need for development of a novel microfluidic platform for evaporation.

In brief, the main goal of the current study is the conceptual design and realization of a microfluidic device mimicking the emitter of a pheromone in nature and the pheromone synthesis of a single animal. Such an ambitious project is only possible with the solid base from two completely opposite research topics that were briefly introduced in this literature review. As a result of their combination the chemoemitter studied in this monograph evolves, which will have an impact on entomology, by suggesting novel microfluidic platforms for communication through volatiles in addition to the cornerstone setting for studies on chemical communication in air.

3

Surface modifications for immobilization on SiO$_2$

Enzyme immobilization has been heavily investigated throughout the last few decades and multiple strategies are implemented in practice. Thus, the major concern is not how to immobilize enzymes, but how to design the performance of the immobilized enzyme in an integrated system to meet certain biocatalytic requirements (30). In the context of a biomicroreactor surface functionalization, the methods can be grouped in two main categories: top-down and bottom-up approaches.

Top-down approaches are based on the hypothesis that the known properties of the enzyme are compatible with the immobilization strategy. In this case different modifications are introduced in the enzyme structure to match already existing immobilization chemistry on a support. Optimization of the immobilization strategy would require iterative immobilization attempts of enzymes with various structure modifications.

Alternatively, bottom-up approaches first explore the unknowns, then modifications follow a gradual development of the immobilization strategy with detailed analysis after completion of each stage. Again the purpose is immobilization of the enzyme, however, its structure remains unaltered during optimization of the immobilization process. The bottom-up approach is also referred to as a data driven processing, when an interpretation emerges from the experimental results. Above all, it is crucial to have as much data as possible about the surface modifications before the biocatalyst immobilization.

Both approaches are oriented towards immobilization of an enzyme. However, a bottom-up strategy is considered more suitable for the silicone-glass microreactor. Therefore, it is essential to learn as much as possible about the layer modifications on polished Si pieces and on later stage implement the established protocols for the enzyme immobilization on the walls of a microreactor.

Another functionality issue that we address in the current chapter is adsorption of the product on non-treated Si surface. The adsorption depends on all system components as well as on experimental parameters. In general, these are surface properties (geometry, roughness, porosity, charge or polarity), solvents (protic, aprotic, polar, non-polar), adsorbent characteristics (hydrophilic, hydrophobic,

dipole moment, active groups) (55). The substrate of the enzyme is a polar molecule and so is the product; on the other hand, the Silicon surface is also polar due to the different electronegativity between O and Si atoms in the topmost oxide layer. It contains two types of hydroxyl groups: isolated and hydrogen-bonded, interacting in pairs.

After studying the absorption of fatty acid methyl esters from benzene on a completely hydroxylated surface, Mills (56) proved that the isolated groups are the main absorption centers. Same tendency is described for water and aliphatic alcohols in the work of Dabrowski *et al* (57). According to them, for silica surfaces, interactions during adsorption would be mainly caused by the free silanol groups with a maximum of 3-4 per nm^2.

The present investigation aims to achieve a new protocol for surface modification and immobilization of recombinant hexahistidine-tagged enzyme, alcohol acetyl transferase 1 (His$_6$ CmAAT1), originating from a plant, *Cumis melo*. This chapter describes the process of obtaining the stoichometry of six surface modifications by chemical analysis based on XPS measurements. Further, we address the absorption of (*Z,E*)-9,11-tetradecadienyl acetate, the pheromone, via *in situ* FTIR measurements.

3.1   Materials and Methods

3.1.1   Surface modifications on silicon

Initially, the coatings are generated on flat one-side polished silicon pieces (7x7 mm).

Activation The surface of the Si pieces is covered by naturally occurring protective oxide layer, that consists of siloxane bonds which are stable and relatively inert, not likely to step in to reaction readily. Therefore, to activate the surface, the Si pieces are placed in a glass beaker and incubated for 25 minutes in Piranha solution, which is a mixture of H$_2$SO$_4$ and H$_2$O$_2$ (3:1 vol). It is well-known that Piranha is a strong oxidizing agent and reacts vigorously with organic components! The hydroxyl radicals from the solution brake the siloxane bonds to form silanol groups on the surface. To wash the excess acid and peroxide away, the pieces are rinsed with copious amount of water for 25 minutes. Because it is important to have a dry surface for the silanization step the pieces are thoroughly dried by N$_2$ flow followed by an EtOH flush and are finally dried for one hour at 150°C.

Silane anchoring. For the silanization process it is chosen to work from anhyndrous toluene solution instead of using gaseous deposition. Several concentrations are tested to reduce the choice down to three concentrations: 1.5% for the APTES and the EDSPA, and 4% for the TMSPEDA. The dried Si pieces are transferred to separate vials containing the silanization solutions, and incubated inside at room temperature for 4 hours. Afterwards the solutions are decanted and anh. EtOH is pipetted into the vials, to flush the non-reacted organosilanes. The pieces are further N$_2$ flow dried.

To cross-link the TMSPEDA and also APTES molecules, the samples are heated at 150°C overnight. The third modification, utilizing EDSPA, is not heat treated after the silanization step.

Introducing a glutaraldehyde spacer. The dry surfaces are incubated in 5% GA in 0.5 M NaHCO$_3$ (pH8.5) for two hours at room temperature. Afterwards the surfaces are N$_2$ dried.

Coupling diisothiocianyte spacer. The other spacer variation, DITC, is introduced as 0.1% (w/v) solution in anh. toluene. The silanized surfaces are kept for 4 h at 60°C. Finally the surfaces are rinsed with anh. EtOH.

Carrier binding and charging with Ni^{2+}. The carrier molecule NTA has a terminal, primary amine that binds to the aldehyde groups originating from GA, as well as to the isothiocyanate of the DITC. This process is conducted from a solution of 0.5% NTA in MilliQ, pH8, adjusted with NaHCO$_3$. The surfaces are incubated for 2 h at room temperature; then rinsed with EtOH, and dried with N$_2$.

Next, 400 mM NiSO$_4$ at pH6.5 is incubated for 20 minutes at room temperature. The excess solution is flushed out with 10 mM Tris-Cl (pH 7.3) buffer. At this stage the samples are ready for surface characterization.

3.1.2 X-ray photoelectron spectroscopy of the functionalized Si samples

After each modification step a silicon sample (7x7 mm) is studied to evaluate the layer formation by measuring the stoichiometry on the surface; for each sample three measurements are taken at different spots. The spectra from a total 22 samples are measured with Quantera SXM (scanning XPS microprobe) from Physical Electronics, using an X-ray source Al Kα, monochromatic at 1486.6 eV.

The distance from the sample plate, auto-Z height, is determined to be 24.41 mm and higher, it depends on sample position, and the measurement settings (100μm^2, 25W, 15keV) of the X-ray beam at the standard beam-input and detector input angle of 45°. Auto-Z is necessary for alignment of the surface of the sample with the foci of X-ray source and electron analyzer.

For reduction of the measured data Compass for XPS control, Multipak v.8.0 is used. Fitting of the measured spectra is done after shifting it with respect to known reference binding energies. In the current study that is aliphatic carbon C1s at 284.8 eV.

3.1.3 *In situ* FTIR measurements of the adsorption of (Z,E)-9,11-C14:OAc

Fourier Transformance Infrared Spectroscopy is performed in a micromachined flow-through cell consisting of a Si chip (0.5 x 20 x 50 mm) with 54.7° on the shorter sidewalls, a result of wet anisotropic etching. On the Si chip a PDMS gasket (3.5 mm) is positioned to define the sidewalls and volume (1700 μL) of the chamber. The PDMS is pressed by a holder that serves as the lid of the cell, and as a holder for the inlet and outlet capillaries. The holder is mounted on the mirror rack of the FTIR and placed inside the sample compartment of an infrared spectrometer (Bruker Tensor 27, Ettingen, Germany) equipped with MCT detector.

The spectra are recorded at room temperature (294 K). For each infrared spectrum 128 scans at a resolution of 4 cm^{-1} are averaged. First is measured the spectrum of the clean dry surface, as a background. Next, the phases of interest are measured under stop-flow conditions in sequence: the pure dienyl acetate; followed by copious amount of water, the cell is dried for 26 h by purging N$_2$ in the sample compartment then spectra are collected; 5 chamber volumes of reactive buffer-solution (aq. soln. 10 mM Tris-Cl, 4% DMSO and 10% Glycerol) are introduced; consecutively dried for 22 h and measured; lastly, 5 chamber volumes of Ethyl acetate are flown through the cell, then dried with N$_2$ for 19 h and measuring.

3.2   Results and Discussion

XPS spectra are collected from the six variations of surface modification, using three different organosilanes in combination with two linker molecules, in order to show all elements with an abundance higher than 1%. Additionally, homogeneity and element content are studied by performing three high-definition element spectra scans per sample. To demonstrate the layer formation, spectra are collected after each stage of the modification process. The results are grouped in accordance to their stage of deposition and functionality. To estimate the properties of each surface, the empirical data is analyzed in the context of the predicted data from hypothetical models (Fig.3.1). The results from the survey spectra are presented and elemental analysis is performed based on the high resolution spectra.

Additionally, adsorption of the (*Z,E*)-9,11-tetradecadienyl acetate is studied to evaluate the significance of interaction with non-treated Si surfaces.

3.2.1   Organosilane anchoring layer

It is important to know the characteristics of the deposited layer in order to evaluate which of the organosilanes and procedures is the most suitable for implementation inside the microreactor. Three molecules are chosen for the anchoring to the surface of the Si (i.e. APTES, TMSPEDA, EDSPA) with diverse chemical structures. These silanization agents bind covalently via siloxane bonds to the hydroxyl groups on the Si surface thus providing a stable initial layer (Fig. 3.1, *Stage I*).

Though, single layer formation is considered for calculating the theoretical ratios of elements, achieving a single layer is not crucial as long as the process is reproducible and well defined. The three organosilanes are chosen because of variations in their hydrolysis rates; with the increase in the size of the alkoxy substituent the silanes become more resistant to hydrolysis (72).
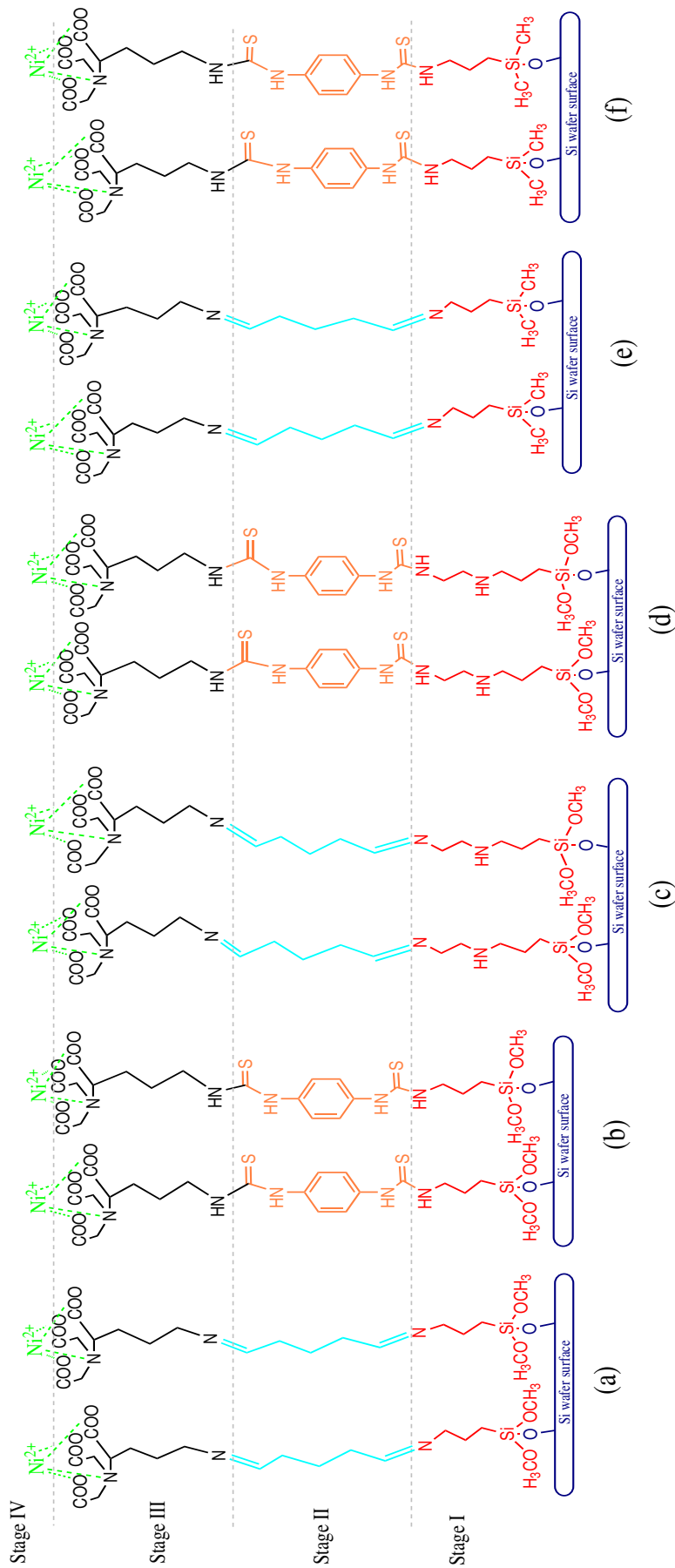
Figure 3.1: Representation of the surface modifications on oxidized Si. The variations considered in the current chapter are depicted from left to right: (**a**) (3-Aminopropyl)triethoxysilane coupled via glutaraldehyde to N_α,N_α-*bis*(carboxymethyl)-L-lysine with chelated nickel (APTES/GA/NTA/Ni²⁺); (**b**) (3-Aminopropyl)triethoxysilane connected by 1,4-diisothiocyanate to N_α,N_α-*bis*(carboxymethyl)-L-lysine that chelates nickel (APTES/DITC/NTA/Ni²⁺); and the configuration with the other organosilane (**c**) N-[3-(trimethoxysilyl) propyl]ethylenediamine with glutaraldehyde (TMSPEDA/GA/NTA/Ni²⁺); (**d**) TMSPEDA/DITC/NTA/Ni²⁺; (**e**) [ethoxy(dimethyl)silyl]propylamine in combination with glutaraldehyde (EDSPA/GA/NTA/Ni²⁺); (**f**) EDSPA/DITC/NTA/Ni²⁺. The grey horizontal lines divide between the four main stages of modification.

15

Despite of these differences, the three agents have a terminal amine that is further used in the layer formation. In addition to the substituent groups, another parameter influencing the thickness of this initial layer, is the number of atoms found in the backbone of the organosilanes. However, the effect of the length of the alkyl substitute could diminish, if the anchored molecules are oriented randomly to the wafer surface; only perpendicular orientation is considered in the models represented in Fig. 3.1. Equally valid, the silanes can lay flat on the surface of the substrate, thus resulting in higher coverage and thinner layer, than in the case of molecules perpendicularly oriented towards the surface.

Another feature of the silanes is that more than one bond can occur in lateral direction due to the cross-linking between the silane molecules. One example of how the chemical structure can influence the layer formation is the case of EDSPA (e, f): because there is no possibility for the molecules to cross-link, only dimerization can occur between two EDSPA molecules in solution. This would prevent attachment to the wafer surface and formation of a stable coating. Therefore, the EDSPA is most likely to build a monolayer on the Si wafer surface.

To analyse further the coating properties in terms of coverage and cross-linking for each of the organosilanes, we compare the theoretical content of N from the model to its counterpart from the elemental analysis obtained from the XPS survey spectra. By making several estimations in the model and recalculations of the experimental data, explained further, the actual ratios of elements are determined for each of the organosilanes after deposition.

Table 3.1: **Elemental ratios on the Si surface at *Stage I*.** Element spectra scans on C, N, O and Si (at. %) are measured from the Si wafer samples with covalently bonded organosilanes layer. The control, blank sample, is further used in the calculation of the C contents originating from the silanization.

Organosilane	C1s	N1s	O1s	Si2p
blank Si	6.1 ± 0.9	—	64.4 ± 0.4	29.6 ± 0.6
APTES	17.0 ± 3.3	0.8 ± 0.4	55.5 ± 2.8	26.7 ± 0.9
TMSPEDA	14.4 ± 0.9	2.1 ± 0.1	56.6 ± 0.7	26.7 ± 0.1
EDSPA	15.9 ± 1.0	0.6 ± 0.1	56.8 ± 0.7	26.2 ± 0.5

The results from the analysis of the XPS from *Stage I*, the formation of the anchoring layer, are summarized in Table 3.1. As C is the most common contaminant of XPS samples, even under Ar atmosphere it is hard to avoid contaminations on the samples. Therefore, the measured C content (6.07%) on a blank Si wafer is considered as contaminant, and is subtracted from the rest of measured values of C1s for the three organosilanes, only afterwards the residue C is addressed as a direct consequence of the layer deposition.

Based on the survey spectra, it is established that SiO_2 is completely described by the measured peak area at BE 103.7 eV, coming from SiO_2. Thereafter, the determined silicon (from the Si 2p) is multiplied by factor 2, coming from the ratio of the O to Si in the molecule of SiO_2, and it is then

substituted from the total amount of oxygen measured at O 1s. Thus, the recalculated amount of O originates only from the organosilane layer.

The sum of the corrected C and O contents, plus the measured N, give the approximation of the elements in the anchoring layer. Next, the ratio of the measured N1s versus the sum of elements is determined. Knowing the shift in those ratios will allow precise characterization of the layers. The cross linking of the APTES, for instance, leads to elimination of ethanol that would reduce the total number of atoms and result in a different ratio. Hence, the ratio from the elemental analysis is used as a criteria to evaluate whether the layer is cross-linked and to what extent.

In the case of the APTES anchoring layer, the theoretical value of N for a single bonded molecule coincides with the measured ratio within the upper value of the standard deviation for the N1s (see Appendix A for details). The APTES modified surface has a ratio for N:C $(0.8 \pm 0.4)/13.9 = 1:11.7$ comparable to 1:12 which is the theoretical content of N in the molecule of APTES, when a single bond is formed with a silanol group from the wafer without cross-linking in lateral direction. Hence, it is proved that the APTES layer is not cross-linked in lateral direction. Additionally, when the lowest N1s value is considered, it can be stated that the coverage is not complete or the coating is not homogeneous. That is deduced from the XPS measured ratio which is lower than the theoretically expected for a monolayer. In summary, for the APTES anchoring layer it can be concluded that, it is not completely covering the Si surface but is most likely assembled in a monolayer with no cross-link formation in lateral direction.

Identical calculations are done for the TMSPEDA; two nitrogens are measured per 12.8 atoms or 15.6 % (at.), in comparison to the theoretical 16.7 % N per molecule of TMSPEDA. This value is calculated per molecule with a single siloxane bond to the surface without considering cross links to other molecules. The measured ratio is lower than the theoretical for N, however, it is higher in comparison to the determined APTES which can be expected as the TMSPEDA has extra nitrogen. The coverage on the surface is not completely homogeneous, judging from the comparison between the theoretical and measured ratios.

Having a single ethoxy group capable to hydrolysis, the EDSPA can bind via a single bond to the Si surface in which case the theoretical content of N is 12.5 % (at.). In contrast, the measured content is 3.7 % (at.) from N1s, that is 3 times less than expected. For this reason, it can be stated that only one third of the surface is covered by the monolayer. In comparison to the other two organosilanes, at this first anchoring stage, the EDSPA has the least coverage.

In summary, after the silanization stage, elemental analyses showed that APTES and TMSPEDA have a surface coverage close to the theoretical model with a tendency of non-complete coating, while

EDSPA covers only 1/3 of the surface of the wafer.

3.2.2 Coupling linkers to the anchoring layer

The surface modification continued with the coupling of diisothiocyanate (DITC) and glutaraldehyde (GA) to the silanized surface. DITC is chosen for its affinity and readiness to react with amines; the molecule has its two functional groups in *para* orientation to benzene. Hence, DITC provides both the necessary distance from the surface and a reactive site for the modification with the nitrilotriacetic acid (NTA).

On the other hand GA is chosen as a linker in this study as an alternative, to compensate for the non-complete surface coverage at the initial silanization stage. As it is known from literature (59), the GA in basic conditions is found in polymeric form, that tends to organize in a mesh-like structure which is abundant in aldehyde groups available to react with the amine terminated NTA. The primary amine forms either a Schiff base with an aldehyde that remains stable to hydrolysis due to the conjugated C-C bond (68).

(a)

TMSPEDA/GA
C, 63.16; N, 10.03; O, 21.05; Si, 5.26

(b)

TMSPEDA/DITC
C, 60; N, 16;
O, 12; S, 8; Si, 4
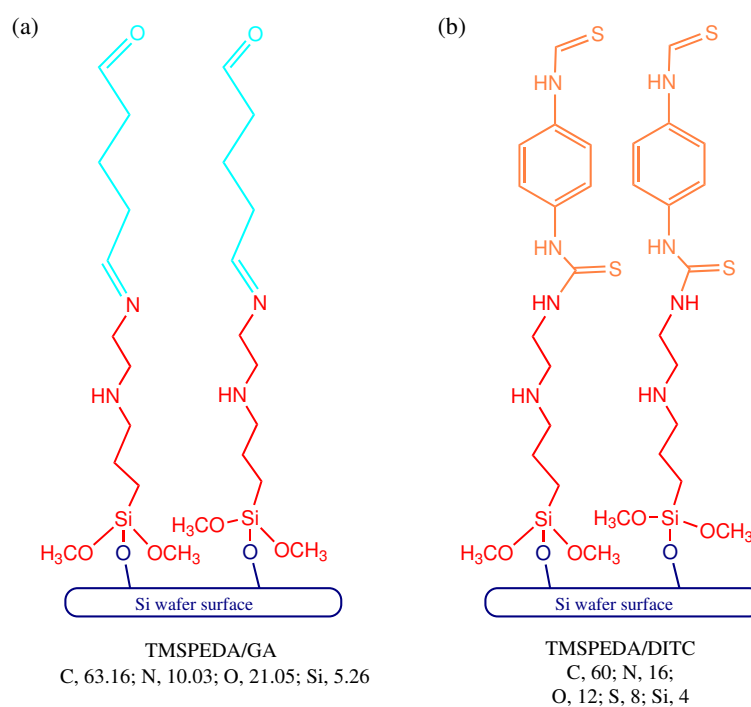
Figure 3.2: **Schematic representation of the silicon wafer surface with anchored TMSPEDA:** (a) coupled to glutaraldehyde (GA); (b) coupled to diisothiocyanate (DITC), and the elemental analysis for the two molecules that are immobilized via a single bond. Hydrogen is not detected in the XPS, therefore it is not considered in the calculation of element spectra either.

For *Stage II* (Fig. 3.2) the theoretical ratios are calculated based on the findings, that organosilanes are bond to the surface via a single bond, and no cross-linking occurred between the silanes in lateral direction. Additionally, it is assumed that one linker molecule binds to a single anchoring

molecule. The ratios of C:N for each of the surface modifications are calculated based on the results shown in Table 3.2. Further, these are compared to the theoretically predicted ratios.

The general trend is that the measured data differ from the predicted values for all six surface modifications, Figure 3.3. It is observed that the measured amount of the N is lower in comparison to the theoretical amount as the ratio of C:N in the former is larger. Equally valid, the content of C is higher in the XPS measured results and this is the reason for the discrepancy. The most significant difference is in the case of the EDSPA coupled to GA for which the measured ratio is twice the theoretical one. This means a simultaneous increase in C and a decrease in N. Another strongly exceeding C content over the theoretical one is seen for the APTES/GA sample. One interpretation can be that the deposition of polymeric GA is the major constituent of the layer, which is in agreement with the findings by Richards and Knowles in their work on protein cross-linking.(69)

Table 3.2: Element spectra scans on C, N, O and Si (At. %) at _Stage II_. Measured are performed on the Si wafer samples after silanization and coupling to the linkers. The control, blank sample is used to subtract for the background C contamination.

Organosilane	Linker	C1s	N1s	O1s	Si2p
None	None	6.0 ± 0.9	—	64.4 ± 0.4	29.6 ± 0.6
APTES	GA	20.6 ± 1.7	0.7 ± 0.1	52.7 ± 1.4	26.0 ± 0.4
APTES	DITC	12.5 ± 2.2	0.9 ± 0.2	58.8 ± 1.6	27.8 ± 0.8
TMSPEDA	GA	25.4 ± 4.9	2.5 ± 0.9	49.1 ± 3.9	23.1 ± 1.9
TMSPEDA	DITC	13.9 ± 1.3	1.8 ± 0.4	57.3 ± 1.1	27.0 ± 0.5
EDSPA	GA	18.6 ± 3.4	0.6 ± 0.1	55.2 ± 2.4	25.6 ± 1.1
EDSPA	DITC	9.8 ± 2.3	0.5 ± 0.2	61.5 ± 1.7	28.2 ± 0.8

One would expect to observe similar strongly pronounced discrepancy in C:N ratio for the last sample with GA linker,_i.e._ TMSPEDA/GA, because of multilayer generation. In this case, the C peak is increased form 15.1 to 21.7 (at.%), in comparison to the survey spectra of the sample treated only with TMSPEDA. The last result is derived from the BE 284.4 eV, which is characteristic for C-C bond. An increase of this peak area is a sign for an aliphatic carbon contamination that originates either from insufficient cleaning or contamination in the short time span between the processing steps and the analysis with XPS.

For the other linker a decrease in the content of N is detected in comparison to the samples withholding only the silane layer. However, it is not obvious from Fig. 3.3, if the DITC has coupled to the terminal amines of the anchor and in what stoichiometry. Therefore, the S is determined in the samples with DITC in a second run of measurements including C as a reference (Fig. 3.4). The assumption that one DITC molecule binds to a single terminal amine is also considered here, as the rigid structure of the molecule prevents bridge formation between two amines on the surface (79). It is observed for all three surface modifications that the amount of S2p is lower than the theoretically expected amount. The largest is the difference between the measured S2p from the TMSPEDA/DITC
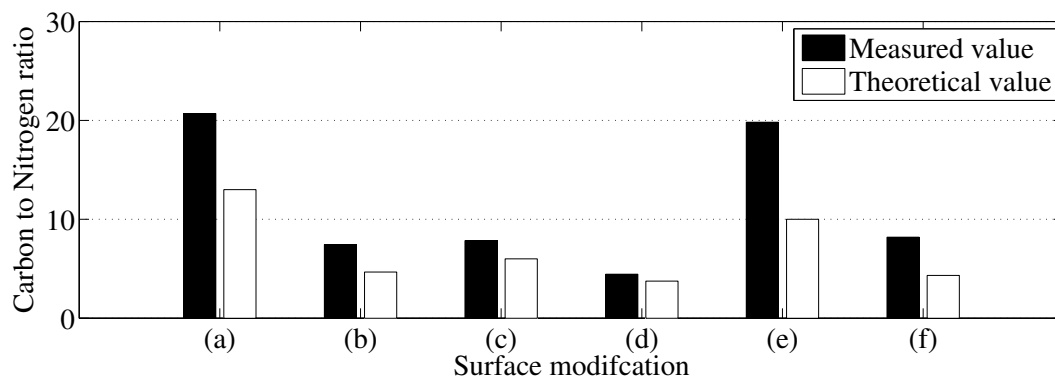
Figure 3.3: The ratios of C to N determined in the XPS survey measurements and the calculated ratios based on the model-layer structure after at *Stage II*: (**a**) APTES/GA; (**b**) APTES/DITC; (**c**) TMSPEDA/GA); (**d**) TMSPEDA/DITC; (**e**) EDSPA/GA; (**f**) EDSPA/DITC.

sample and the theoretical ratio (7:1), it is established that for each DITC molecule there are two molecules of silane.
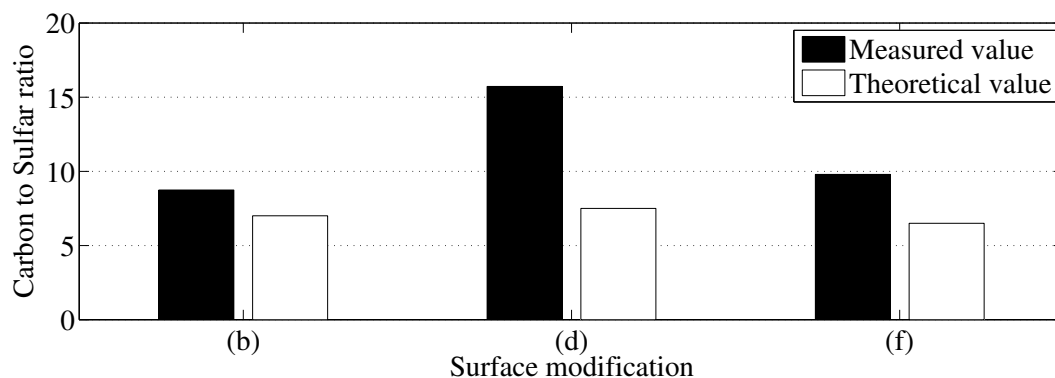
Figure 3.4: Samples containing DITC as a linker with their C to S ratio determined by XPS measurements. Plotted together are the theoretical structure based content and the measured values from: (**b**) APTES/DITC; (**d**) TMSPEDA/DITC; (**f**) EDSPA/DITC.

The APTES surface has a marginal difference between the measured and the predicted ratios, thus it is most likely that the assumed correlation is correct, i.e. one anchor binds to one linker molecule. The ratio for the EDSPA showed approximately 30% lower content of sulfur than predicted by the model, which is in agreement with the findings from *Stage I*. This means that barely 70% of the studied area are coated with the DITC at this *Stage II*. As coverage is the least in comparison to the other measurements, out of the six modifications on the Si surface the EDSPA/DITC is least likely to be implemented further for the enzyme immobilization.

3.2.3 Terminal stage - dendrimeric molecule and chelated metal ions

In the present section the stoichiometry in the final two stages of surface modification is evaluated, i.e. NTA binding and Ni^{+2} chelating before the immobilization of the protein, by comparison of the theoretically expected versus the XPS measured content of N and Ni. The surfaces are designed to terminate with the coupled NTA, a chelating agent, which has a dendrimeric structure that forms a complex with one Ni atom via four coordinate bonds. Therefore, the completion of this final step is crucial as each NTA would bind two of the His residues from the tag of the enzyme. It is important to evaluate the number of NTA molecules available in order to choose the one with maximum binding sites. To achieve this the ratios of C:N for the six modifications are studied.

The expected and measured ratios are calculated in the already described manner (see Appendix A for details) and the results are shown in Fig. 3.5. The overall trend is that N is less than the theoretically predicted value in 5 out of the 6 cases. The explanation of the gap between the predicted and the measured value could be twofold. First, the monolayer assumption for the theoretical model is not strictly valid. Second, the coverage of the surface is not complete, and the number of plausible reactive sites for immobilization is less, which is in agreement with the results from *Stage II*.
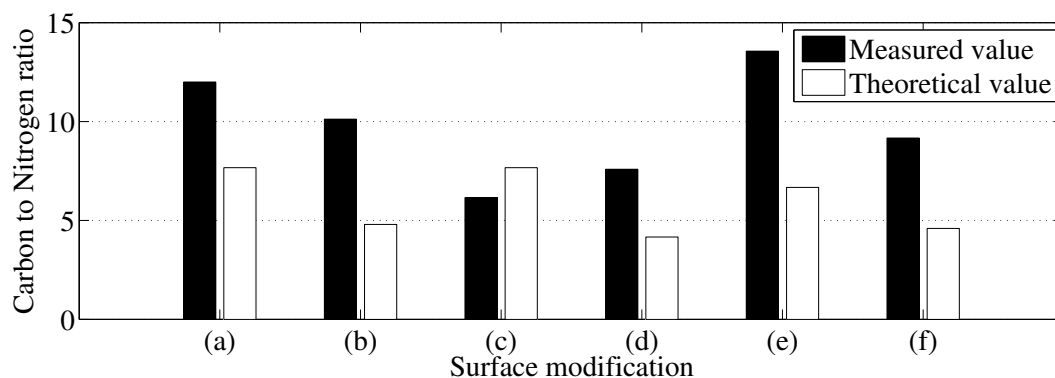
Figure 3.5: Predicted *vs* measured ratios of C to N after *Stage III*. Surfaces after NTA binding with the corresponding C to N ratios determined by XPS measurements and the theoretical content of: (**a**)APTES/GA/NTA; (**b**)APTES/DITC/NTA; (**c**)TMSPEDA/GA/NTA; (**d**)TMSPEDA/DITC/NTA; (**e**)EDSPA/GA/NTA; (**f**)EDSPA/DITC/NTA.

Similar results are recorded for the DITC containing samples (Fig. 3.3). The only exception is observed for the TMSPEDA/GA/NTA modified surface. It demonstrates abundance of N exceeding the theoretically expected amount, therefore it is favored for further immobilization as it is the closest to the predicted values. It must be noted that during the GA coupling there has been deviation from the suggested model based on single molecule binding. In the last stage more NTA molecules have attached to the GA treated surface, probably due to the high number of aldehyde reactive sites which are a result of the thick build-up discussed earlier. The result indicates compensation for the poor coating on an earlier stage by the GA.

For some of the samples a decrease is observed in the ratios for C to N after coupling of the NTA (Fig. 3.5) in comparison to the counterpart ratios measured after coupling of the linker to the anchoring silanes (Fig. 3.3). For instance, the C:N ratio for the APTES/GA is approximately 21:1, in contrast to 12:1 in the case of APTES/GA/NTA. These findings suggest that the NTA had attached to the surface. This could be due to the fact that the GA has detached from the surface during the washing process or reacting with NTA. Few of the surfaces did not have a decrease or had a marginal change leading to a low population of the NTA.

In order to determine the number of active sites, one more ratio (C:Ni) is calculated from the measured data, and displayed in parallel with its theoretical counterpart in Fig. 3.6. Notably for all the studied modifications, the content of Ni on the surfaces related to the XPS determined carbon is extremely low. In fact, the measured amounts of Ni are approaching the detection limit of the XPS (0.2 - 0.5 for C1s) for three out of the six surfaces. Hence, the results in Fig. 3.6 ((b),(d),(e)) are presented for comparison to emphasize the divergence between the hypothetical model and the actual value but at the same time are arbitrary because they are close to the detection limit. Even though Ni is not detected on every sample, it can be seen that the theoretical ratio for the surface containing APTES/GA/NTA/Ni has value of 23:1 (C:Ni) while the measured value is 68:1, meaning that the real number of Ni atoms constitutes approximately 33 % of the expected number. For the same anchoring molecule but different linker, the APTES/DITC/NTA/Ni, an even more dramatic difference is observed: theoretical 24:1 versus experimental 261:1 , thus providing only 9.2% of the expected amount of Ni^{2+}.
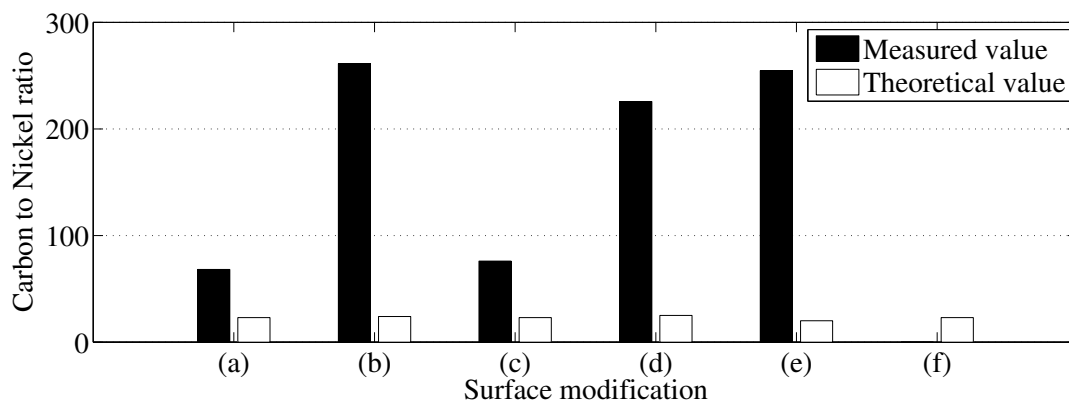
Figure 3.6: **Predicted *vs* measured ratios of C to Ni after *Stage IV*** The measured ratios by XPS, together with the theoretical content, e.g. one atom per build-up at the final, *Stage IV*: (**a**) APTES/GA/NTA/Ni^{2+}; (**b**) APTES/DITC/NTA/Ni^{2+}; (**c**) TMSPEDA/GA/NTA/Ni^{2+}); (**d**) TMSPEDA/DITC/NTA/Ni^{2+}; (**e**) EDSPA/GA/NTA/Ni^{2+}; (**f**) EDSPA/DITC/NTA/Ni^{2+}.

The tendency of those ratios is that the GA linker leads to low C:Ni ratio, that could be the result from a thick multilayer. In contrast, the DITC linker would form, in the best case scenario, a single layer that provides significantly less targets for the NTA to bind. From the three aminosilanes

the most attractive, in terms of C:Ni, seems the TMSPEDA which also shows strong discrepancy from the suggested model, but altogether is more Ni saturated than the EDSPA and at about the same level of saturation as the APTES. The general observation from the elemental analysis is that nearly all surface modifications do not reach the hypothetical-model stoichiometry from Figure 3.1.

Despite the lower amounts of chelated Ni there are proofs of the chelation on all the surfaces except for one, the EDSPA/DITC/NTA. The worse of the six surfaces is the EDSPA/DITC/NTA/Ni on which no Ni is detected; also the C:N ratio is roughly four times lower than the hypothetical. Nevertheless, the fit of the main Ni^{2+} peak, in the other samples, gives a binding energy of around 856 eV, a value found in $Ni(OAc)_2$ and $Ni(OAc)_2 \cdot 4H_2O$. Therefore, several of the surfaces would be further studied for protein immobilization by using a model protein (His_6-EGFP). To pin-point the results from the Si pieces, more detailed chemical analysis of their high resolution spectra is carried out further.

3.2.4 General analysis of the high resolution elemental spectra

In this section analysis of the layer formation based on high resolution elemental spectra from the XPS is presented for each of the surfaces (see Appendix A, Fig. A.1–A.12) at every stage of their modification depicted in Figure 3.1. The layer formation is studied from both the changes in area ratios and the position of a characteristic peak, whether it is shifted or not. Furthermore, by comparing the spectra, for instance, of the C1s (C=O:C-N) to N1s (NHC=O:(-NH_2/NH_3^+)) it can be established whether there is a C contamination on the surface. These assessments are facilitated because of the known chemical bonds that form during the process of surface modification, however, the formation of bonds can be established *de novo* without any knowledge of the surface treatment.

Surface modified with APTES/GA/NTA/Ni^{2+} Comparing the relative peak areas of spectra recorded after *Stage I* for APTES (Fig. 3.1, a) treated surface show for the N content that the ratio of NH_2:N=C after *Stage I* equals 2.5. Consecutively, the addition of GA (*Stage II*) decreases the ratio to 0.8. This means that the GA binds with the formation of a double bond to the nitrogen of the terminal amine as the number of N=C has been increased and the relative amount of the -NH_2/NH_3^+ is unaltered but with a shift towards lower energies. Additional shift is seen at this *Stage II* towards lower BE of NHC=O peak, normally BE 400.3 eV. The slight shift (to BE 400.27 eV) is a hint for hydrophilic interaction between the aldehyde and terminal amine. In other words, part of the amine groups stepped in reaction while the protonated amines, originating from the APTES, are likely to form a hydrogen bond with the aldehyde groups. The nature of the H bond is characterized by weak, reversible interactions, that can lead to dissociation and imperfection of the layer.

At *Stage III*, NTA is added on the surface. As expected the NH_2 component of the spectra is increased whilst the N=C is decreased. This observation is deduced, firstly, from the ratio NH_2:N=C that emerged to value of 5.4 and secondly, from the ratio NH_2:(-NH_2/NH_3^+) drop, 4.5 in *StageII* to

3.4 in *Stage III*. The author's speculation is that an increase of the number of protonated amines (NH_3^+) can be due to reverse orientation of the NTA molecule, facing the surface with its three acetate groups.

In the last *Stage IV* the ratio of areas of $NHC=O:NH_2$ showed value of 1.97 with a visible decrease in area (by 15 %) for the $NHC=O$ while the $-NH_2/NH_3^+$ increased by 13.5 %. This is related to the Ni chelation, as the formation of coordinate bonds would decrease the $NHC=O$, that originate from the NTA, in a reversed proportion to $-NH_2/NH_3^+$. All things considered, the layer formation of a modified surface (Fig. 3.1, a) is proved after analysis of the element spectra of C1s and N1s.

Characterization of APTES/DITC/NTA/Ni^{2+} modified surface.

Considering the alternative linker DITC in *Stage II* (Figure 3.1, b) of the modification, there is less pronounced change of area ratios, in comparison to the GA linker. The area ratio $NH_2:N=C$ has a value of 2.5 for APTES (*Stage I*) versus 2.0 after the linker addition (*Stage II*). In contrast to the GA, the DITC do not form multilayers. Moreover, the later linker carries two thiocyanate functional groups that contribute to the area of $N=C$ peak. Although it is difficult to conclude with certainty that the layer has a complete coverage on the surface, this result suggests that there is a successive coupling of the DITC to the APTES.

The addition of NTA (*Stage III*) leads to less $N=C$ and a boost of $(-NH_2/NH_3^+)$ peak; which is seen in the change from 2.59 to 3.97 for $NH_2:(NH_2/NH_3^+)$ and indicates the addition of NTA to the DITC. This happens because a bond is forming between the primary amine of the NTA and the thiocyanate group of the DITC, which leads to higher content of N and concomitant decrease of the $N=C$.

At the fourth stage, an overall shift in the BE is observed by approximately 1 eV towards higher energies which is a hint of the complex formation with Ni^{2+}. However, such tendency is not consistent with the result from the previous modification. Redundant is the strong presence of the $NHC=O$ peak, characterized by the ratio of 2.73 that is determined from the areas of $NH_2:NHC=O$. The final prove for the layer build-up is the presence of Ni^{2+} but the reason for the poor coverage is not completely understood. Despite the non-complete coverage the surface contains chelated Ni^{2+} ions, that makes it suitable for enzyme immobilization studies.

Surface modified with TMSPEDA/GA/NTA/Ni^{2+} Next in the scope comes the surface treated with the TMSPEDA, the initial ratio of $NHC=O:NH_2$ is 1.6 which after the reaction with the GA is doubled up to 3.3 demonstrating the formation of bonds between the amine and aldehyde. It is hard to attest whether the attachment of GA follows Michael addition or a Schiff base formation, as there is no significant change in the peak area of $N=C$ between *Stages I* and *II*. The slight shift from 399 eV in *Stage I* to 398.7 eV in *Stage II* can be attributed also to amine formation (BE 398.9 eV) according to literature (60). However, Michael addition is not likely to occur in this case

because it only takes place when conjugated alkenes are present. In order to check if it is peak form contamination a correlation is sought between the peak area of C=O (BE 288,1 eV) in the C1s (see Appendix A, Fig. A.5) and the peak area of NHC=O (BE 400 eV) in the N1s spectrum. More specifically, the ratio is calculated between the areas for NHC=O:(NH_2 plus $-NH_2/NH_3$), cf. N1s spectrum (see Appendix A, Fig. A.6), and the C=O:C-N in the C1s spectrum. The two ratios are significantly different with values 2.5:1 against 0.5:1 for the C1s. Such discrepancy suggests that 20% of the NHC=O correlate to the C1s and N1s spectra. Therefore, it can be concluded that the other 80% of NHC=O found in the N1s spectra are due to contamination with adventitious Carbon (61).

Typical rise in the peak area of $-NH_2/NH_3^+$ is registered in *Stage III*, which is ascribed to the addition of NTA on the surface. Another high peak is observed at 398.7 eV, that can be characteristic for amines. It is likely, however, that the last peak can be due to a double bond formation between the primary amine of the NTA and the aldehyde group from a GA.

The evidence for the NTA binding is found at the final stage, an increase is observed for the NHC=O peak with a slight shift towards higher energy, a hint for the Ni^{2+} chelation to the three carboxyl groups and the tertiary amine of NTA. The presence of Ni 2p3 shows that Ni^{2+} is chelated with the NTA (66). Moreover, the fit of the main peak (Ni 2p3) gives a binding energy of around 856 eV which is a value typical for $Ni(OAc)_2 \cdot 4H_2O$. Despite the adventitious C, this proves that the surface modification is complete from the anchoring layer up to the chelated Ni^{2+} ion for the TMSPEDA/GA/NTA/Ni^{2+} surface modification.

Characterization of the TMSPEDA/GA/NTA/Ni^{2+} formation The surface modified with the same silane but DITC instead of GA linker (Figure 3.1 , d), is analyzed next. In *Stage I*, after deconvolution the NH_2 peak has area of 35.4%. Based on the ratio of NH_2:($-NH_2/NH_3^+$), namely 4.5:1, it can be concluded that about 22% of the amines after silanization are protonated. Depending on the molecular orientation of the organosilane, the protonated amines are considered to have bonds formed to the surface, other silane moieties or both as has been determined for aliphatic amines by Graf *et al* (78).

However, the remaining non-protonated groups are available for bonding as they do not interact with the surface. As a result of the DITC addition, the ratio NH_2:($-NH_2/NH_3^+$) is slightly reduced in *Stage II* while the peak area of NH_2 remains unchanged.

During *Stage III* of the surface modification, this trend is preserved; the ratio of 3.4:1 is reached for the NH_2:($-NH_2/NH_3^+$), which is accompanied by increase of NH_2:N=C, i.e. from 1.6 (*Stage I*) to 4.2 (*Stage III*) because of both decrease of N=C and increase of NH_2 peak areas. The spectra results prove build-up of the layer with the attachment of NTA through a single bond. The last result is in contrast to the GA linker which formed more N=C bonds.

After addition of Ni^{2+} the peaks of $-NH_2/NH_3^+$ shift in the direction of higher energies (BE 399.9 eV)for the last two peaks, this event can be interpreted as electron redistribution after the

Ni^{2+} chelation. In his recent work, T. Yoshida (62) suggests that oxime have very similar BE 399.8 eV; however, in our case oxime formation at the last *Stage IV* of the surface treatment is unlikely and can only be ascribed to adventitious Carbon. Therefore, no cross-check for oximes is performed as the peak with BE of 399.9 eV is ascribed to NH$_2$ after a shift, according to literature (63) NH$_2$ without shift is found at BE 399.6 eV.

Characterization of the EDSPA/GA/NTA/Ni^{2+} formation The following ratios are derived from the spectra of the surface silanized with the EDSPA (Figure 3.1 , e, *Stage I*) from the peak areas of NHC=O:(-NH$_2$/NH$_3^+$ plus N=C) in N1s 0.9:1 which is approximate to the value calculated from C1s 0,4:1 for the ratio of C=O:C-N. Taking in consideration these two ratios, it can be calculated (0.9/0.4) that approximately half of the detected C=O originates from NHC=O and the other half is an adventitious Carbon contribution. Such spectra occurs typically after the addition of GA. In the current case the main cause is considered to be alteration of the functional amino groups of the organosilane, as suggested in a study by Graf and coworkers (78) focusing on surface treatment by utilization of organosilanes and their stability in time. Looking closer at the C1s and N1s (Appendix A, Fig. A.9, A.10) we see that the main peaks after deconvolution are at 284.8 eV and 400.3 eV typical for aliphatic C and imide (BE 400.7 eV) respectively (60). It can be concluded that the imide peak in author's opinion is actually shifted NH$_3$ peak (BE 399.6 BE) (63), which is due to interactions of the amines with the surface. These results stand as a prove; first, that there has been, the inevitable under N$_2$ conditions, contamination with C in the form of NHC=O; and second, that the amino group is altered. These factors can hamper further build-up of the layers.

After the addition of GA, the ratio of NH$_2$:(-NH$_2$/NH$_3^+$) rises to 6.9:1, in parallel, the relative area of NHC=O is diminished from 47.2% in *Stage I* to 32.2% in *Stage II*. The cross-check for C1s and N1s for the ratios of C=O:C-N and NHC=O:(-NH$_2$/NH$_3^+$ plus N=C) are matching at 0.5:1, thus proving that the NHC=O in *Stage II* are not a result of contamination but due to interactions between GA and EDSPA. All three peaks in the high resolution spectra for N1s are shifted towards higher energies, in that case the BE of 399.4 eV could actually be ascribed to the formation of various nitrogen carbon bonds, for instance N=C or N=C=C.

Surprisingly, there is no shift of spectra in *Stage III* with the addition of the NTA to the GA functionalized surface. Moreover, the area of the -NH$_2$/NH$_3^+$ with BE 401.49 eV has increased, whilst the peak characteristic for the C=N is reduced. This is a hint for the detachment of the GA from the surface during NTA addition. However, the ratio of the NH$_2$:(-NH$_2$/NH$_3^+$) seems to be fixed at 0.55:1, which is due to an increase of the area for NH$_2$. Thereupon, sufficient amount of GA is left for the NTA to interact and bind to the surface. It is likely that weak interactions occur between charged NTA and GA species, the non-specific of those are disrupted in the consecutive washing steps.

26

An increase is seen in the last *Stage IV* for both NH_2 (399 eV) and -NH_2/NH_3^+ (401.75 eV) peaks resulting in ratio 1.91:1 proving the decrease in the number of GA species on the surface. Important is also the shift observed towards higher energies indicating that Ni^{2+} is chelated successfully. According to the Ni 2p3 peak, the Ni^{2+} is chelated in trace amounts, which is also in agreement with the analysis of the elemental spectra.

Surface characterization of the EDSPA/DITC/NTA/Ni^{2+} The *Stage I* of the EDSPA treated surface has been already discussed in the previous paragraph. In the *Stage II*, however, a drop is observed to 12.5% for the relative area of the amine at 398 eV in comparison to the initial value of 34.7%. Nevertheless, the ratios of the NH_2:NH_2/NH_3^+ coincide at about 2.6 for the two stages. One explanation for the observed N decrease is that EDSPA detaches because it is not covalently bonded to the surface, leading us back to the argument of organosilane orientation on the surface. Nonetheless, the DITC interacts with the amine of those EDSPA molecules that are bonded, and contributes two secondary amines that balance somewhat the ratio NH_2:NH_2/NH_3^+. The major consequence, however, is less binding sites for potential attachment of the NTA at the next *Stage III*.

In *Stage III* no significant shifts are observed, and also the peak area for NH_2 (BE 399.8 eV) is not altered after the NTA has been added to the build-up. The ratios between N=C:(-NH_2/NH_3^+) are nearly unaltered 0.8 versus 0.5 from the previous *Stage II*. Minor change is recorded in the relative area of C=N. In contrast to the DITC/NTA treated surfaces, however, this change is not significant. These results are an evidence of a hindered NTA addition that will lead to a low amount of Ni^{2+} binding sites.

The surface is barely altered in *Stage IV* when judging from the minor shift of the peaks towards higher energies, which is a sign of electron density redistribution. The characteristic NHC=O formation, detected at the last stage for the other samples, is absent. In addition no Ni^{2+} is detected from the Ni 2p3 peak. On the whole, the poor binding of EDSPA at initial stage and the fact that DITC linker does not form multilayers the amount of binding sites is below the detection limit of the XPS.

3.2.5   Assessment of the dienyl acetate interactions with non-modified Si via *in situ* FTIR

Adsorption on non-treated Si is studied with FTIR in order to elucidate the interaction between the Si and (*Z,E*)-9,11-C14:OAc. The frequency of the symmetric stretch C-C-O at 1237 cm^{-1}, measured from the flow-cell on a dry surface, is decreased upon adsorption due to greater electron density and destabilization of the carbonyl bond (81). The spectra are shown in Fig 3.7 (a, b, c) for comparison. According to previous studies, vibrational frequency shifts of the adsorbed versus solution-phase dienyl acetate are due to interactions between hydrogen-bonding donor sites on the surface and π electrons in the carbonyl groups of the dienyl acetate molecules. Evidence for the adsorption is the

slight shift (7 cm^{-1}) of the C=O stretch found usually at 1750 cm^{-1} towards lower wavenumbers, result of lowering the bond order and decreasing the frequency of the C=O stretching vibration (70).

Another key point is the residue of water, after 26 h of purging with N$_2$ in order to measure from a dry surface there is the scissors bending at 1652 cm^{-1}, that is +10 cm^{-1} from its typical position, and a large peak is observed at 3464 cm^{-1} originating from OH stretching (3400 cm^{-1}). The water fingerprint is completed by the broad combination band at 2120 cm^{-1}. However, the surface is dry because the 1743 cm^{-1} and 2929 cm^{-1} are detectable; otherwise, a spectrum similar to the one in Fig 3.7 (e) is going to be observed. This means that the detected water interacts with the adsorbate, dienyl acetate, without displacing it from the surface.
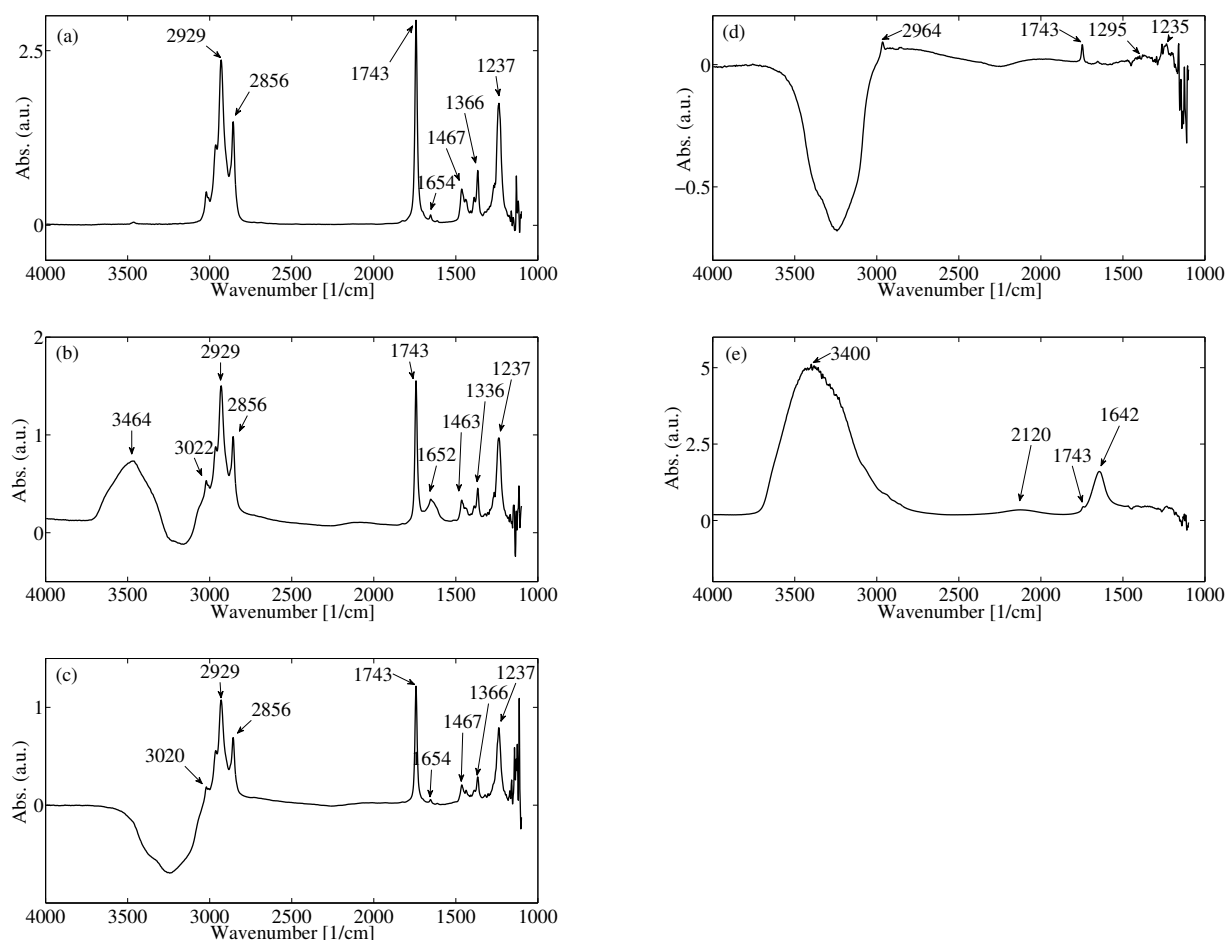
Figure 3.7: FTIR spectra collected during *in situ* measurements using a micromachined flow-cell: (**a**) spectrum of the pure dienyl acetate ((*Z,E*)-9,11-C14:OAc);(**b**) after rinsing with copious amounts of water; (**c**) rinsing with the buffer solution (10mM Tris-Cl, 4%DMSO, 10%Glycerol); (**d**) flushed with ethyl acetate; (**e**) measurement with the buffer solution inside the flow cell. Spectra (**a**) to (**d**) are collected from dry surfaces.

By the same token, a shift of the band frequency with coverage is observed, which would be characteristic of a changing interaction with the surface. The relative amounts of two stationary bands appear to vary with surface coverage, which is a clear signature of multisite adsorption to a

heterogeneous surface. Example of such a shift is observed for the flow cell filled with buffer-solution (e). Due to the abundance of water molecules a shift is detected from 1654 cm^{-1} to 1642 cm^{-1} for the scissor bending peak, and a negative shift by 64 cm^{-1} to the nominal 3400 cm^{-1} of OH stretching. At the same time the dominant peak at 1743 cm^{-1} (C=O) has reduced its intensity. Thus even the excess addition of a less polar adsorbent than the dienyl acetate does not rupture its bonding to the surface but rather interacts with the existing layer.

The Glycerol and DMSO in the working solution marginally decrease the bands of the C=O and the symmetric stretch C-C-O; however, the 3464 cm^{-1} is gone and the negative band is deepened at 3250 cm^{-1}. Thus, together with the water being removed off the surface after perturbation from the DMSO and/or Glycerol, also some amount of the dienyl acetate is detached. None of the reagents used in the experiment displaced completely the dienyl acetate from the Si surface. Therefore more polar solvent, ethyl acetate, is injected through the flow-cell.

The resulting spectrum, Fig 3.7 (d), demonstrates reduction of intensities for the characteristic dienyl acetate peaks (1237 cm^{-1}, 1743 cm^{-1}), and a shift from 2929 cm^{-1} to 2964 cm^{-1}. More importantly, the water peak of the OH stretch at 3246 cm^{-1} has the approximate intensity (-0.69 a.u.), which means that the dienyl acetate is displaced without any further water removal from the surface. Additionally, there is no band at 3700 cm^{-1} denoting an interaction between OH from the silicon surface with adsorbate. This is important because it gives a hint of the type of interaction between the acetate and the surface. On the basis of the spectra for the silicon surface and the changes in bands upon contact with the more polar solvent, ethyl acetate, the sites that are available as candidates for adsorption of polar molecules are solvent-perturbed free silanols and hydrogen-bonded surface water. The last is in agreement with the work of Rivera *et al.* who proved that the solvent-perturbed silanols are strongly involved in the adsorption of ethyl acetate from n-heptane (70).

Given these points, the adsorption of the dienyl acetate is realized through hydrogen-bonded surface water on the Si surface. Once adsorbed, the molecules of the dienyl acetate are partially displaced from the surface after water rinse or treatment with the working buffer-solution. However, the dienyl acetate is removed only when more polar solvent is introduced to the system, which is a prove of reversible interaction between the adsorbate and the Si surface.

3.3   Conclusions

The current chapter explored six surface modifications by elemental and chemical XPS analysis to determine those of them with the best coverage. For the purpose, at each modification stage the layer formation is evaluated through comparison of the XPS results to a hypothetical model, as criteria are considered the number of potential binding sites and the homogeneity of the layer. Finally, it is determined that both TMSPEDA and APTES in combination with GA or DITC linkers provided sufficient coverage but not as much binding sites, chelated Ni^{2+}, as expected from the theoretical model.

In a consecutive set of FTIR experiments it is proved that the dienyl acetate is retained from aqueous solution on non-coated Si surface. The interactions with the surface are proved reversible but required more polar solvent than the dienyl acetate in order to be displaced. These findings proved the need for homogeneous coating of the tubing and not only the microreactor, that would both mask the adsorption sites of Si and would provide stable immobilization.

4

Immobilization of His$_6$ protein on silicon-glass microreactor walls

Based on the results from the XPS analysis several surface modifications are favored for the immobilization of two model proteins. The knowhow of the surface modifications (see Chapter 3) was implemented inside a silicon-glass microreactor. Although, the CmAAT1 has many unidentified characteristics, some details as the molecular weight, amino acid sequence, and that the enzyme has a His$_6$ tag bioengineered for purification purposes are known. Therefore, it is feasible to use a straight forward method for surface modification and consecutive enzyme immobilization of the recombinant protein CmAAT1. The number of intermediate modification steps makes it slower in comparison to silica-encapsulation (71). Nonetheless, the silanization approach is providing opportunities to create the base for covalent bonding and stable build-up. The binding of the silane is a process consisting of hydrolysis of one or more alkoxy groups, followed by condensation and covalent bond formation after temperature treatment (72).

The role of the spacer is to increase interaction of the enzyme with the carrier, as the importance of the coupling distance has been proven by Taylor for the trypsin (73). Two well known linkers with different chemical properties are considered in the current study: 1,4-phenylene diisothiocyante (DITC) (74) and the pentane-1,5-dial or glutaraldehyde (GA) (75).

In the final stage of the surface modification, it is chosen to implement N_α,N_α-*bis*(carboxymethyl)-L-lysine (NTA) as the chelating molecule as it has been proven suitable not only in protein purification but also in immobilized-enzyme microreactors mimicking metabolic pathways (76). Theoretically, the completed modifications have the function of immobilization, with the additional important feature that the adsorption of enzyme on the surface is such that changes in the conformation of the enzyme and loss of activity are prevented.

Another important issue that we address in the current chapter is adsorption of substrate and product inside the microreactor. Although we have already studied the adsorption of dienyl acetate on non-treated Si surface *in situ*, adsorption inside the microreactors could differ due to modifications

of the surface. Therefore, surface characterization of the layers inside the microreactor is required. Lastly, the study expands towards the protein-support interactions.

Two of the silanization protocols are implemented in microreactors, then the layers are visualized. Protein binding was studied and activity assay of the immobilized CmAAT1 performed. The protein adsorption is studied inside the microreactor using EGFP for qualitative analysis of these modified surfaces, then preliminary activity tests are performed with immobilized enzyme on the walls of the microreactor. At the final the adsorption of (Z,E)-9,11-tetradecadienyl acetate on the modified microreactor surfaces is addressed.

4.1 Materials and Methods

4.1.1 Activation

After microfabrication, the surface of the silicon-glass microreactor is covered with the naturally occurring SiO_2. As stated in the previous chapter, the oxide layer consists of siloxane bonds which are stable and relatively inert, not likely to step in to reaction readily. In order to activate the surface, Piranha solution, a mix of H_2SO_4 and H_2O_2 (3:1), is flushed continuously through the channel for 25 minutes. The Piranha is a strong oxidizing agent and reacts vigorously with organic components! The hydroxyl radicals from the solution brake the siloxane bonds to form silanol groups. To drive the excess acid and peroxide out, the channel is rinsed with copious amount of water flushed through for 25 minutes. It is important to have a dry surface for the silanization step, therefore, the channel is thoroughly dried by N_2 flow followed by EtOH flush and finally one hour at 150°C.

4.1.2 Silane anchoring

For the silanization process it was chosen to work from anhydrous toluene solution instead of using gaseous deposition. The predetermined concentrations are tested: 1.5% for the APTES or 4% for the TMSPEDA. The solutions are incubated at room temperature inside the microreactor for 4 hours. Then a nitrogen flow was used to drive the liquid out of the channels, anh. EtOH was pumped through to flush the non-reacted organosilanes, and the microreactors are further dried in N_2 flow. To cross-link the TMSPEDA and also APTES molecules, the samples are heated at 150°C overnight.

4.1.3 Introducing a glutaraldehyde spacer

The dry channels are filled with 5% GA in 0.5 M $NaHCO_3$ (pH8.5) for two hours at room temperature. Afterwards the surfaces are N_2 dried.

4.1.4 Coupling diisothiocianyte spacer

Another possible spacer variation, DITC, is introduced as 0.1% (w/v) solution in anh. toluene. The silanized surfaces are kept for 4 h at 60°C. Finally, the surfaces are rinsed with anh. EtOH.

4.1.5 Carrier binding and charging with Ni^{2+}

The carrier molecule NTA has a terminal, primary amine that binds to the aldehyde groups originating from GA as well as to the diisothiocyanate of the DITC. This process is conducted from a solution of 0.5% NTA in MilliQ, pH8, adjusted with NaHCO$_3$. The surfaces are incubated for 2 h at room temperature; then rinsed with EtOH, and exposed to N$_2$ flow till dry.

Next, 400 mM NiSO$_4$ at pH6.5 is incubated for 20 minutes at room temperature. The excess solution is flushed out with 10 mM Tris-Cl (pH7.3) buffer. The enzyme CmAAT1 is immobilized straight after the Ni^{2+} charging.

4.1.6 EGFP immobilization in the microreactor and fluorescent microscopy

Based on the results from the XPS analysis several surface modifications are favored for the immobilization of two model proteins. A non-coated microreactor was filled with a 10mM fluorescent protein in buffer solution and a fluorescent image was acquired using microscope with external light source(Leica AF6000 with EL6000, Leica microsystems, Germany). The solution was pumped out, and after rinsing with water another image was produced, thus providing information about the retention of EGFP on the non-treated surface. The same solution of 10 mM His$_6$-EGFP was newly prepared in Tris-Cl, pH 7.5, and then introduced into the functionalized microreactor, where it is incubated for 20 min in dark to avoid bleaching. For rinsing 10 mM Tris-Cl buffer is used to get the excess protein out of the system, and an image is taken to observe the fluorescence of immobilized protein.

For the desorption assay the microchannel is washed with 250μM Imidazole in water at pH 8 adjusted with NaOH. This is a non denaturing elution buffer popular also in the commercially available Ni-NTA protein purification columns. Fraction is collected for protein concentration analysis. Another image of the microreactor is taken to detect the non-specifically bonded protein.

4.1.7 Enzyme immobilization

A total amount of 8.5 μg CmAAT1, which is the target enzyme, is immobilized on the chosen surfaces following the procedure: 50 μl of buffer-protein solution 10mM Tris-Cl pH7.3, containing 10% Glycerol, is pulse pumped in to the microreactor at flow rate 5 μl/min. Then the protein is left for incubation in the microreactor for 40 minutes at 4°C; this step is repeated 5 times. After total incubation time of 2 h the pass-through fraction, a wash buffer with weakly bonded protein from the microreactor and the pass-through fraction of imidazole are collected separately. Those fractions are used for an SDS page, and a protein quantification.

4.1.8 Activity and adsorption assays in the microreactor

In the activity assay a reaction buffer is prepared containing: 10 mM Tris-Cl (pH 7.3) with 10% Glycerol containing 250 μM Acetyl-CoA, 320 μM (Z,E)-9,11-C14:OH and 4% DMSO. The DMSO

is added to prepare the initial solution of (*Z,E*)-9,11-C14:OH as the last has low solubility in water. The reaction buffer is run through the system at 10 μL/min using the syringe pump. Fractions from the biomicroreactor are collected in sealed glass vials. A batch reaction experiment is set in parallel under the exact same conditions: reaction buffer, reaction volume, enzyme concentration, and temperature. Batch reactions are not quenched.

From each sample the organic phase is extracted with hexane as follows. Internal standard, dodecyl acetate, is added to the hexane up to a concentration of 0.3 μg/mL. Then, 0.2 ml of this mixture with the sample are vortexed for 1 minute. The sample is frozen on dry ice and organic fraction is extracted with glass Pasteur pipette into a clean vial. The step is repeated once. Next, the samples are partially evaporated under a N_2 flow, and analyzed in GC-MS.

The GC parameters are optimized to achieve separation of substrate and product for the utilized column (HP-5ms GC, Agilent). Injector and detector (FID) temperature are set to 280°C. The oven temperature is initially set at 80°C and a temperature program is set with a heating rate of 3°C/min and a plateau at 280°C for 10 minutes. In order to achieve higher signal, the measurements are done in splitless mode at 60 mL/min and a splitless time of 0.6 minutes. Helium is used as a carrier gas at a flow rate of 1.3 mL/min.

4.1.9 SDS page and protein determination in the flow through fractions from the microreactor

Well established method, by Smith (77), is used for preparing sodium dodecyl sulfate (SDS) 5% polyacrylamide gel electrophoresis with Coomassie Blue staining.

4.2 Results and Discussion

4.2.1 Investigation of the functionalized surfaces inside a microreactor

The enhanced green fluorescent protein S65T, tagged with His_6, is immobilized on the surface to visualize and estimate the specificity of the binding. Also the surface of the microreactor is studied with HR-SEM.

Visualization of the TMSPEDA leads to several interesting findings: the layer is partially detached from the surface to form folded floating structures inside the microchannel. Although it is hard to estimate the exact thickness of the layer during this experiment, the fluorescent image of the coating is a proof that the coating is a multilayer structure (Fig. 4.1, (a)). One possible cause for the detachment can be the condensation of the organosilane molecules in the process of surface modification. From literature is known that the thickness of the layer is dependent on the initial concentration of silanes and also on their orientation towards the surface. In contrast, using the same protocol on flat Si pieces did not result in multilayer formation of such magnitude.
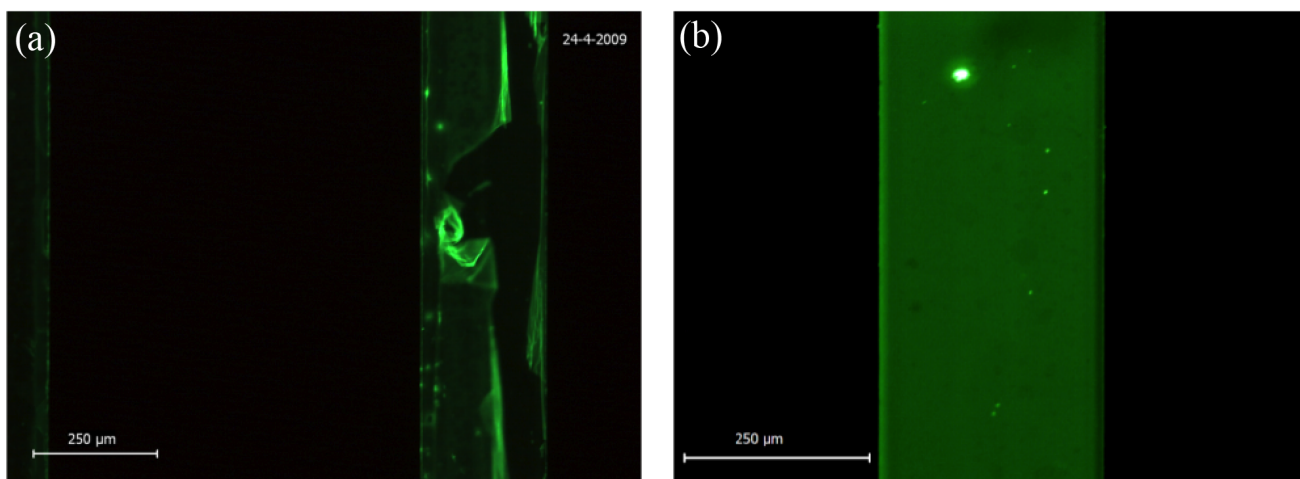
Figure 4.1: Layer imperfections inside the microreactor. Detached TMSPEDA/DITC/NTA/Ni^{2+} layer (a) and for comparison attached APTES/DITC/NTA/Ni^{2+} (b).

There are two possible interpretations of this result: the condensation is taking place in the solution or on the surface, as it is already covered with TMSPEDA molecules that have not bonded covalently. The first situation would lead to agglomeration of organosilanes that would probably be driven out of the microchannel during the washing step. In the second case different orientations can exist: the silane group facing the surface; the amino group gets in contact with the surface; both groups are in contact while the molecule is bent. If one of the groups is in contact with the surface at some moment in time, then the other group, silane or amine, would be exposed to react. The silanol groups of molecules from the solution can interact with the NH$_2$ of the attached monolayer (78). Likewise, a penta-coordinated Si could form according to the work of Chauhan and coworkers as a result of the interaction between the silane and NH$_2$ (80). This type of multilayer structures will be under stress during cross-linking in lateral direction. This result explains the rupture of the multilayer and detachment from the surface, Fig. 4.1 (a). Presumably, the stability of attachment of the layer could be enhanced if the concentration of the anchoring organosilane is reduced, as condensation would not occur.

The APTES (Fig. 4.1, b) is not detaching from the surface, and the layer is rather homogeneous judging from the attached S65T. The question is, what has prevented the detachment. A possible explanation is, that lower concentration during the anchoring step leads to homogeneous layer formation. The higher the concentration the higher will be the probability of polysilane formation. Even though the XPS, resulting from the Si pieces, did not prove cross-linking on the surface the layer of APTES seems stably attached to the surface. Based on the fluorescent micrograph only, it is impossible to estimate the thickness of the layer. Therefore, the microreactor cross-section is studied with HR-SEM.

The HR-SEM images unveil agglomeration inside the microreactor, specifically at the corners of the rectangular channel, Fig.4.2. Intriguingly, the build-up starts in the edges and seems to protrude towards the middle of the wall, and in the middle of the channel a layer of several nanometers is deposited.
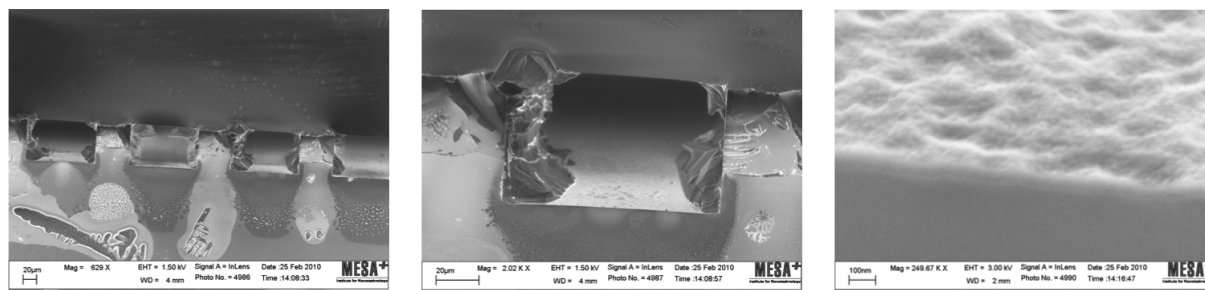
Figure 4.2: **Multilayer build-up inside the microchannel.** High resolution scanning electron micrographs showing the microreactor having rectangular cross-section channels with an APTES/DITC/NTA modified surface. Starting from the left the image is zoomed.

The theoretical thickness of the APTES/DITC/NTA should be about 3 nm, considering the number of bonds and the length of a C-C bond 1.57 A. Exceeding this value would mean that there is multilayer formation. Specifically in the corners and on the side walls a build-up is observed. The DITC and NTA are not prone to multilayer formation thereupon the whole contribution to those thick layers should be due to APTES. However, on the planar Si pieces equal N:C content (12.6 at%) is expected (12.0 at%) is detected. As N is related directly to the amount of APTES on the surface, this shows that on the planar surface a monolayer is generated. Inside the microreactor the same surface modification protocol is implemented and resulted in aggregation. Despite the stability towards hydrolysis, the APTES can polymerize with the formation of polysilanes. The author's hypothesis is that hydrolysis starts from the corners of the channel as there might be residual water trapped after the drying step. Due to the fast temperature change, from 150°C to room temperature, water from air can condense inside the microchannel and thereafter trigger hydrolysis and condensation of the APTES into lumps.

Nevertheless, there might be a positive effect of the detachment (TMSPEDA) and the aggregation of the anchoring molecules (APTES), as the overgrown layers could provide higher number of binding sites, respectively larger amount of immobilized enzyme that would eventually result in more efficient conversion inside the microreactor. Therefore, the TMSPEDA and APTES variants of the surface modifications are further studied for their capacity to retain proteins/enzymes.

In a separate set of experiments the APTES/DITC is explored in terms of specific binding via NTA/Ni^{2+} to the model protein, His_6-EGFP. The last should readily bind to the chelated Ni on the surface resulting in a fluorescence, as is demonstrated in Fig. 4.3 (a). Then after introducing imidazole, which competes for the Ni^{2+} binding sites, in the microchannel the EGFP should be

detached from the surface and driven out of the microreactor by the flow. Although the fluorescence is diminished, there is detectable signal from the surface (Fig. 4.3 (b)). This is an evidence of additional, non-specific, interactions between the molecule of the EGFP and the modified surface. An interaction between the modified surface and the S65T leads to uniform fluorescent signal, in contrast the fluorescence scatters across the surface, as can be seen from the control experiment (Fig. 4.3 (c)) where a non-treated surface is exposed to the EGFP at conditions similar to those for the modified surface. More importantly, in the non-modified channel a reversible interaction is observed, which is proven with disappearance of the signal after thorough rinsing, Fig. 4.3 (d).
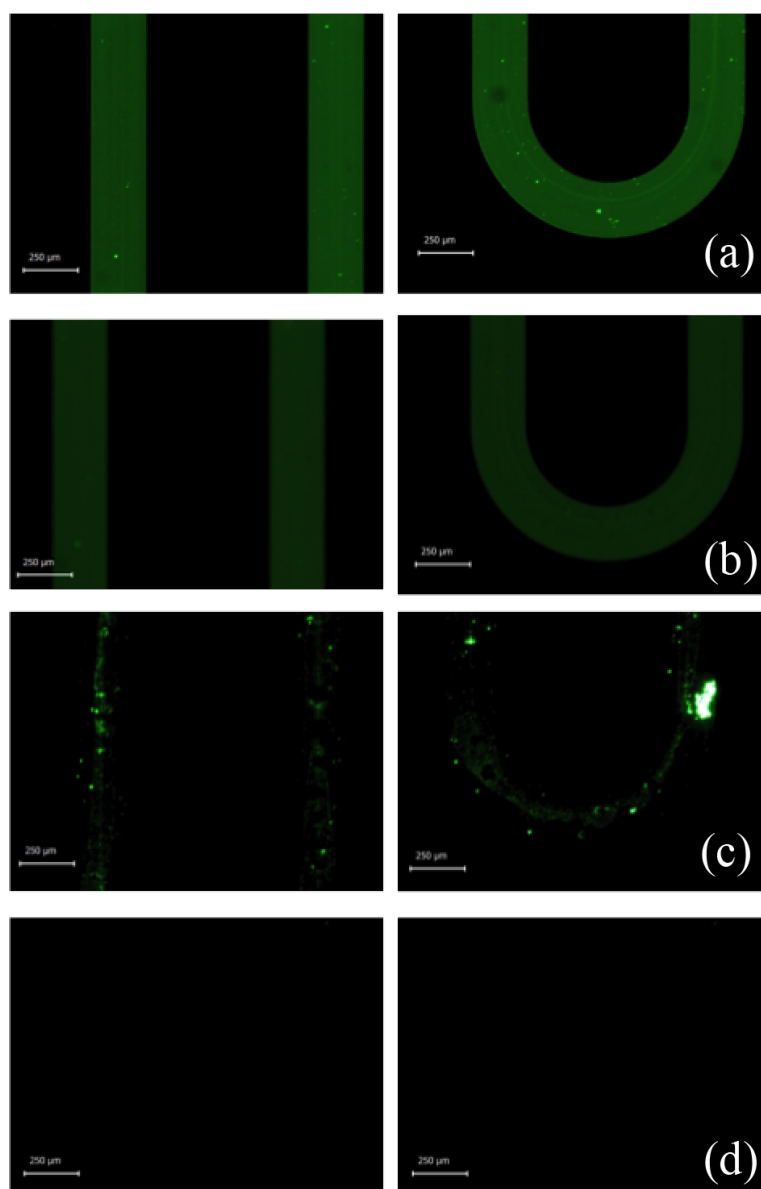
Figure 4.3: Fluorescent micrographs representing the non-specific binding of His$_6$-EGFP to APTES/DITC/NTA/Ni^{2+}. Observed signal from the microreactor after EGFP attachment (a); imidazole treatment (b); non-modified surface (c); non-modified surface thoroughly rinsed (d).

To understand better the nature of the adsorption inside the microchannel the experiment is extended towards detachment of the protein by acting on it with a nonionic detergent. These results are shown in Fig. 4.4. As can be seen from the results of the experiments, the fluorescent signal is reduced significantly after treating on the surface with imidazole. Specifically on the sidewalls and also in the middle of the channels there is residual fluorescence. The sidewalls are covered with a cluster of APTES as is observed in the HR-SEM study of the microchannel surface. The aggregation has started from the APTES and mainly consists of it but with the consecutive layer depositions (GA or DITC and NTA), the build-up is an agglomerate of all functional groups originating from the rest of the layer components. Thus, the rich environment of functional groups induces the unspecific binding observed in Fig. 4.4 (b). The issue of protein adsorption on solid surfaces has been tackled in numerous publications and studies. Some of the typical interactions are due to charge-charge, Van der Waals forces or hydrogen bond formation. The covalent bonding, for instance between thiocyanate group from the DITC and an NH_2 is also possible. To explore whether the binding is reversible or not, a nonionic detergent is pumped through the microreactor. The fluorescent signal is diminished even further, to the level that no lumps are recognized inside the channel. This indicates an important finding, namely that the nonspecific binding of the fluorescent protein, S65T, is due to weak interactions.
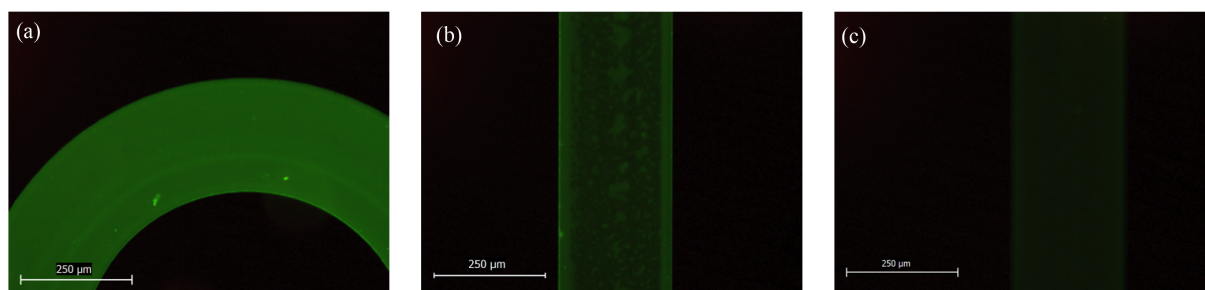
Figure 4.4: Reversibility of binding. Florescent microscopy images representing the bonded His_6-EGFP after rinsing with 10mM Tris-Cl (a), imidazole (b) and tween (c).

If the nature of interaction is covalent bonding, it would most likely lead to a number of drawbacks, like enzyme deactivation. Moreover, no reutilization of the microreactors will be possible after the activity of the biocatalyst is completely lost because the protein will attach irreversibly to the surface. The main goal here of course is not to immobilize the fluorescent EGFP (a.k.a. S65T) but to have a functional microreactor with immobilized CmAAT1. Next, the issues related to the immobilized enzyme and its activity in the microreactor are discussed.

4.2.2 Immobilization of the CmAAT1 inside the microreactor

The protein immobilization is confirmed via gel electrophoresis of the CmAAT1 fractions (Fig. 4.5) after passing the enzyme through microreactors modified with TMSPEDA and DITC or GA. Despite the detachment from the microreactor walls, these two surface variations are chosen for further

exploration because the flat surfaces have coatings, according to the XPS analysis from the Si pieces. Moreover, it is critical to determine whether the multilayer is advantageous for CmAAT1 immobilization. The SDS page is run with the fractions collected straight after immobilization (F0); F1 is originating from the loosely bonded enzyme detached from the walls after a buffer rinse, and the final strip fraction (F2) containing the specifically bonded His_6-CmAAT1, is collected after imidazole treatment.

Comparing the F0 lanes from the two microreactors, and considering the identical protein concentrations and immobilization conditions, it is visible that more protein is immobilized in the system with the GA linker as the signal (F0) from that microreactor is less intense than the F0 from the system with DITC.

Nearly no enzyme is detected in any of the two lanes (F1) corresponding to the wash fraction, which means there had been no detachment from the wall of the microsystem.

Alarmingly, the final (F2) are almost completely empty, which denotes a non-specific immobilization of the enzyme as imidazole is expected to compete with the His_6-CmAAT1 for the binding sites on the surface. That would result in exchange of the specifically bonded biocatalyst to the smaller imidazole molecule.

Thus for the TMSPEDA modified surface it is proven that there is immobilization of the enzyme on the modified surface, more on the surface with the GA linker in comparison to the DITC. Moreover, it is established that the enzyme is retained on the surface due to non-specific interactions different from the NTA-Ni-His_2. Otherwise it can detach after the imidazole treatment.

Similar results are obtained also from the APTES modified surface. The enzyme attaches to the surface according to the decrease in the intensity of the fraction passing through the microreactor. However, in the consecutive washing steps it is not recovered.
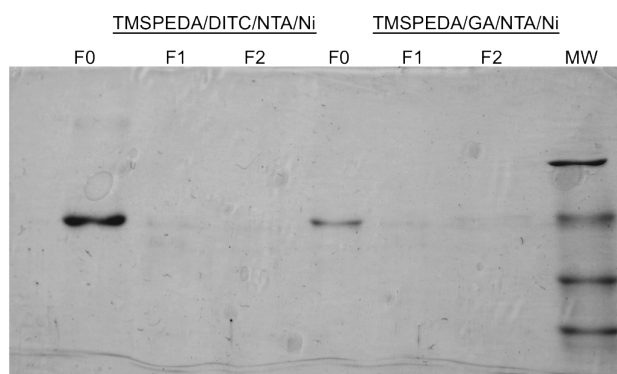
Figure 4.5: Protein retention inside the microsystem. Comparison of the protein fractions recovered from two microreactors: (F0) represents the fraction after immobilization; (F1) after rinsing with Tris-Cl; (F2) imidazole (250 mM) strip

Despite the non-specific binding of the enzyme it is an intriguing question whether catalytic activity is preserved after immobilization or the interactions with the surface lead to deactivation.

In order to answer this question, an activity assay is performed in a microreactor, which surface is functionalised with APTES and DITC or GA, plus chelator (NTA) and Ni^{2+}. The (*Z,E*)-9,11-C14:OH is determined from the peak area with retention time 26.3 min after passing the reactive mix through the biomicroreactor, at flow rate 2 μl/min. An internal standard (I.S.) peak area has retention time inside the column 24.2 min; typical for the product is retention time 29 min, Fig. 4.6. The MS peak for the acetate has m/z of 60.5–61.6, whilst the aliphatic chain with 14 C atoms and two unsaturated bonds has characteristic 191.5–192.5 m/z. The enzyme is proven active in batch reaction as is seen from Fig. 4.6, (a) the conversion of the dien-ol (26.3 min) in dien-acetate (29.0 min). No activity is detected after the CmAAT1 immobilization in the microreactor with APTES/DITC surface modification, Fig. 4.6, (b). That finding can be ascribed to a number of factors, among which the nonspecific interaction between the surface and the biocatalyst coupled with a possible partitioning.
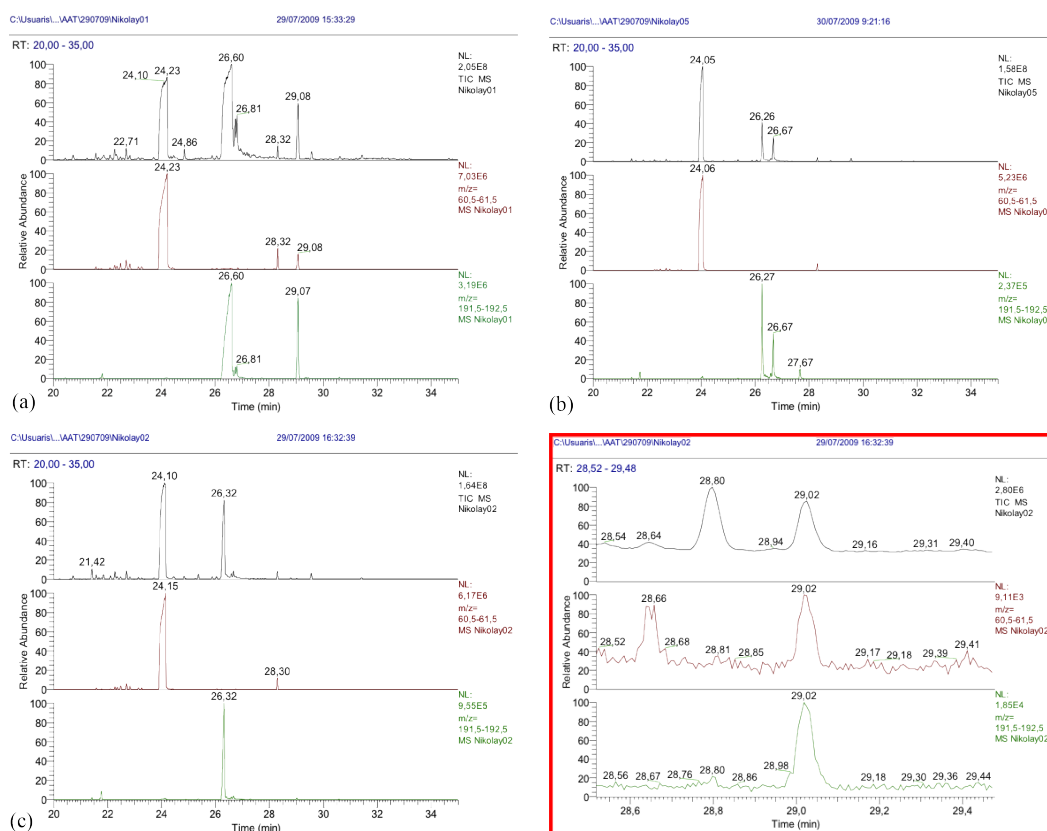
Figure 4.6: Activity assay of the immobilized CmAAT1. Batch activity of the CmAAT1 in a glass vial (a), negative results from an activity assay in APTES/DITC/NTA coated microreactor (b), also in an APTES/GA/NTA (c) and traces of the product, magnified in the last GC-MS pane (red frame).

The later is evidenced by the peak area for the substrate, (*Z,E*)-9,11-C14:OH, that is noticeably reduced in comparison to its counterpart (Fig. 4.6, (a)), even though concentration deviates from the initial (320 μM) because of conversion. Similarly large decrease is detected also for the substrate content after passing through the microreactor with APTES/GA treated surface (Fig. 4.6, (c)).

Despite the choice of linker molecule, GA or DITC, the substrate and/or product are retained inside the system. The last statement, concerning the product, is based on the fact that both substrate and product have very similar chemical structures; therefore if the substrate interacts also the product would. To support this hypothesis comes the data from the same activity experiment, where trace amount of the product is detected. That leads to enzyme partitioning inside the microsystem, in which the interaction of the substrate and product with the surface of the microreactor influence the conversion inside the system. The main consequence is reduced yield of product due to substrate retainment leading to reaction hinderance. By this same token it is not clear which of the two factors is dominating as both of them are result of non-desired surface interactions.

A strategy is proposed for the blocking the potential active sites with bovine serum albumin (BSA), which is a protein, that is supposed to interfere with the nonspecific enzyme adsorption on the surface. However, this blocking strategy did not lead to increase in the activity of the microreactor. Another dynamic type of strategy is tested in an attempt to solve the retention of substrate and lessen the partitioning. A saturated decanol solution in water is pumped through the channel just before the activity assay. However, the decanol is not competing for the same binding sites as the adsorption of dien-alcohol is not reduced afterwards. At this stage a conclusion can not be drawn that the hydroxyl group from the alcohol is a secondary factor influencing adsorption, as the layer imperfections and detachment can contribute to the partitioning.

4.3 Conclusions

Investigation of the microreactor surface showed multilayer formation, most probably due to condensation of the silanes. Even though detachment is registered for the TMSPEDA treated surface, in which case silanization took place from more concentrated solution, partitioning is also evidenced inside the APTES coated microreactor without detachment. In addition, from the non-specific binding of the two model proteins can be concluded that the surface modification strategies considered in the current chapter are proven inapplicable for their immobilization. Therefore, an alternative path has to be sought for realization of the biocatalytic process of interest.

5

PEMs for a functional microreactor†

Insects communicate with their con-specifics using complex blends of volatile chemicals called pheromones. The pheromone communication system consists on the release of specific chemical blends, generally by females, to the environment that are then detected by a very sensitive olfactory system of males. These chemical blends are biosynthesized in a pheromone gland in most cases from fatty acids by pheromone specific enzymes. The biosynthetic pathways of the sex pheromone of the moth *S. littoralis*(82) was taken as a starting point for the development of a chemical communication system to mimic the generation and reception of a chemical signal(83). One of the biosynthetic modules, is an enzymatic microreactor system to perform the final biosynthetic step in the production of the major component of the pheromone, (*Z,E*)-9,11-tetradecadienyl acetate(82). In the future, such modules will be hierarchically integrated to establish a chemoemitter for infochemical communication.
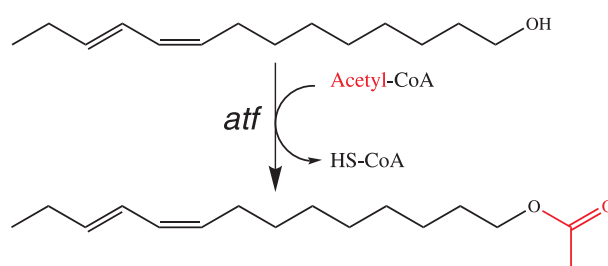
Figure 5.1: Bioconversion catalyzed by an alcohol acetyl transferase (a wax ester synthase, *atf*, in this paper). In the presence of acetyl-CoA *atf* transforms the (*Z,E*)-9,11-tetradecadienol, the pheromone precursor, into (*Z,E*)-9,11-tetradecadienyl acetate, the pheromone product.

The last step in the biosynthesis of all components of the pheromone blend of *S. littoralis* consists of the transfer of an acetyl group from acetyl-CoA to the precursor alcohol. This reaction is catalyzed in the moth by an alcohol acetyl transferase. However, due to the absence of a known acetyl transferase in *S.littoralis*, we selected an orthologue (a wax ester synthase, *atf*) to perform the

same biochemical reaction (Fig. 5.1). The *atf* esterifies aliphatic alcohols with carbon chains longer than 6 into the corresponding acetates(155). To exploit this enzymatic reaction in a microreactor module, a route was sought to immobilize the enzyme in a microreactor compartment. Several of such compartments, containing different biosynthetic enzymes, may then be connected by an integrated microfluidic network (see e.g. (85)) in order to mimic the complete biosynthetic pathway. Several methods to immobilize enzymes in a microfluidic environment have been described in the literature(86; 87; 88; 89), and for simplicity we followed a similar procedure to that reported by Soeng et al(124). This involved immobilization of the enzyme on microbeads and package of the beads into a microfluidic chip, through which a flow of the substrate solution was passed to produce the expected product at the outlet.

Preliminary experiments with such a construct showed that the compounds of our interest were prone to adsorb on the surface of the silicon/glass microreactor. Previous fundamental studies have proved that adsorption on silicon surfaces (with a native oxide) occurs on silanol groups(91; 92). Building a polyelectrolyte multilayer (PEM) on these negatively charged groups, may mask the charges and prevent adsorption. Deposition of PEM was implemented using a layer-by-layer (lbl) technique, suggested by Iller(93) and later developed by Decher(94). The polyelectrolyte system explored here was PEI/DSS. A similar approach was adopted by Kim *et al.* as a basis for thromboresistant thin films on polyvinyl chloride(95). The polyelectrolyte modification of the silicon surface is a versatile method in terms of layer optimization which allows fine tailoring of interfacial properties. During the last two decades research has been performed on PE stability(96), growth regimes(97; 98) and interaction with proteins(99; 100). Additionally, specific knowledge on PEI charge density(101), (102), adsorption behavior(103), (104) and dynamics of protein interactions at interfaces(105) provide us solid ground for further exploration and implementation of the PEI/DSS couple in a biomicroreactor.

Foregoing literature describes the adsorption of PEI on silica (103), (104), (97) and the PEI coupling to epoxysilane for attachment of antibodies(106), however the PEI/DSS polyelectrolyte couple has not been studied in details for deposition on silanized silicon surfaces. Thus, it is important to characterize the layer formation and thickness on the silanized substrate under various conditions, and to compare with their non silanized counterparts before application in a microreactor.

5.1 Materials and Methods

Branched polyethyleneimine (PEI) 50% (wt) solution with molecular weight 750 kDa and PEI with molecular weight 1.2 kDa as polycations, and dextransulfate sodium salt (DSS) from *Leuconostoc spp.* as polyanion with molecular weight 500 kDa were used in the lbl deposition. The cross linking reagent, crotonaldehyde , sodium cyanoborohydride ($NaCNBH_3$), sodium chloride (NaCl), acetate, MES monohydrate and borate buffers, dodecyl acetate (97%), toluene (anh. GC grade), *N,N*-dimethyl-formamide (DMF), dimethyl sulfoxide (DMSO, GC grade), glycerol, acetyl Coenzyme A

sodium salt (acetyl-CoA), Trizma HCl (Tris-Cl), hydrogen peroxide (H_2O_2, 30%), (3-glicidoxy-propyl)-trimethoxysilane (97%, GC grade) and sulfuric acid (H_2SO_4, 98%) were purchased from Sigma-Aldrich (Chemie BV, Germany), and used without further modification. The (Z,E)-9,11-tetradecadienyl acetate was purchased from Bedoukian (Danbury, USA).

The agarose beads were part of His Band purification kit from Novagen (Darmstad, Germany). One side polished 4 inch Si(1 0 0) wafers were obtained from Okmetic (Vantaa, Finland), 4 inch borofloat glass wafers were purchased from Schott AG (Benelux, Netherlands).

5.1.1 Surface activation before layer deposition

Characterization of lbl deposition was conducted on 7x7 mm square pieces diced from the silicon wafer (Disco DAD-321, Tokyo, Japan). Prior to layer deposition the silicon pieces were activated with piranha solution (H_2SO_4 (98%):H_2O_2 (30%) 3:1) for 25 min. (Piranha is a strong oxidizing agent!) The abundance of hydroxyl radicals from piranha opens the siloxane bonds on the Si/SiO_2 surface to form silanols. Surfaces were washed for 25 min with copious amounts of Milli-Q water (Millipore, Billerica, US), dried in N_2 flow and on a hotplate in air at $100°C$ for 5 min.

5.1.2 Polyelectrolyte layer-by-layer deposition

Non-anchored layer In our study, direct deposition of non-anchored PEM on the activated wafer surfaces was performed by lbl adsorption(94), an electrostatically driven sequential deposition of polyelectrolytes from water solutions. Initial experimental conditions for the PEM generation were chosen according to Kim(95). Two variants of PEI, with molecular weight 1.2 kDa and 750 kDa, were used as polycations during the lbl deposition. For each molecular weight 0.01% (wt) PEI aq. solutions were prepared in 10 mM MES buffer at pH 6 and 10 mM borate buffer at pH 9.2. Crotonaldehyde (4.1 μM) was added and the salt concentration was adjusted to 1.7 mM NaCl. Time of incubation in the PEI solution was 10 min at room temperature. The loosely bound PEI molecules were removed with sufficient amounts of Milli-Q water.

The Si pieces were transferred consecutively into Eppendorf tubes containing 0.4% (wt) DSS in 10 mM acetate buffer, pH 3.8, with 1.7 mM NaCl and incubated for 10 min at room temperature. Non-adsorbed DSS molecules were discarded by washing with Milli-Q.

An odd number of layers were deposited alternating PEI with DSS, thus terminating the build-up with positively charged PEI.

Anchored layer Anchored PEM, via (3-glicidoxypropyl)trimethoxy silane, was obtained following a slightly modified protocol from the originally reported covalent attachment on silicon beads(107). Activated, dry, Si pieces were incubated in 1.5% (3-glicidoxypropyl)trimethoxy silane solution in anh toluene for 2 h and then rinsed with DMF. Coupling of the amino group to the epoxy was done overnight using 0.01%(wt) PEI (molecular weight 1.2 kDa or 750 kDa) in DMF. The pH values were maintained with 10 mM MES, pH 6, or 10 mM borate buffer, pH 9.2. The Si pieces were rinsed

with Milli-Q water. The processing continued for an odd number of layers as the direct deposition lbl described above, terminating with PEI as target molecule because of its positively charged amino groups.

Reduction of the Schiff bases To complete the process and to obtain stable cross linking, a 10 mM solution of $NaCNBH_3$ in 10mM acetate buffer, pH 3.8, was applied to the surface for 1 h at room temperature. During this step the Schiff bases were reduced. Surfaces were rinsed with water and dried overnight at 30°C before characterization.

5.1.3 Characterization of the polyelectrolyte layers on Si surface

Surface morphologies and step heights were studied with a commercial atomic force microscope (Dimension Icon, Bruker, Germany) equiped with a Nanoscope V controller. All scans were obtained in non-contact mode using rectangular silicon cantilevers (NCH, NanoWorld, Switzerland) with a force constant of 42 N/m. The roughness of the surfaces was determined for a constant scan area of 1 x 1 μm on dry samples. The raw data were processed and visualized with Gwyddion (version 2.19), an open source software.

The scans for the step measurements were conducted after scratching away part of the coating with a scalpel. Then heights were obtained from those scans by fitting a step-height (Gwyddion) to the interface between scratch and coating. For each surface modification the mean height value and standard deviation was calculated from three cross sections, as illustrated in Fig. 5.2.

The thickness of dry polymer layers was determined by ellipsometry on the Si pieces after each layer of the PEM deposition process. Angles Ψ and Δ were measured with a VASE (J.A. Woollam Co., Inc, Lincoln, USA) ellipsometer at three incident angles, 65°, 70°, 75°, using the wavelength (λ) from 250 to 1250 nm. The number of samples was duplicated in order to evaluate the reproducibility of lbl deposition. Thickness and refractive index of the native oxide layer on bare Si pieces were obtained by using the WVASE32 modeling software for the measured Ψ and Δ in the beginning of each experimental series. The mean layer thickness was calculated from the three incident angles data, fitted by the two layer Cauchy mathematical model.

The stability of the coatings was evaluated by comparison of thicknesses before and after incubation in working conditions. The initial layer thicknesses were ellipsometrically measured, two points from each sample, then the samples were left in 10 mM Tris-Cl(pH 7.3) with 10% glycerol at 30°C for a week. Samples were dried and the measurements were repeated.

5.1.4 Fabrication of the silicon/glass microreactor

Fabrication of the silicon-glass microreactor followed well established techniques schematically represented in Fig. 5.3. The silicon wafer was cleaned 5 minutes in 99% fuming HNO_3, 5 minutes in another beaker with 99% fuming HNO_3, then rinsed with water, followed by 10 minutes at 95°C in 69% HNO_3, and finally rinsed in Milli-Q water till a conductivity 0.1 μS was obtained. Next the
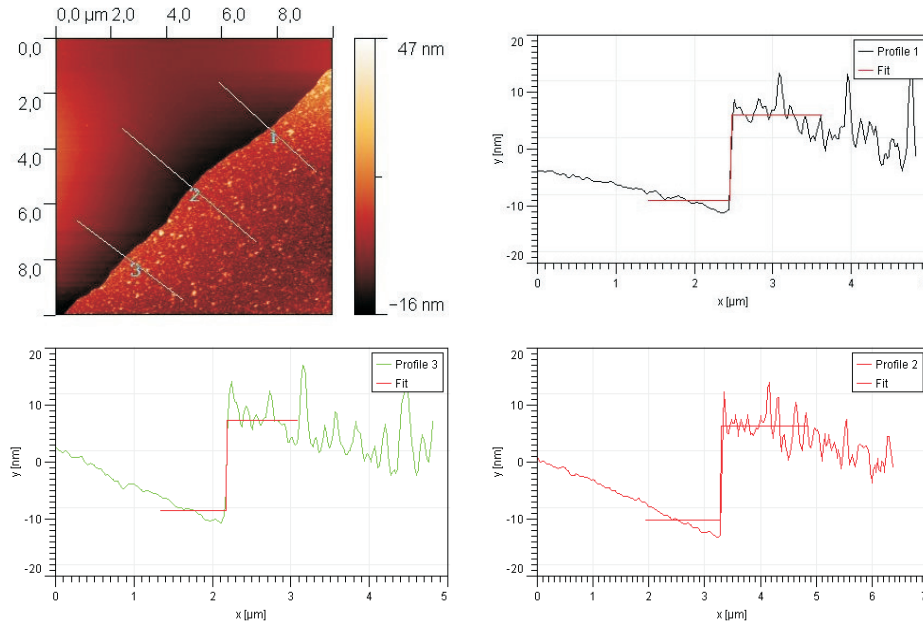
Figure 5.2: Height of step measurement. Three cross sections were set in random positions on the AFM scan across the scratch/coating interface and a model was fit measuring the step heights.

wafer was spun dry (Delta 10), covered with HDMS and spin coated at 3000 rpm with photoresist (OiR 906-17, Fujifilm, Japan) thickness 1.7 μm.

The resist was soft baked at 95°C for 1 minute and the channels were defined by photo lithography using a mask aligner (EVG 620, EV Group, Austria) with near UV source (365 nm) at approximately 12 mW/cm^2 and 3.1 seconds exposure time. After that, the resist was developed for 50 seconds in OPD 4262, the wafer was rinsed in Milli-Q water and spun dry. A "Bosch" Directed Reactive Ion Etching (DRIE) (B-UNIFORM recipe, Adixen AMS100SE, Alcatel, France) was applied for 10 minutes to create a 200 μm deep channel with straight walls into the silicon wafer. Acetone was used to strip the residual photoresist. On the polished side of the wafer the micro-channels were protected from possible damage by transportation foil. Next, photosensitive foil was applied on the backside of the wafer and through-holes were defined with photolithography. Prior to powderblasting, the irradiated structures were developed in 18.8 mM $NaHCO_3$, in two cycles of 2 minutes. After powderblasting, the foil was removed in acetone and the wafer was stripped from the fluorides, formed during Bosch processing, first with oxygen plasma for 10 minutes (500 W) followed by 15 min at 800°C. The resulting SiO_2 was etched for 2 min in 50% HF, Fig. 5.3 (e). A Borofloat wafer was cleaned, spin dried and pre-bonded to the clean, dry Si wafer and anodically bonded (EV 501 Bonding Station, EV Group, Austria). Lastly, the microreactors were separated by dicing.

47
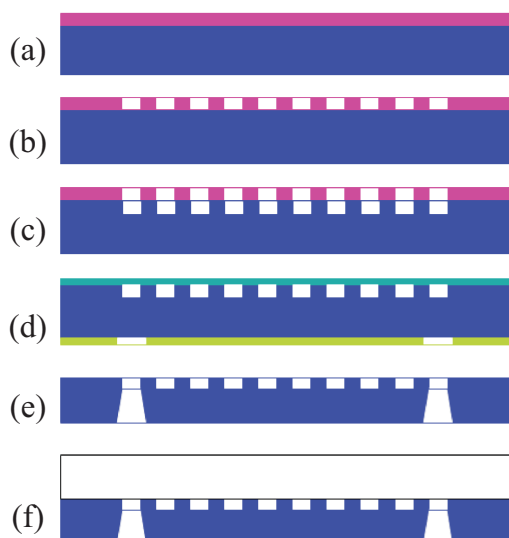
Figure 5.3: Process flow of microreactor fabrication: (a) after HDMS, photoresist was spun on the wafer; (b) channel was defined by litography; (c) reactive ion etching of the channel; (d) the wafer was cleaned in acetone and dried, the channel was temporarily sealed with transportation foil to avoid possible damage, backside of the wafer was covered with photosensitive foil and through-holes were defined by litography; (e) through-holes were powderblasted and Si wafer was cleaned; (f) the channel was sealed by anodic bonding to borofloat glass.

5.1.5 Adsorption of (*Z,E*)-9,11-tetradecadienol and (*Z,E*)-9,11-tetra- decadienyl acetate inside the silicon/glass microreactor

Reaction buffer with predefined concentrations of substrate and product was flown through the microreactor at a rate of 10 μl/min. The non-coated microreactor with non-coated syringe and capillary was compared with the microsystem (microreactor and capillaries) coated with high molecular weight (HMW) PEI/DSS (pH 9.2/3.8) in the adsorption experiment. Collected fractions at the outlet were extracted with hexane and analyzed by GC-MS (ThermoFisher Sci., Madrid, Spain).

5.1.6 Determination of His$_6$-EGFP adsorption inside a silicon/glass microreactor

Standard dilutions were prepared from a stock solution of 40 μM His$_6$-EGFP in 10 mM Tris-Cl containing 10% glycerol. Fifty μL of the stock solution were transferred into an Eppendorf tube with 50 μL of 10mM Tris-Cl, 10% glycerol to result in 20 μM concentration. By repeating this process, standard solutions of 10, 5, 2.5, 1.25 and 0.625 μM were obtained. A non-coated microreactor was filled with the last standard dilution a fluorescent image was acquired at magnification x20 with 4 s. exposure time using a microscope with external light source (Leica AF6000 with EL6000, Leica

microsystems, Germany), and the microreactor was flushed with water. The process was repeated with the next dilution sample (1.25 μM) and so on until all dilution samples were tested. The obtained fluorescent images were converted (Matlab 2008a, The MathWorks, United States) to 8-bit gray scale images and the average of the pixel intensity was calculated for each image. The collected data points were plotted versus the protein concentration to generate the calibration curve shown in Fig. 5.4.
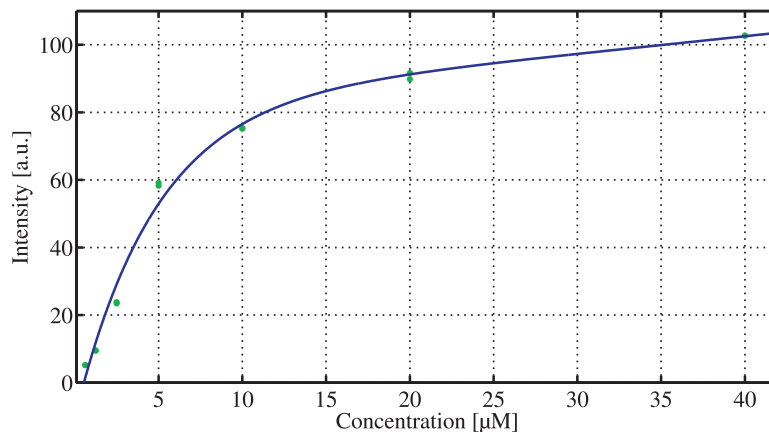
Figure 5.4: Calibration curve imaging the His$_6$-EGFP content versus the fluorescence intensity measured inside a microreactor. Fluorescent images were acquired in duplicate and concentrations were plotted against their intensity values, the data were fitted to an exponential curve.

For the adsorption measurement 20 μM His$_6$-EGFP solution was inserted in an anchored HMW PEI/DSS (pH 9.2/3.8) coated microreactor and incubated for 30 minutes at room temperature. An image of the microreactor was acquired to evaluate the fluorescence of the protein. The biomicroreactor was shortly rinsed with buffer and another image was acquired. The measurements were triplicated. The amount of adsorbed His$_6$-EGFP was determined by using the calculated intensity from these images and the already generated calibration curve.

5.1.7 Expression and purification of His$_6$-*atf*

The construction pET23a::His$_6$atf was kindly provided to us by Prof. Alexander Steinbüchel (Westfälische Wilhelms Universität, Münster, Germany) and transformed into *Escherichia coli* cells (strain Rosetta (DE3)pLys). The protein was expressed according to the procedure described by Steinbüchel et al(155). Next the overexpressed *atf* was purified from the crude extract by metal affinity chromatography (Novagen), followed by membrane dialysis (MWCO 68000, 6.4 mm diameter, Spectrumlabs) to remove the Imidazole used during the chromatographic elution.

5.1.8   Immobilization and activity assay of the His$_6$-*atf* inside the microreactor

In total a five layer structure was anchored via (3-glycidoxypropyl)trimethoxy silane inside a microreactor and capillaries, following the protocol described above and using HMW PEI/DSS (pH 9.2/3.8) for 10 min deposition time in a stopped flow mode. Then 100, μL of solution containing NTA functionalised agarose beads were introduced into the microreactor. The beads were prevented from leakage by adjusting the gap between the capillary and microreactor outlet smaller than the smallest measured bead diameter, approximately 30 μm. Further, conditioning of the packed agarose beads was performed in accordance with the Novagen protocol for protein purification.

A solution of 10 μg His$_6$-*atf* in 10mM Tris-Cl, pH 7.3, with 10% glycerol was prepared. The solution was manually injected into the microreactor and incubated for 30 min. The collected fraction was re-injected, and incubation was repeated untill the total incubation time was 2 h. The enzyme was kept on ice during incubation. The biomicroreactor was thoroughly washed with buffer using a syringe pump (PHD 2000 Programmable, HARVARD apparatus, United Kingdom) at 10 μL/min for 15 min.

For the activity assay, the reaction buffer contained 10 mM Tris-Cl (pH 7.3) with 10% glycerol, 250 μM acetyl-CoA, 320 μM (*Z,E*)-9,11-tetradecadienol and 4% DMSO. The DMSO was used as solvent to prepare the stock solution of 8 mM (*Z,E*)-9,11-tetradecadienol. The reaction buffer was run through the system at 10 μL/min using the syringe pump. Fractions were collected from the outlet of the biomicroreactor in sealed glass vials. A batch reaction experiment was set in parallel under the same conditions.

5.1.9   Hexane extraction and measurement of pheromone concentration by GC-MS

Extraction of the organic material from the aq. phase was done with hexane. Dodecyl acetate (0.2 mL of a 0.3 μg/mL soln.) was added to the extract, vortexed for 1 min. The samples were frozen in dry ice, the organic fractions were taken out with a Pasteur pipette, concentrated to ca. 20 μL and analyzed by GC-MS on a HP-5MS column (Agilent Technologies, Madrid, Spain). This step was done in duplicate. Injector and detector (FID) temperature were set to 280°C. The oven temperature was initially set at 80°C and increased at 3°C/min until 280°C, which was held for 10 min. The injections were done in splitless mode at 60 mL/min and a splitless time of 0.6 min. Helium was used as a carrier gas at a flow rate 1.3 mL/min.

5.2   Results and Discussion

5.2.1   Characterization of polyelectrolyte multilayer thickness and morphology

We studied the effect of pH and MW on the thickness of one, three and five layers on flat silicon silanized surfaces and compared the results with those of non-silanized surfaces. The results obtained

for both silanized and non-silanized surfaces (Fig. 5.5(a)-(b)) showed that the thickness of PEM deposited at alkaline pH is larger than the thickness of the layers deposited at acid pH. The same general trend can be observed irrespective of the number of layers. These results can be explained by the adsorption energy, solvency and electrostatic interactions(108). The latter, also known as Coulombic interactions, can be influenced by the surface and polymer charge density, as well as the ionic strength of the solution. Due to the influence of pH on the surface charge density, and to the dissociation of amino groups in the PEI molecules. For instance, in the case of PEI from Fig. 5.5(a), the anchoring layer on the surface screens the negatively charged silanols and shifts the electrostatic interaction towards a covalent bond formation between an amino and an epoxy group. In comparison, on the non-silanized surfaces (Fig. 5.5(b)) the PEI layer is rather thin in all four experimental variations. This is due to the fact that electrostatic forces govern the deposition and once the charges on the Si surface are compensated no further growth takes place.
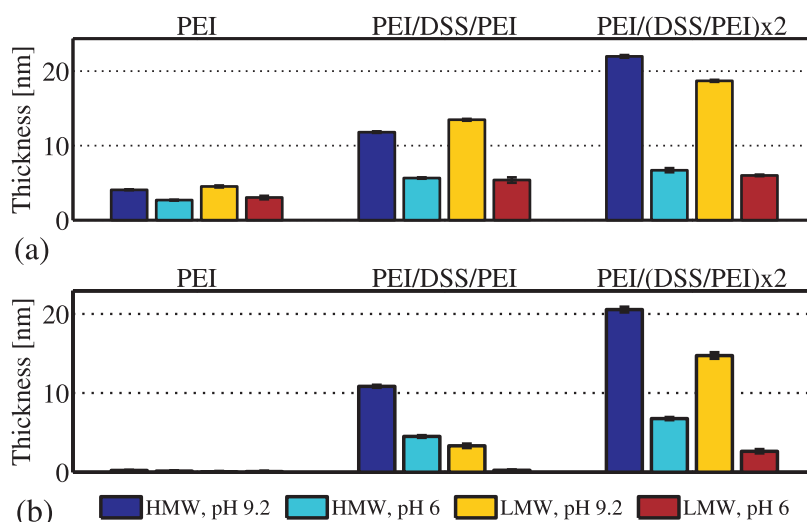
Figure 5.5: Effects of pH and molecular weight of PEI on layer thickness after 10 min incubation. In total five PE layers were generated on planar, (a) silanized with (3-glycidoxypropyl)trimethoxy silane and (b) non-silanized silicon surfaces using PEI with HMW = 750 kDa or LMW = 1.2 kDa.

In the case of anchored PEI/(DSS/PEI)x2, illustrated in Fig. 5.5(a), the buildup reaches 21.9±0.2 nm for the HMW at pH 9.2 because the electrostatic interaction is restored with the lbl deposition. Moreover, LMW at the same pH is approximately 3 nm thinner. Another group is formed by the HMW at pH 6 with 6.7±0.3 nm thickness and LMW at pH 6 for which measured were 6.0±0.1 nm. Strong evidence of the pH influence on the PEI/DSS growth was obtained by AFM step measurement. The results are consistent, within the error, to the experimental values from the Ellipsometry, Table 5.1.

Thus, pH influences significantly the thickness, especially with higher layer number, and therefore is a suitable control parameter for layer thickness.

Table 5.1: **Thickness of PEMs deposited on silanized silicon surfaces.** From the generated AFM scans, the height of step (mean values ± SD) is presented.

	PEI	PEI/DSS/PEI	PEI/(PEI/DSS)x2
HMW, pH9.2	3.9±2.1	15.4±3.5	24.4±4.5
HMW, pH6	3.2±1.2	6.0±1.0	6.7±1.4
LMW, pH9.2	5.3±1.6	12.9±1.4	19.3±2.3
LMW, pH6	1.9±1.5	7.3±1.8	7.8±0.6

The next parameter that influences the deposition of PEM is the adsorption time. The most suitable method for this investigation was to utilize non-silanized surfaces because of the marginal difference between the two types of substrate in terms of growth, especially for high layer numbers. Therefore we measured the non-silanized samples with 5, 10, 15 and 20 min increment between each alternating layer (Fig. 5.6 (a)).
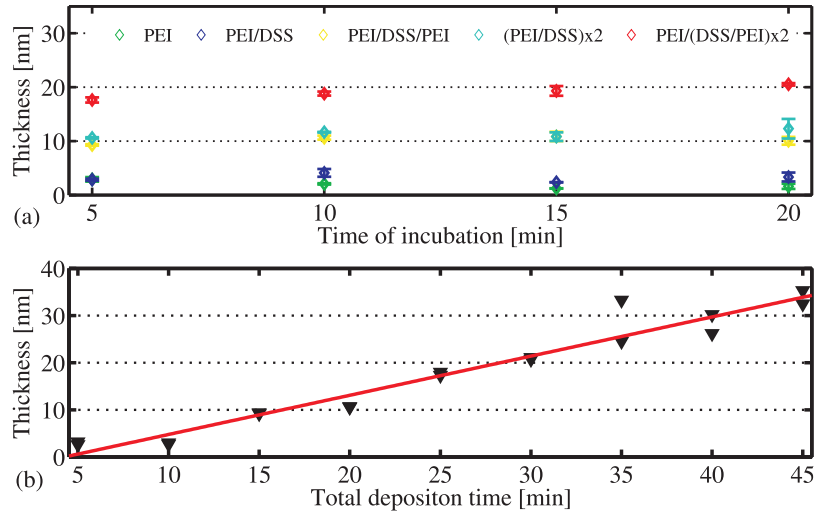
Figure 5.6: Layer thickness versus time of incubation. Five single PE layers were deposited starting with HMW PEI, pH 9.2, and alternating with DSS, pH 3.8. The thicknesses were measured in duplicate by Ellipsometry, one point per sample, after each deposition step. Plotted were: (a) the mean values of thicknesses and standard deviations for increasing incubation times from 5 min. to 20 min.; (b) experimental data (symbols) and fitted function correlating the thickness to the deposition time, R^2 =0.95.

Looking at the mean thickness for five layers, all coatings are within 18 to 21 nm. A similar situation was observed for the mean values measured from the four layer structures: in the same time interval thickness values were in the range of 10 to 14 nm. Based on these results it can be stated that the time of incubation does not influence the deposition process of PEI/DSS multilayer, because the difference in thickness between 5 and 20 minutes of incubation is relatively small within the same number of layers. This finding is in agreement with the work of Müller et al.(105) on

PEI/PAC and the earlier study by Cohen-Stuart et al.(96). The former used ATR-FTIR to study the kinetics and showed a steep ascent for less than 5 min deposition time, which is outside our region of investigation; however for longer deposition times the thickness increased slightly. Therefore, any of the incubation times from the studied interval could be used for deposition in a microsystem and the resulting PEI/DSS thickness would not change within the same layer.

The thickness growth of the PEI/DSS (pH 9.2/3.8) has a linear behavior in time. This trend, which is attributed to the lack of diffusion between consecutive layers, is shown in Fig. 5.6 (b) for 5 min incubation between two single layers. The results are consistent with the findings by Bieker and Schönhoff(98), although these authors applied a different polyelectrolyte couple. By using the established linear growth pattern, it is possible to adjust the thickness of the PEI terminated multilayer coating for more than five layers.

AFM scans, illustrated in Fig. 5.7, show the influence of the number of layers on the morphology and roughness (RMS) of the HMW PEI/DSS coating (pH 9.2/3.8). The coverage of the first layer (a) is already sufficient as the layer appears homogeneous with a granular structured coating. The roughness of this layer is the lowest of all four layers, RMS = 0.41 nm. In the second and third layers the granular structures grow in size which results in increase in roughness from 1.34 nm (b) and to 1.66 nm (c). Although the RMS values differ by 0.22 nm, it can be seen that bulky structures start to form on the surface of the three layer coating (c). Roughness reaches a value of 5.55 nm for layer (d) whilst the grain structure does not alter in comparison to the third layer (c). The influence of time on roughness, for the PEI/PAC couple, has been documented in previous research(105). In their work the authors presumed that an increase in adsorption time would lead to an increase in RMS. In contrast, the current findings on the PEI/DSS couple allow us to assume that roughness increase is dependent on the number of layers even for constant time of deposition.

The PEMs have implicit porous structure, as observed in Fig. 5.7. On the first two surfaces such porosity might result in non-protected silanol groups and consecutive pheromone adsorption because of poor layer coverage and low thickness. Therefore, they were considered unsuitable for modifying the silicon/glass microreactor. The coverage of both layers (c) and (d) would be sufficient to prevent adsorption.

5.2.2 Layer stability in working conditions

The results from the measurements are summarized in Fig. 5.8 (a)-(b), from which it becomes clear that there is no depletion of the surface coating after one week. The coatings have consistent thickness before and after the incubation period for both silanized and non-silanized samples. This means that, in static conditions, without flow, PEM stability is not dependent on the anchoring layer. The PEI/DSS multilayer is stable and suitable for application in a biomicroreactor for pheromone synthesis.
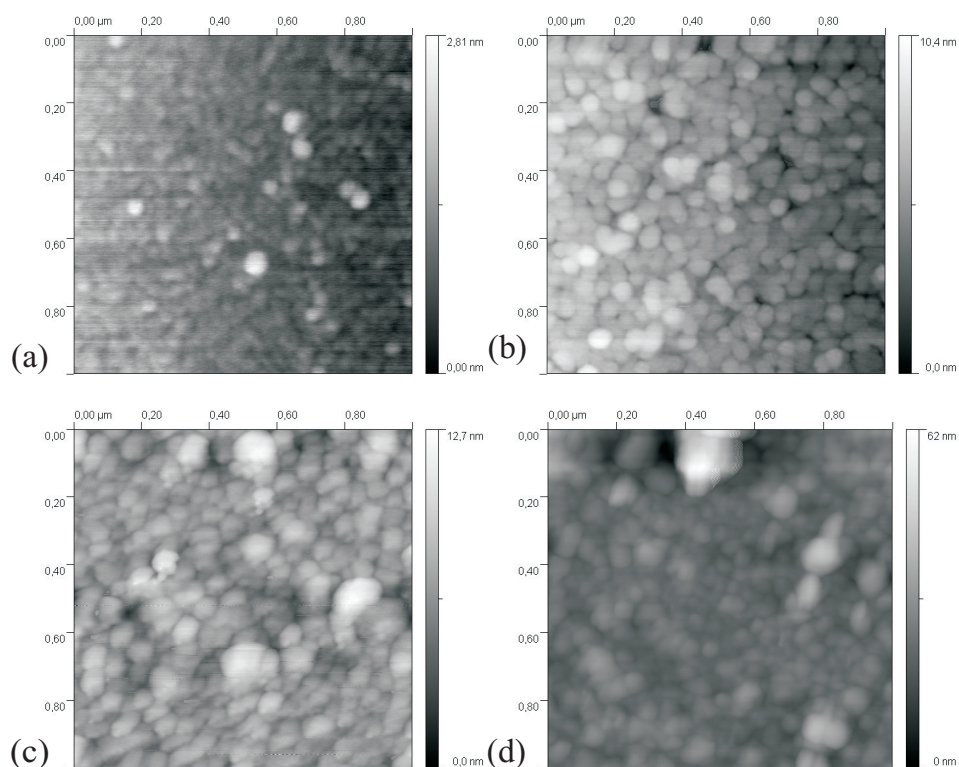
Figure 5.7: AFM scans representing the surface morphology of polyelectrolyte coating. Surfaces after 10 minutes of incubation, on silinated silicon substrate: (a) one layer(PEI), RMS = 0.41 nm; (b) two layers (PEI/DSS), RMS = 1.34 nm; (c) three layers (PEI/DSS/PEI), RMS = 1.66 nm; (d) five layers (PEI/(DSS/PEI)x2), RMS = 5.55 nm

5.2.3 Chemical and biological inertness of PEI terminated coating inside a microreactor

The recovered amounts of dienol and acetate for three different experimental conditions are summarized in Fig. 5.9 as percentage of the initial concentration. The recovered substrate (Z,E)-9,11-tetradecadienol from the syringe and capillary was approximately 38%. The recovered amount was lower in the non-treated system (12%), whereas for the one coated with the five single layers the recovered amount of alcohol increased to 85%. Recovery of the product (Z,E)-9,11-tetradienyl acetate was lower in the three cases, amounting to 4% in the non-coated system, 18% for the syringe and capillary and 60% for the PEM coated microsystem. These data confirm the efficiency of the PEM as anti-adsorption layer (ca. 20x the recovered amount of substrate and product in comparison to the non-coated system).

The substrate recovery is close to the initial concentration. Overall, loss of product may be due to the polar nature of the acetate functional group of the pheromone, which is retained possibly due to interactions with the PEI terminal layer. The exact mechanism of adsorption for the (Z,E)-9,11-tetradecadienol and (Z,E)-9,11-tetradienyl acetate on the weak PEM coating is still not clear. In the authors' opinion, due to the porosity of the PEM coating there might be regions with active negative
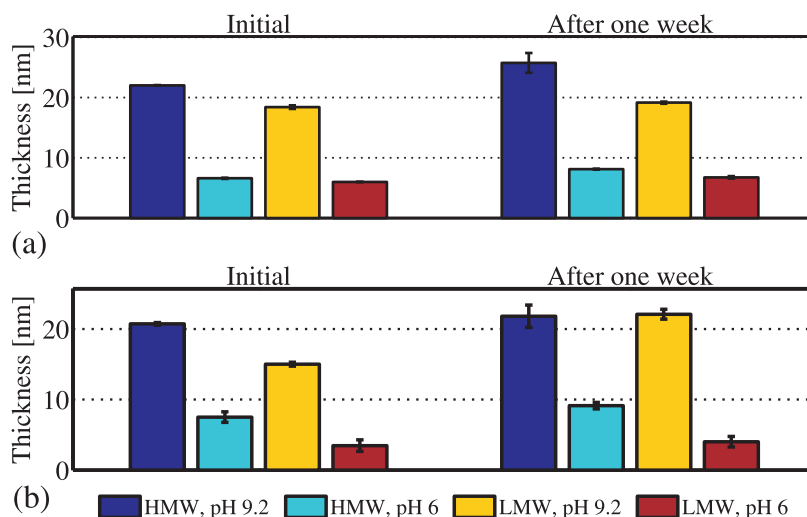
Figure 5.8: Effects of incubation for one week in the specified solution. Five PE layers were deposited on, (a) silanized with (3-glycidoxypropyl)trimethoxy silane and (b) non-silanized, silicon surfaces using PEI with HMW = 750 kDa or LMW = 1.2 kDa.
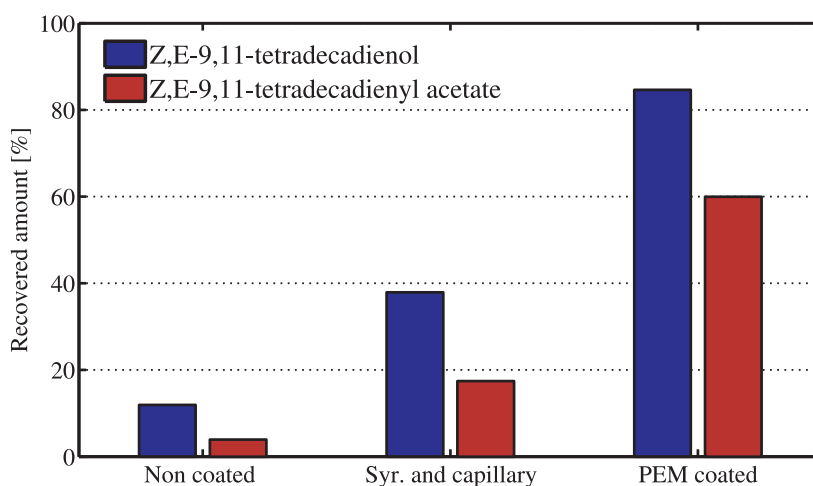
Figure 5.9: Quantification of substrate and product after passing through the microsystem. Amount of (Z,E)-9,11-tetradecadienol and (Z,E)-9,11-tetradienyl acetate recovered after passing through: a non-coated microreactor; non-coated syringe and capillary; microreactor and capillary coated with PEM.

charges either from the Si surface or the DSS. Plausibly, the swelling of the PEM would enhance the effect, by exposing charged sites on the surface. Equally valid, if the charge on the terminal PEI layer approaches zero the repulsion from the surface would diminish and adsorption would eventually take place because of weak interactions. The zero surface charge could be a result of the charge overcompensation, which is assumed to be the driving force for PEM formation during the lbl deposition. Additionally, the ionic strength of the solution could also lead to zero charge, according to the DVLO(110), (111) theory. Nonetheless, the recovered amount for the (Z,E)-9,11-tetradienyl acetate

is 20 times higher from the coated microsystem than from its non-coated counterpart. According to these results the enzymatic reaction should be achievable in a PEM coated microsystem.

Next the effect of the PEM coating on adsorption of protein was studied. The retained His$_6$-EGFP on the walls of the microchannel was determined, and amounted to less than 0.2 μM. A direct comparison between the adsorption behavior of His$_6$-EGFP and His$_6$-atf would be futile, since these two proteins have different amino acid sequences and structure, we can infer it indirectly. The native isoelectric point of His$_6$-EGFP proteins is in the range of 5-6.2(109), which will result in an overall negative charge for His$_6$-EGFP at the immobilization conditions (pH 7.3). On the other hand, atf is positively charged at pH 7.3(154). Therefore, if His$_6$-EGFP molecule is not adsorbed on a positively charged surface, this would mean that no interaction would be expected for the positively charged atf either.

However, in their work on adsorption of lysozyme at a model charged surface, Kubiak-Ossowska and Mulheran(113) argue that electrostatic interactions might not be sufficient to dominate protein adsorption. This opinion is confirmed by Müller et al.(105), who state that adsorption is possible for negatively charged human serum albumin on negatively charged poly(vinylsulfate)(100). Accordingly, such interaction would occur between charged domains of the protein molecule and dissociated polyanion. Although the adsorption behavior of His$_6$-EGFP cannot be translated unconditionally on atf, it provides valuable information about adsorption on PEI terminated coating. The experimental results evidence that PEI/His$_6$-EGFP interactions are weak and reversible.
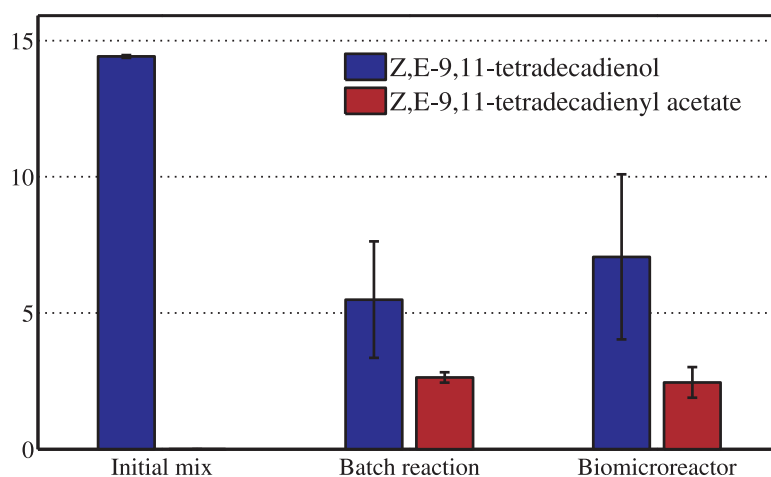
Figure 5.10: Comparison of conversion. The conversion of (Z,E)-9,11-tetradecadienol into (Z,E)-9,11-tetradienyl acetate in batch and after single passing through a biomicroreactor coated with PEM and containing atf immobilized on beads.

5.2.4 Biomicroreactor activity in comparisson with batch activity

The reactions were conducted after thorough washings of the microreactor with buffer solution, indicating that the enzyme was successfully immobilized by coordination bonds to the agarose beads. Thus the PEI/DSS multilayer coating was proved inert towards the immobilized enzyme.

The results from these experiments are illustrated in Fig. 5.10 and show similar conversion in the biomicroreactor and in the batch. Considering the mean values for detected (Z,E)-9,11-tetradecadienol and (Z,E)-9,11-tetradienyl acetate from the batch and PEM coated microreactor there is a loss of approximately 30% in each system, compared to the amount of (Z,E)-9,11-tetradecadienol in the initial mix. Despite the non complete recovery, a working biomicroreactor was presented thus proving the functionality of the anchored five layers coating based on the PEI/DSS.

5.3 Conclusions

In summary, a PEM coated silicon/glass microreactor has been developed to mimic the biosynthetic last step of the pheromone of *S. littoralis*. The PEI/DSS multilayer coating was able to mask the active sites on silicon surfaces, thus considerably reducing adsorption of the substrate and the pheromone. Equally important, the PEI terminated coating demonstrated inertness towards His$_6$-EGFP from which was presumed an identical lack of interaction with the His$_6$-*atf*. The PEI/DSS properties were affected by pH and time of deposition and therefore these parameters could be used to achieve the desired thickness and morphology of the coating.

Our findings would allow to optimize the infochemical pheromone synthesis using biomicroreactors. More generally, the explored PEI/DSS couple could be applied successfully as an anti-adsorption coating in a variety of silicon surfaces using polar substrates.

6

Characterization of the immobilized enzyme and biomicroreactor

Over the last decade immobilized enzyme microreactors (IEMR) have been cited with many advantages over conventional biocatalytic systems. The implementation of microfluidics in enzyme kinetic analysis is expanding fast with impact on vitrotherapeutic methods(114) and biosensing(115), as well as in the basic research on biosynthesis(116; 117) and enzyme characterization(118),(119). There are many advantages of microfluidics to become so influential in biocatalytic research: the small amount of biocatalyst, the possibility of reuse; also the enhancement in mass and heat transfer due to the miniaturization and the high surface to volume ratio of a microsystem. Microreactors enable the characterization of key parameters, the kinetics, K_M and v_{max}, to be determined for immobilized enzymes. In their work Urban *et al.* claim that characterization of new immobilized enzymes can be facilitated by using miniaturized systems in continuous flow mode. Results are obtained using very small quantities of immobilized enzymes and the methods are readily amenable to automation of protocols for enzymatic characterization. Such methods overcome problems with batch assays for immobilized enzymes, e.g. the difficulty of mixing of the solid particles containing supported enzyme with the substrate solution(120).

However there is a downside, due to the uniqueness of each enzyme that is inevitably related to its 3D structure, it is impossible to develop a universal microsystem. Maintaining the functionality of a biocatalyst optimal is a challenging scientific aspect of the marriage between microfluidics and enzymology. Nevertheless, novel techniques and a growing body of literature on the topic help to overcome these difficulties and unveil the complete potential of microfluidics. Factors such as: the type of support activation, presence, distribution and density of functional groups determine the activity yields of an immobilization reaction, and stability and operational stability of the carrier-fixed enzyme. A reduced reaction rate may result from external diffusional restrictions on the surface of carrier materials. Leading to partition effects due to the difference of solubility inside and outside of the carrier, i.e. agarose beads in the current study. The partition must be considered when either ionic or adsorptive forces of low concentrated solutes interact with carrier materials (121),(122). The

most crucial effects are observed in porous particles due to internal or porous diffusion as outlined below. However, a criterion is proposed for evaluation of the impact of mass-transfer on enzyme kinetics in a packed bed microreactor in the work of Kerby *et al.* (118). Their contribution is to elucidate the difficulties in the determination of the exact reaction mechanism in a microfluidic system.

In this study the main focus is on pheromone producing microfluidic bioreactor, i.e. a biomicrore-actor, that uses immobilized *atf* as a biocatalyst. Immobilization is realized via interactions between the Ni^{2+} free orbitals and the imidazolyl groups of two histidines; it can bind proteins with dissociation constant of 10^{-5} to $10^{-7} M$ (123). In general, this chemistry has wide application in immobilized metal ion affinity chromatography (IMAC) and in proteomics. In the current research it is used to immobilize His_6-tagged enzyme (*atf*) on agarose carrier(124), inside a silicon-glass microreactor.

The current work utilizes the biomicroreactor to synthesize (*Z,E*)-9,11-tetradecadienyl acetate ((*Z,E*)-9,11-C14:OAc), the major pheromone compound of *S. littoralis*, for establishing chemical communication between devices. However, to understand better the events occurring inside the system a numerical model is constructed and implemented for determination of the kinetic parameters of the immobilized *atf*. The model conveys a hypothetical mechanism, based on the Michaelis and Menten kinetics(125), for the acetylation reaction and elucidates factors like adsorption and inactivation of the enzyme that hamper the overall conversion inside the system.

The aim of this chapter is to describe the implementation of a silicon-glass biomicroreactor, and a widely accepted concept of the enzyme kinetics on chip, for studying the *atf* towards deeper understanding of its functionality, stability and reaction mechanism. Scientifically, the work is contributing to the field of the biomicrocatalysis by offering a straight-forward and simple numerical model to evaluate the performance of an immobilized enzyme that follows the Michaelis-Menten kinetics.

6.1 Materials and methods

Branched polyethyleneimine (PEI) 50%(wt) solution with molecular weight 750 kDa polycation, and dextransulfate sodium salt (DSS) from *Leuconostoc spp.* as polyanion with molecular weight 500 kDa are used in the layer by layer deposition (lbl) deposition. The cross linking reagent, croton-aldehyde, sodium cyanoborohydride ($NaCNBH_3$), sodium chloride (NaCl), acetate, borate buffer, dodecyl acetate (97%), toluene (anh. GC grade), N,N -dimethyl-formamide (DMF), dimethyl sulfoxide (DMSO, GC grade), glycerol, acetyl Coenzyme A sodium salt (acetyl-CoA), Trizma HCl (Tris-Cl), hydrogen peroxide (H_2O_2, 30%), (3-glycidoxypropyl)trimethoxysilane (97%, GC grade) and sulfuric acid (H_2SO_4, 98%) are purchased from Sigma-Aldrich (Chemie BV, Germany), and used without further modification. The (*Z,E*)-9,11-tetradecadienyl acetate is purchased from Bedoukian (Danbury, USA). The agarose beads are part of His Band purification kit from Novagen (Darmstad, Germany). One side polished 4 inch silicon (1 0 0) wafers are obtained from Okmetic (Vantaa, Finland), 4 inch borofloat glass wafers are purchased from Schott AG (Benelux, Netherlands).

6.1.1 Fabrication of the silicon-glass microreactor

Fabrication of the silicon-glass microreactor followed well established techniques described in Chapter 4. The two variations of silicon-glass microreactors, used in this study, consist of meandering channel with length (L = 9.8 mm) and a rectangular cross-section: the first (W = 250 μm, H = 50 μm); and the second (W = 300 μm, H = 50 μm) for longer retention times. Both variations are studied further in activity assays and by numerical modeling.

6.1.2 Surface modification with anti-adsorption PEM

Firstly, the silicon surface is activated by flushing Piranha (H_2SO_4/H_2O_2 (3:1) volume ratio) through the microchannel for 25 min. Next, the surface is dried thoroughly in a nitrogen flow and by incubation at 100°C for 5 min. Secondly, the surface is silanized with 1.5% γ-glycidoxypropyl trimethoxysilane in anh. toluene, incubation for 4 hrs at room temperature. Afterwards, the channel is rinsed with toluene to discard the non-reacted silanes. Thirdly, the polyelectrolyte multilayer build-up takes place using the lbl deposition technique described earlier (126). In total five layers are deposited, alternating PEI with DSS, thus terminating the build-up with positively charged PEI. The resulting PEM structure is reduced for 1 h with $NaCNBH_3$ aq. soln, then the microreactor is rinsed with acetone anh.

The surface is dried overnight at 30°C and the NTA-functionalized agarose beads are introduced with 100 μL of slurry into the microreactor. The distance between the outlet and the fused-silica capillary is adjusted to prevent leakage of the beads (see Appendix B). Next, the beads are introduced inside the microreactor. The system is washed and charged with Ni^{2+} according to the suppliers protocol (Novagen, Darmstad, Germany).

6.1.3 Charging with Ni^{+2} and His_6 tagged protein immobilization

The charging of the NTA is done with 50 mM $NiCl_2$ aq. soln for 20 min. Then the beads are rinsed with Milli-Q water and straight afterwards with 10 mM Tris-Cl buffer containing 10% Glycerol. The enzyme is introduced inside the system and incubated for 2 h at 4°C. The enzyme is kept on ice whenever possible. The total amount of immobilized enzyme is 10 μg per microreactor. As the final step, the microreactor is washed with 10 mM Tris-Cl buffer before the activity test.

6.1.4 In batch long term activity assay of the immobilized *atf*

The NTA-functionalized agarose beads are introduced with 100 μL of suspended beads into Eppendorff tubes, then washed and charged with Ni^{2+} according to the supplier's recommendation (Novagen, Darmstadt, Germany). Then, 3 μg are incubated in two consecutive steps for 40 min from 10 mM Tris-Cl, pH 7.3, containing 10% glycerol. Next, the beads are shortly washed with the same buffer, then the liquid was decanted and the beads with the immobilized *atf* are transferred in glass vials (4 mL). In each vial 200 μL of reaction mix are added and the reaction is conducted at 30°C

inside an incubator. The reacted mix is collected after 0, 19, 32 h. A control is set in parallel with the same amount (3 μg) of non-immobilized *atf*. The initial mix and the probes, in duplicates, are analyzed after double hexane extraction with GC-MS for content of (*Z,E*)-9,11-tetradecadienol and (*Z,E*)-9,11-tetradecadienyl acetate.

6.1.5 Activity test of the immobilized wax ester synthase (*atf*)

At a concentration of 320 μM of (*Z,E*)-9,11-tetradecadienol the enzyme is working at V_{max} in batch as the concentration is approximately twice the K_M. The purpose is to determine the enzyme activity after immobilization inside the microreactor and to quantify the production of pheromones at different flow rates.

Activity is determined at constant substrate concentration and different retention times inside the microreactor. The reactive mix, described in Table 6.1, is introduced in the microreactor at different flow rates resulting in different retention times. The collected samples for each retention time (Table 6.5) are 200 μL in order to have a direct comparison between the different flow rates and batch. The microreactor is kept inside an incubator and the reactions are conducted at 30°C.

Table 6.1: Reactive mix Dien-ol without Glycerol.

Stock solution	Name	Final concentration	Volume
10 mM	Tris-Cl, pH 7.3	t.f.v.	1309 μl
10 mM	Acetyl-CoA	250 μM	35 μl
8 mM	*Z,E*-9,11-C14:OH	320 μM	56 μl

6.1.6 Microreactor reloading

Inevitably the enzyme activity decreases with time. Therefore, it is necessary to reload the microreactor for continuous usage. The procedure includes stripping off the old enzyme and after recharging the NTA with Ni^{+2} introducing a new enzyme. The *atf* together with Ni^{+2} is removed by flushing 1xStrip buffer at 1 μL min^{-1} for 20 min.

The microreactor is washed with Milli-Q and could be reused again, starting from the charging step or it could be stored indefinitely filled with glycerol at 4°C.

6.1.7 Numerical modeling and calculations

An ODE-based numerical model is constructed and applied to characterize the biomicroreactor, and also as a method to determine the enzyme kinetics and plausible reaction mechanism. In figure 6.1 a schematic representation of the biomicroreactor used for production of main pheromone acetate, (*Z,E*)-9,11-tetradecadienyl, is shown. The rectangular channel has a length L, a width W and a height H. The green element represents an infinitesimal segment n with volume $\Delta V = W \cdot H \cdot \Delta z$.

The volume of the beads is not subtracted from the volume of the segment as the beads are highly porous. Balance for the substrate is derived (eq.6.1) for the infinitesimal volume element of the biomicroreactor in Fig. 6.1.

$$(Z,E)\text{-9,11-C14:OH} + atf \underset{k_b}{\overset{k_f}{\rightleftharpoons}} (Z,E)\text{-9,11-C14:OH:}atf$$

$$(Z,E)\text{-9,11-C14:OH:}atf \xrightarrow{k_r} (Z,E)\text{-9,11-C14:OAc} + atf$$

Acetyl-CoA   HS-CoA
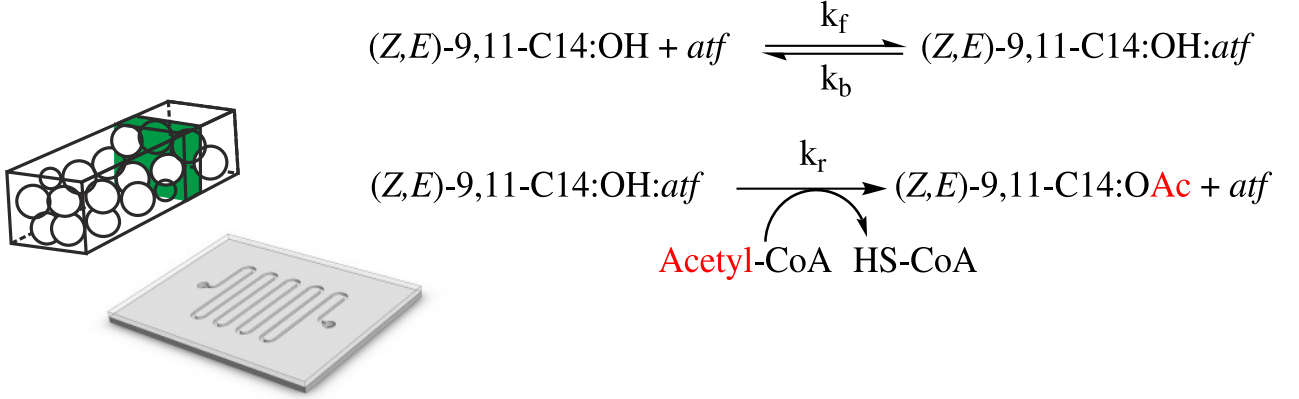
Figure 6.1: Schematic representation of the microreactor and enzymatic reaction. The silicon-glass microrector with a segment of the microchannel packed with NTA-functionalized agarose beads are shown; and the canonical enzymatic reaction, based on the Michaelis Menten kinetics, adapted in the numerical model for the main substrate conversion with the *atf*.

The material balance of the substrate for segment n is the accumulation of substrate, that is the ingoing mass of substrate at position n-1 equals the sum of the outgoing mass of substrate at position n and the substrate converted in product.

$$\Delta V \frac{dS_n}{dt} = S_{n-1} \cdot F_{n-1} - S_n \cdot F_n + r_{Sn} \cdot \Delta V \tag{6.1}$$

Assuming that the density of the reaction mixture is constant, equation (6.1) could be transformed by dividing both sides by ΔV,

$$\frac{dS_n}{dt} = -\frac{\Delta(S \cdot F)}{\Delta V} + r_{Sn} \tag{6.2}$$

By substitution of $\Delta V \to W \cdot H \cdot \Delta z$ and $\Delta S \to dS$ we derive the partial differential equation, as,

$$\frac{\partial S}{\partial t} = -\frac{1}{W \cdot H} \frac{\partial(S \cdot F)}{\partial z} + r_S \tag{6.3}$$

With constant volumetric flow, F, as in the studied case,

$$\frac{\partial S}{\partial t} = -\frac{F}{W \cdot H} \frac{\partial S}{\partial z} + r_S \tag{6.4}$$

To model the dynamics by simulation methods, the partial differential equation (6.1) could be written also as,

$$\frac{dS_n}{dt} = \frac{S_{n-1} - S_n}{\Delta V / F_n} + r_{Sn} \tag{6.5}$$

the expression $\Delta V / F_n = \tau$, is the residence time of the liquid in a single segment. From the expression (6.4), assuming that $\frac{\partial C_S}{\partial t} = 0$, where C_S stands for enzyme-substrate complex, the steady state equation is derived,

$$0 = -v\frac{dS}{dz} + r_S \tag{6.6}$$

which means that the rate of substrate depletion due to product formation with the flow along the channel equals the rate of the enzymatic reaction r_S. For the infinitesimal volume, r_{Sn} is defined by the Michaelis-Menten kinetics as,

$$r_{Sn} = \frac{V_m \cdot S_n}{K_M + S_n} \tag{6.7}$$

The mechanism, firstly described for the invertase by Michaelis-Menten (125), of enzyme kinetics is adapted for the system characterization, and is presented schematically in Fig. 6.1 for the main substrate ((Z,E)-9,11-C14:OH). Accordingly, the mass balance equations for substrate and product can be formulated as,

$$\frac{dS}{dt} = -\frac{k_r \cdot S \cdot E}{\frac{k_r + k_b}{k_f} + S} \tag{6.8}$$

$$\frac{dP}{dt} = \frac{k_r \cdot S \cdot E \cdot F_{AD}}{\frac{k_r + K_b}{k_f} + S} \tag{6.9}$$

In the above (Eq. 6.9) a parameter is introduced F_{AD} to account for the retention of product inside the microsystem. The factor value is derived from an experimental batch reaction of enzyme immobilized on beads. Another important parameter is also estimated from the same set of experiments, the enzyme deactivation constant (K_D), that has the physical meaning of a deactivation rate for the immobilized *atf*. It is included in the following equation,

$$\frac{dE}{dt} = -K_D \cdot E \tag{6.10}$$

In order to solve the system of ordinary differential equations (ODEs)(Eqs. 6.8 - 6.10) a number of experimentally derived parameters are used (Table 6.2).

The system of ODEs is analytically solved in MatLab (MatLab 2008b, The MathWorks, United States) by using fourth-order Runge-Kutta method of integration. The program code is available in the supplementary material, see Appendix B.

Table 6.2: Parameters used in the numerical simulation. These values originate either from the initial parameters or from the experimental data obtained in the long-term stability study; to determination of the activity they are implemented in (Eqs. 6.8 - 6.10).

Parameter description	Symbol	Value	Unit
Immobilized enzyme	E	10	μg
Substrate concentration	S	120	μM
Binary complex formation constant	k_f	variable	μM sec^{-1}
Binary complex dissociation constant	k_b	variable	sec^{-1}
Product formation constant	k_r	variable	sec^{-1}
Enzyme deactivation constant	K_D	1.017	min^{-1}
Adsorption factor	F_{AD}	0.35	—
Product concentration	P	variable	μM

6.2 Results and discussion

Two orthologue enzymes, wax synthase originating from *Acinetobacter* (*atf*) and acyl transferase form *Cumis melo* (CmAAT1), are studied to elucidate which one is more suitable for immobilization on the agarose beads. Enzyme activity and affinity towards the substrate are the two criteria for this choice. Comparison between the enzymes is performed in a series of batch reactions with different concentrations of substrate, and the kinetic parameters are determined graphically from the Michaellis-Menten curves. The results are summarized in Table 6.3. Comparing the obtained parameters for the two enzymes, the CmAAT needs lower substrate concentration to reach its optimum rate, however, the *atf* has higher conversion rate. Based on the findings from these preliminary kinetic studies in batch the *atf* is chosen for the immobilization as it demonstrated higher activity and affinity for the substrate, (*Z,E*)-9,11-C14:OH.

Table 6.3: Kinetic parameters of the CmAAT1 and *atf* for the (*Z,E*)-9,11-C14:OH. (data presented with the permission of G.C.Sans)

Parameter	CmAAT1	*atf*
Km	10μM	160 μM
Vmax	0.6 pKat	5.5 pKat

6.2.1 Pheromone adsorption and operational stability of the *atf* immobilized on beads

The agarose beads allow reutilization after replacing the inactive with active enzyme. Therefore, it is crucial to find the rate of enzymatic inactivation, denoted here as K_D, in order to use the microreactor in an optimal way. To achieve this, a long-term activity assay is performed in batch, corresponding to stop-flow conditions inside the microreactor, using *atf* immobilized on the agarose beads. The *atf*

activity is tested after immobilization on the carrier at several time points (Fig. 6.2). Observed is a decrease in the amount of yielded (*Z,E*)-9,11-tetradecadyenyl acetate with time. The decrease in the conversion is detected immediately after the immobilization of *atf*; it reached zero after 32 hrs at 30°C. According to literature, the two common causes for enzyme deactivation after immobilization are: changes in protein conformation leading to steric hindrance of the active site (127), and/or a diffusion layer around the support that would limit the mass-transfer in and out of the reaction zone, known as transfer effects (121),(122).
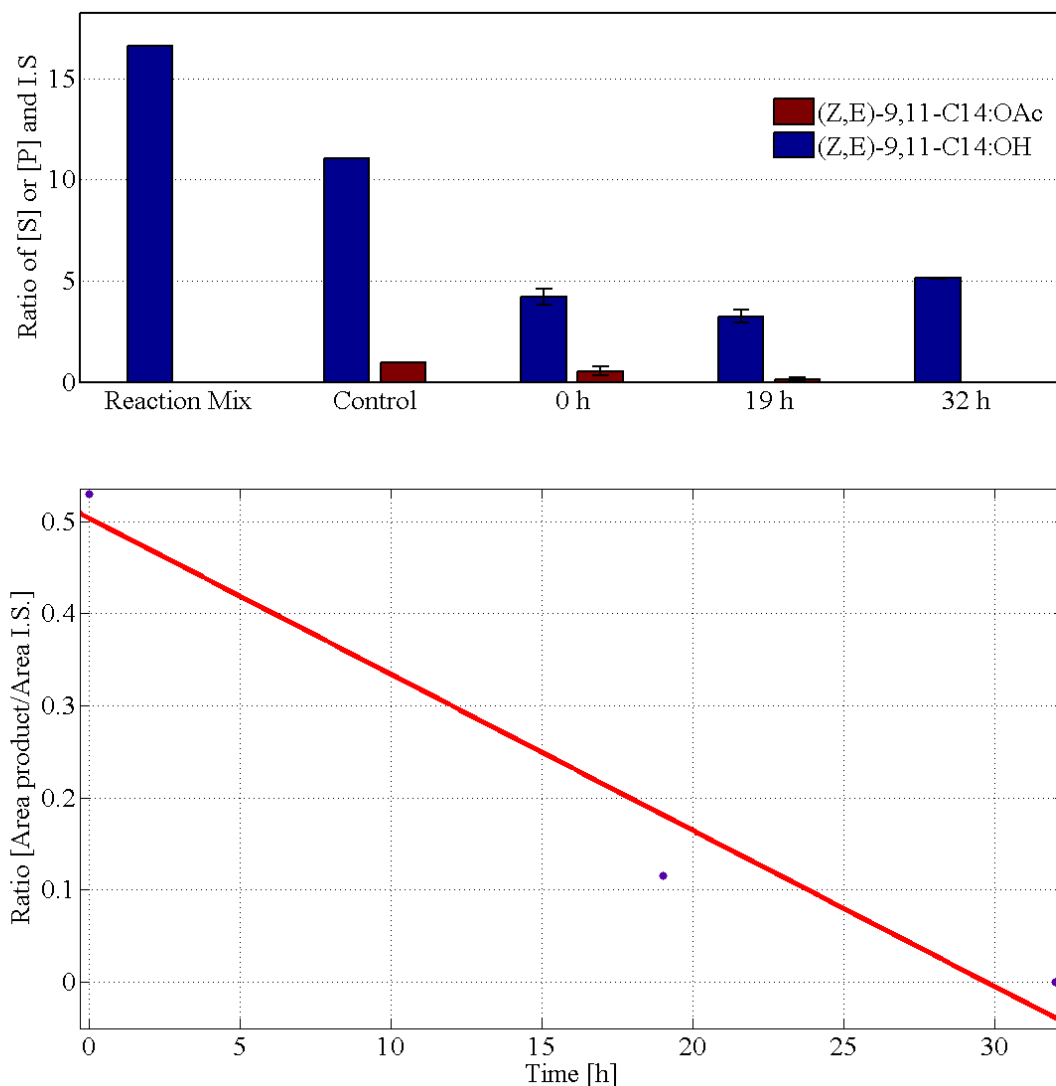
Figure 6.2: Stability of the *atf* immobilized on beads and determination of K_D. The experiments are performed in duplicates as for each assay freshly prepared reactive solutions are added and incubated with the immobilized enzyme: on top, times are plotted versus the recovered amounts of (*Z,E*)-9,11-C14:OH, substrate [S], and (*Z,E*)-9,11-C14:OAc, product [P]; at the bottom, a scatter diagram shows the decay of immobilized enzyme with time, the fit (line) is used to determine the K_D.

The results presented in Fig. 6.2 demonstrated that adsorption is significant between the batch

system containing both the agarose and the enzyme, in contrast to only the enzyme. Namely, 27.8 % of substrate and/or product are retained during the reaction of *atf* in batch in comparison with the initial concentration of the substrate from the reactive mixture (320 μM). One possible explanation for this is that, substrate and/or product are bound to the enzyme or on the walls of the glass vial.

In order to estimate the initial concentration of substrate available during the activity assay, the losses on 50μL packed beads are calculated; considering that the amount of substrate reconstituted from the batch reaction corresponds to the maximum substrate that can be recovered after complete conversion. The substrate loss (%) on the beads only, is calculated as the difference between the substrate from the batch and the substrate recovered in a long term activity test, normalized by the substrate from the batch (Table 6.4).

Table 6.4: Adsorption on the agarose carrier. Loss estimation due to interactions of the substrate, (*Z,E*)-9,11-C14:OH, only with the beads (50μL). Summarized are the substrate areas [S] determined in the GC-MS analysis of the long term activity assay, since the batch does not contain beads (*atf* is dissolved in the reaction mixture) there are no losses.

	Batch	0 hrs	19 hrs	32 hrs
Recovered [S]	11.1	4.3	3.3	5.1
Loss, %	0	61.9	69.8	53.7

The average loss is calculated as the mean and standard deviation (61.8$\pm$8.1(%)) from the three time points (0, 19 and 32 hrs). Practically, this value is used to establish the boundary conditions for substrate after being in contact with the immobilized *atf* on beads; calculated as, $S_{init}\cdot$ 38.2 ($S_{init} = 320\mu$M), resulting in approx. 120 μM of substrate (Table 6.2) that is not retained on the agarose beads and could be utilized by the *atf* inside the microreactor. As the amount of beads inside the microreactor is the same as the amount of beads in batch, according to the supplier's specifications 100 μL of slurry result in 50 μL of packed beads, that same amount is introduced in each microreactor.

A long-term activity assay showed a slight decrease in the activity of *atf* after immobilization. The time versus the product concentration determined in this auxiliary experiment are plotted (Fig. 6.2) and a straight line is fitted, $f(x) = -0.016 \cdot x + 0.503$. The slope of this line is used further in the numerical modeling as the absolute value of $K_D = 0.0169\cdot60 = 1.017$ min^{-1}. The physical interpretation of K_D is the rate of inactivation of the immobilized *atf*. This proves that *aft* loses completely its activity after 32 hours of immobilization. In comparison, the activity of the immobilized Lipozyme IM, studied for the synthesis of esters, remained stable for more than 180 days of continuous working without change in its catalytic activity (128). The results show, that the *atf* has moderate operational stability after immobilization. Nevertheless, the margins of its operational stability allow for short-term experiments as it is demonstrated in the following subchapter.

6.2.2 Kinetic parameters of the enzyme

Next the *atf* is immobilized inside a microreactor and its activity is measured for different flow rates leading to variation of the times of residence inside the system (Table 6.5). The residence time of the substrate and/or product are calculated from the volumetric flow rates as mentioned in equation (6.5) with the assumption that the flow regime inside the microreactor is plug-flow. Mixing is possible inside the microchannel due to the packed beads. However, for an infinite small volume and extremely porous beads the estimation for a plug-flow regime is reasonable (131). The true fluidic regime and the exact retention time of the liquid are out of scope of this study. However, they could be determined with the usage of tracer dyes or other method of flow visualization and image analysis (132). In the current study the flow is pressure-driven; therefore, it also could be expected for a fluid element that is carried along the central axis of the channel to have shorter residence time than the same element moving in proximity to the channel wall. However, because the residence time distribution function is not known, the residence times are expressed as the bulk averages(Table 6.5). Retention time distribution functions are known in literature for packed-bed reactors (132). Exploring those further is not within the scope of this study.

Table 6.5: Flow rates and calculated retention times. Inside the microreactor time of retention for the (Z,E)-9,11-C14:OH is derived from $(\Delta V/F_n = \tau)$; calculated for microreactors having channel width (A) 300 or (B) 250, depth 200 μm and length 91.26 mm.

Flow rates, μl/min	20	10	5	2.5	1.25
Retention time in (A), min	0.3	0.6	1.1	2.2	4.4
Retention time in (B), min	0.2	0.5	0.9	1.8	3.7

The residence time for the two microreactors is plotted versus the determined concentration of (Z,E)-9,11-C14:OH and the yield (Z,E)-9,11-C14:OAc (Figure 6.3). To establish the parameter values for the enzymatic reaction the rate constants ($k_f = 0.2$ μM sec^{-1}, $k_b = 4.3$ sec^{-1}, and $k_r = 25$ sec^{-1}) are established (129) through the numerical model that demonstrated a good correlation to the experimental data. Based on these parameters, the calculated $K_M = (k_r + k_b)/k_f$ is 146 μM, which is somewhat lower than the value determined earlier from the batch reactions. The v_{max} is 9.5 pKat with respect to the conditions inside the microreactor. These are the apparent K_M and v_{max} because the diffusion of substrate from the bulk solution to the microenvironment of an immobilized enzyme limits the rate of the enzyme reactions(133). In fact, the immobilization does not necessarily influence the affinity of the enzyme for a substrate. One example comes from the study on β-galactosidase on silica-alumina (130). To a great extend, this is related to the nature of the biocatalyst. For instance, the K_M of immobilized trypsin via glutaraldehyde linkers had been determined as 25 % of the free biocatalyst (134). In the case of immobilized enzymes, there is also another factor that leads to decrease in the K_M values, partitioning, it has been widely recognized (119), and has been ascribed to the presence of areas of increased substrate concentration on the

surface of the carrier due to electrostatic attraction and hydrophobic adsorption of the substrate on the solid materials (32).

In the current case, the enzymatic reaction is very fast and reaches equilibrium within a single passage of substrate stream through the microreactor channel. In contrast, immobilized lipase acts slower on the substrate; therefore recirculating loop-flow is usually implemented over the immobilized enzyme for reaching complete conversion. The immobilized *atf* reaches a plateau at flow rates below $5 \ \mu\text{L min}^{-1}$ for this architecture and enzyme loading.
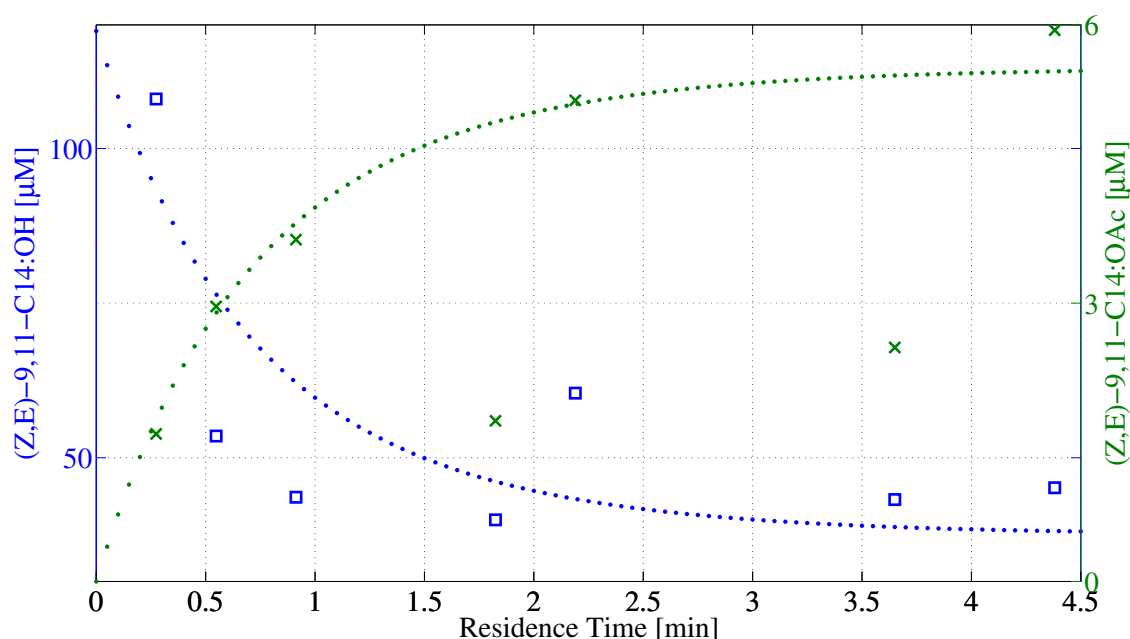
Figure 6.3: Conversion as a function of time presented in a scatter plot. Residence times are plotted versus the substrate (squares) and product concentrations (crosses) recovered from two microreactors with identical amount of immobilised *atf*; the numerical simulation data (dots) are generated for the case of deactivating enzyme and in accordance with the adsorption on beads and microreactor surface.

6.2.3   Efficiency of the conversion inside the microreactor

A comparison is set between the experimental data and the numerical simulation results. Even though the calculated data follows the trend for the experimental results the fit is imprecise in terms of product yield. It is discovered that the experimental data is significantly lower in comparison with its counterpart obtained from the assay with the enzyme in solution. Analyzing the two separate components of the model, the substrate and the product, it is revealed that the numerically generated data is over-predicting the amount of pheromone yield from the microreactor. By modeling it is established that, in reality, the amount of the produced pheromone acetate in the microreactor is 20 % of the expected and about 6 % of the initial substrate. These final results are visualized in

Figure 6.3. One way to interpret the discrepancy between model and experimental values could be the decrease of activity of the *atf* during immobilization inside the microreactor as the process is conducted after introduction on the beads into the microchannel. This is unlikely hypothesis as the flow-rates and cross-section inside the microchannel determine low Re number, hence laminar flow conditions. Moreover, in the last chapter the PEM coating has been proven inert towards the His_6-*atf*. The pending question is, what are the causes of the low levels of measured activity for the immobilized enzyme?

It is observed that the critical component of the simulation, the product, has two points which are strongly deviating from the trend established by the suggested differential equations. Along the design of the numerical simulation a rather statical situations are considered, regarding: the flow-rate, the corresponding retention times; and also the concentration of enzyme. Despite that the F_{AD} coefficient is derived from the experimental data, in order to generate a numerical response as close to reality as possible, it is not resulting from an adsorption isotherm. Hence, the actual adsorption rate might be different from the one considered in the model. This is a dynamic process, and it is highly likely that the two outliers, discussed earlier, are result of fluctuations in the amount of adsorbed product. This means that at certain time more product molecules could be retained per unit surface. Additionally, potential adsorption sites originate from the microreactor. Their contribution to the losses is discussed further.

The strong reduction in yield can be also ascribed to the adsorption inside the microreactor system. Despite the surface modification, adsorption is not completely prevented by the polyelectrolyte multilayer, as demonstrated in the previous chapter 5, the coating has reduced adsorption to 40 % for the pheromone acetate. In the current model two causes for the adsorption of pheromone are contemplated: the first is the interactions with the agarose carrier only; the second considers also the adsorption on the microreactor surface. The former establishes a good correlation between the calculated and experimental data in the case of substrate, which is proved by the close fit (Figure 6.3) of the model to the measured substrate without any additional corrections. On the contrary, if only the adsorption on the beads is considered, for the pheromone acetate, the calculated data is overshooting the experimental results by 80% (not shown here). Despite their similarity in chemical structure, the substrate and product are retained differently on the microreactor coated with PEM, as demonstrated earlier, the pheromone acetate had high affinity towards the surface. It is clear that regarding the adsorption there are more parameters influencing the final result. Nonetheless, the simple model allows for making estimations of the reactor performance. Based on the model it is estimated that the conversion is approximately 6 % of the initial substrate concentration and the reason for this low yield is partitioning of the substrate and product due to both microreactor walls and agarose carrier.

6.3   Conclusion

In summary, the immobilized *atf* was successfully studied with the utilization of microfluidc system and numerical modeling of its reaction kinetics. Via the numerical simulation we estimated the factors that hindered the acetylation inside the microreactor: inactivation of the enzyme with time; adsorption on the beads as well as on the polyelectrolyte surface, possibly in the catalytic pocket of the enzyme. After analyzing the experimental data, it was determined that the adsorption of the product and substrate were the main factors for the observed low conversion. At final, the model was successfully implemented for establishing the kinetic parameters of the immobilized enzyme inside the microreactor by providing easy comparison to the experimental data. Based on the characteristics of the system, detrimental for the initial conditions and the concentration of substrate, the apparent K_M and v_{max} were calculated. To conclude, a methodology for studying immobilized enzyme kinetics was demonstrated on the example of *atf*.

7

Microevaporator and chemoemitter

In the current chapter the main concept of infochemical communication and its realization in the first micro-machine-based chemoemitter mimicking the chemical communication between moths of the genus *Spodoptera* is imparted. The dissipation of pheromones by *Spodoptera littoralis* female moths takes place from the surface of a pheromone gland. Once the volatile blend is evaporated, the signal travels within an air stream; if a male moth detects the scent, it would fly up-stream, follow the message and thus, eventually, locate a female partner for courtship. In nature it is not important what is the amount of evaporated compounds or how much of those are released per unit of time as long as the message is transferred to the male moth. However, for the communication between devices fast, reliable and precisely controlled evaporation is required in order to achieve ratiometric coding and encryption of messages through volatiles. The same requirements are also valid for the scientific community of entomologists who are on the pursuit for blend composition and sensitivity of a test subject.

Until recently, the release of chemical stimuli in wind tunnel experiments on insect flight behavior relied mainly on the passive evaporation of volatile chemicals from a lure, usually made from a filter paper or a rubber septum(135). A major drawback is that only the initial dose applied to these lures is specified, while other factors such as chemical affinity to the substrate used, the kind and amount of solvent in application, temperature, airflow above the lure and time of evaporation are often overlooked. Therefore, establishing compound ratios and their emission rates is cumbersome, time consuming and poorly reproducible, especially for low concentrations of volatiles released from such traditional lures. The microevaporator described in this chapter provides benefits over passive release systems, because by controlling the exact composition of the pheromone solution used and the evaporation rate, the content of the plumes can be defined easily.

In the same class of devices the closest would be an evaporator with ultrasound. Even though ultrasonic devices allow to control the release of volatiles, it is often the case that insects are sensitive to the ultrasound emanating from the device. Some species respond to ultrasound within the working frequency range of the devices during mate orientation and courtship (136),(137). To circumvent such source-related side effects it is necessary to exchange the piezo in order to have the system adjusted

to an insect species (138). However, with the microevaporator at hand these parameters can be adjusted: the temperature of the device, from a controller; the flow rates of the pheromone, from a syringe pump; also the air flow above the membrane by the amount of purging gas.

At the beginning of this chapter, evaporation of pheromone acetate is explored from various surfaces with extremely high surface of evaporation, in order to choose the best design towards the ultimate microevaporator. Next, we demonstrate how the evaporation occurs from the microevaporator on the example of standard chemical solvents. Then moth flight bioassays are investigated, proving the principle and showing the practical aspects of the device. Finally, the complete chemoemitter, i.e. biomicroreactor plus evaporator, is tested in a series of EAG measurements.

The main purpose of this study was to design and fabricate a microevaporation device that could precisely control the amount of released volatiles and to explore the capabilities of the device by implementing it for generation of ratios of volatiles. Thus, the chemoemitter will be authenticated as a universal source for coding in entomology bioassays and volatile sensing.

7.1 Materials and methods

7.1.1 Design and microfabrication of the evaporator

The evaporator was fabricated in silicon and glass using micromachining. All the microfluidic elements were fabricated in Si, and the Pyrex wafer contained the heaters and the temperature sensor. The evaporation took place from a silicon membrane (5.00 x 5.00 x 0.04 mm) that was perforated with ca. $4 \cdot 10^4$ micromachined via-holes. Microfluidic channels with rectangular cross-section delivered the mixture of predefined volatile compounds from two inlets to the reservoir (375 nL) located under the membrane (Fig. 7.1).
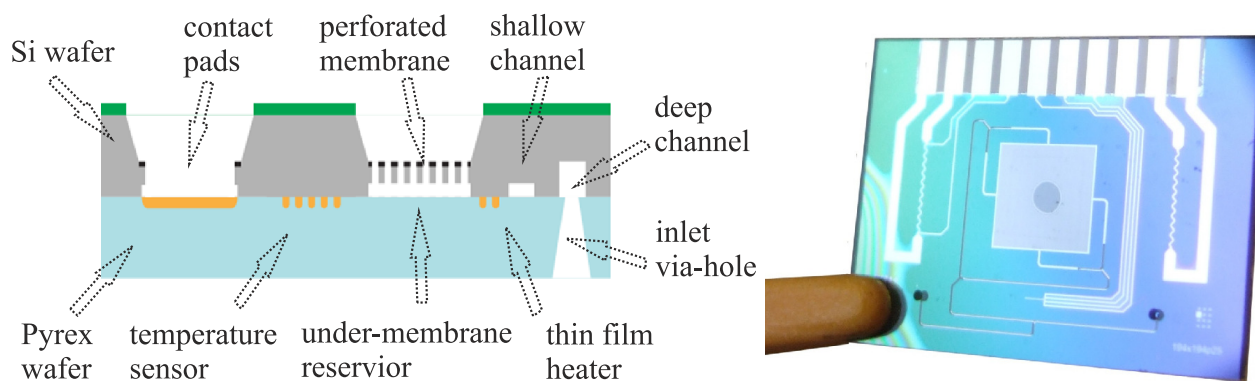
Figure 7.1: Image of the silicon-glass microevaporator and schematic representation of the cross-section through the functional components of the device.

The liquid passed through the membrane and evaporated from small droplets that were formed on the outlet of every via-hole. Two thin-film platinum heaters and a 4-wire resistive temperature sensor

were integrated in the evaporator and worked in a PID loop in order to stabilize the temperature with a variation of 30 mK. The membrane of the silicon-glass evaporator was formed on the top side of the silicon wafer by anisotropic etching in KOH solution. On the backside via-holes through the membrane were etched together with deep channels (100 μm) by DRIE using a mask of photoresist and silicon nitride. After photoresist removal, the shallow channels and under-membrane cavity were etched to 15 μm with the same process. The silicon wafer was anodically bonded to a Pyrex glass plate with powderblasted via-holes and semi-buried Ta (10 nm) and Pt (200 nm) metallization layers of the heaters and the temperature sensor. The silicon-glass stack was diced into separate chips of size 20 x 15 mm.

Microfabrication on the Si wafer

The four inch Si wafer was first cleaned according to the standard process: 10 minutes in HNO_3; second beaker of HNO_3 for 5 minutes followed by quick dump rinsing until the resistivity of the water in the rinser was above 10 MΩ; then 10 minutes in 96°C HNO_3; repeated quick dump rinsing step, followed by spin-drying of the wafer. Next, silicon nitride (SiRN) was deposited on the wafer by LPCVD until thickness 250 nm was reached. Low-pressure chemical vapor deposition (LPCVD) of SiRN was performed in a reactor at a temperature of 800°C and pressure 150 mTorr, as a result of the chemical reaction between the gases SiH_2Cl_2 (77.5 sccm) and NH_3 (20 sccm) were supplied to the reactor as well as N_2 (250 sccm). Film formation occured on both sides of the wafer simultaneously with a deposition rate 4 to 6 nm/min. Photoresist Olin-907-17 was spun on the non-polished side of the wafer at 4000 rpm, after prebacking at 120°C for 30 seconds, the membrane cavity was delineated by photolitography, 3.2 seconds (EVG 601). The non-irradiated photoresist was stripped and the SiRN was removed in 85 % H_3PO_4 acid heated up to 180°C followed by wet anisotropic etching in 25wt% KOH at 75°C with etch rate 1 μm min^{-1}. During this step the thickness of the membrane was defined. In order to etch the under-membrane cavity, photolitography of the hard mask (SiRN) was performed on the polished side of the wafer. After etching the SiRN in the same manner as before, photolitography of the soft mask was done with photoresist (Olin-907-17), thus determining the membrane via-holes, the deep channel and the openings for the electrical contacts. Next, the wafer was etched by DRIE Bosch as deep as 35 μm. The soft mask was stripped. Complete etching of the via-holes was done and the under-membrane cavity was formed with volume 375 nL. Finally, a layer of "black" silicon could be formed on the membrane surface (Adixen SE, Alcatel). After the anodic bonding the actual opening of the contacts could be accomplished by manually removing the thin silicon stripe. The process is schematically presented in Fig. 7.2.

Microfabrication on the Pyrex wafer

A four inch Pyrex wafer was cleaned in HNO_3 for 10 minutes, then immersed in the quick dump rinsing unit and washed until the resistance of the water was above 10 MΩ, after which the clean wafer was spun dry. The photolithography of the metallization spots was done by applying spin-deposition of HDMS followed by spin deposition photoresist of Olin-907-17. Next, the wafer was
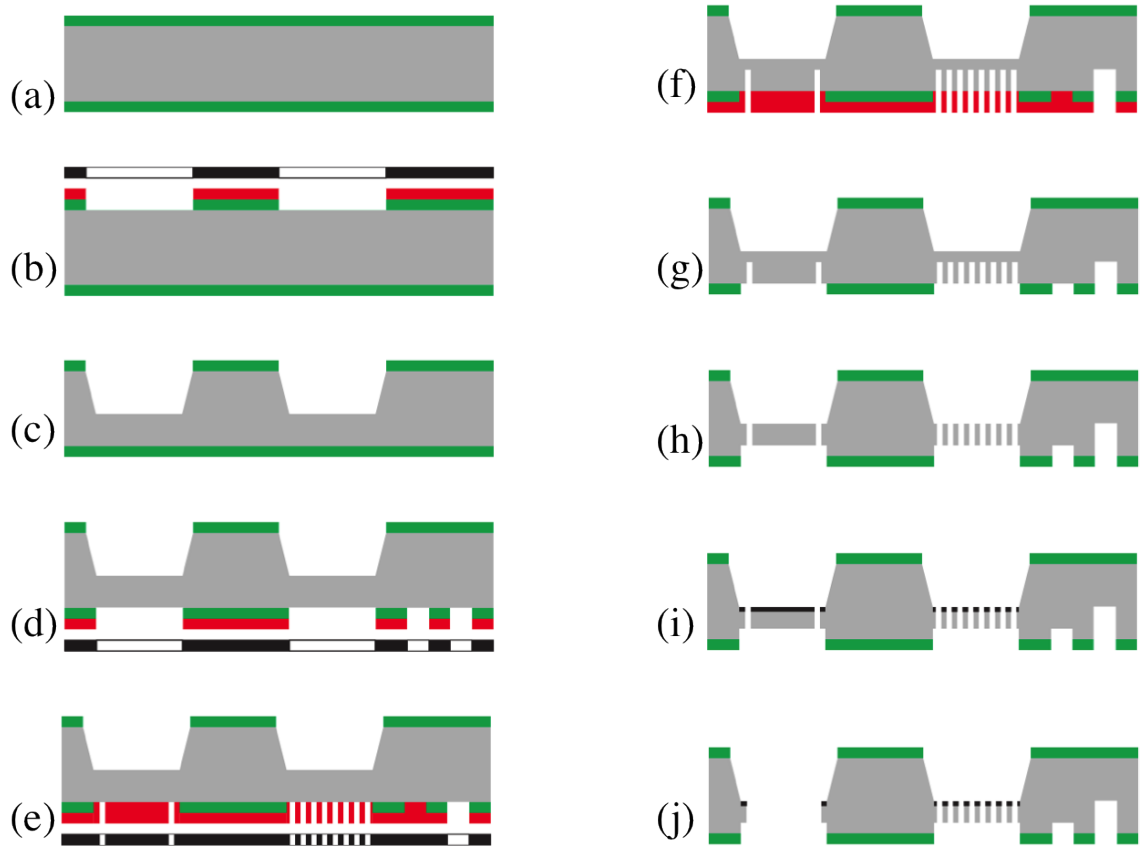
Figure 7.2: Process flow of the Si wafer. Si wafer 4, p-type (100) is used; (a) LPCVD SiRN deposition (250–300nm); (b) photolithography for membrane cavity; (c) KOH anisotropic etching of Si; (d) patterning of SiRN layer; (e) photolithography; (f) DRIE of via-holes and deep channels; (g) photoresist strip; (h) DRIE of shallow channels and sub-membrane cavity; (i) "black silicon" formation; (j) membrane removal.

kept at 95°C for 45 seconds to evaporate the solvent from the resist layer which also hardens the layer. Consecutively, the determination of the metallization area was performed by photolithography (EVG 601, Austria) with exposure of 3.2 seconds. Then the noniradiated photoresist was removed by immersion in OPD4262 (Fuji Film, Japan). Isotropic etching of the Pyrex was conducted in 1% HF until depth of 100 nm was reached, followed by thorough rinsing and spin-drying. Afterwards 10 nm of Ta was sputtered, as adhesion layer for Pt, on the processed surface, followed by Pt layer evaporation until 200 nm thickness. The sacrificial layer of photoresist and sputtered metal was removed in acetone, in a lift-off step (Fig 7.3, e), leaving the Pyrex wafer with microfabricated Pt trenches on one side. The other side of the wafer was covered with photosensitive foil (Ordyl BF 205) and the spots of the inlet via-holes were defined by photolithography. After developing in 0.2 M NaH_2CO_3 aq. soln. and spin-drying, the wholes were powder blasted.

Foil residues were removed manually. The wafer was cleaned in acetone and water consecutively and finally it was spun dry. Lastly, the Si wafer was anodically bonded to the Pyrex glass for 20 minutes at 400°C, 1.8 kV , and the microevaporators (20 x 15 mm) were separated by dicing (Disc DAD, Tokyo, Japan). The complete process is shown in Fig. 7.3.
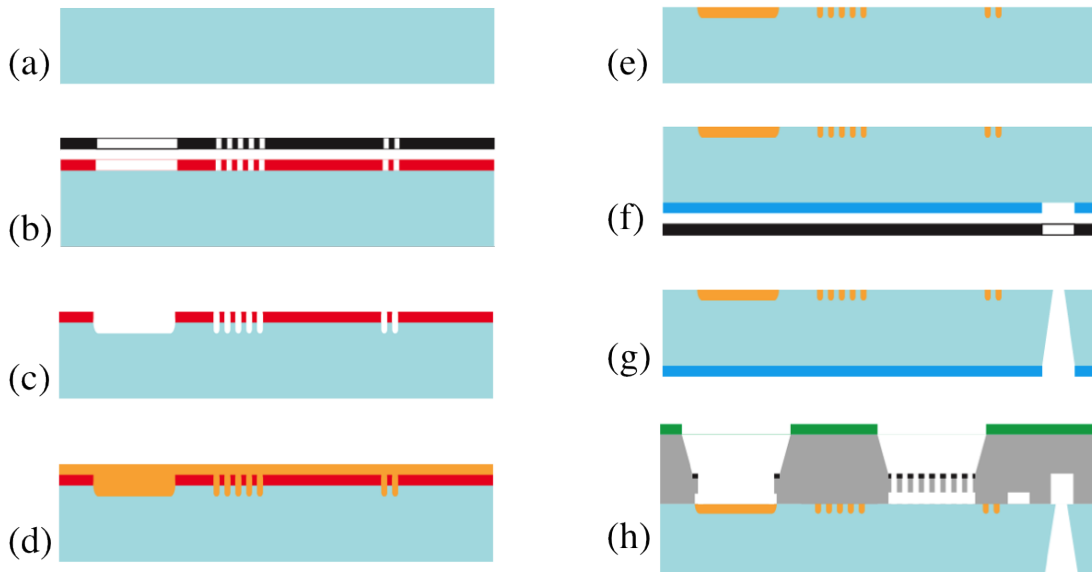
Figure 7.3: Process flow of the Pyrex. Microfabrication on (a) Pyrex 4 wafer; (b) photolitography for metallization spots; (c) isotropic etching of glass in HF; (d) evaporation of Ta/Pt layers; (e) lift-off process; (f) photolithography for via holes; (g) powderblasting; (i) anodic bonding (400°C, 1.8 kV).

7.1.2 Modification and evaporation from silicon surfaces

In these experiments one side polished Si (4") wafers were used as substrates. The wafer surfaces were modified to achieve: porous Si with same thickness but different pore sizes, so called "black" Si, a.k.a. "silicon grass," by directed reactive ion etching (Adixen SE, Alcatel), and carbon nanofibers (CNFs) by growing them by thermal CVD in a mixture of hydrogen/ethylene flow. More details on each of the fabrication methods are given below. All surfaces of the substrates were explored with HR SEM.

A known amount of pheromone acetate (100 μg) was pipetted on each of the surfaces and left to evaporate. The pheromone acetate was placed on top of each surface and then the samples were left to evaporate at room temperature. A probe was collected at a given time point, then the remaining pheromone was extracted from the surface with Hexane to determine the depleted amount of pheromone from the surface. For each time point the difference in pheromone amount was measured after double extraction with hexane of the probed surface. Using internal standard, quantification was performed by GC-MS on the residue from the sample surface.

Porous Si

The porous Si was achieved by etching in HF and simultaneously applying current on the backside of the wafer. Two concentrations of HF aq. soln. were implemented, 5% and 20%. Special attention should be paid in working with HF, where chemically resistant protective gloves and goggles are obligatory. The etching process was completed at a current of 50 mA after 10 min and 5 min, respectively (139). Finishing steps were: thorough rinsing with water, drying and dicing (Disc DaD, Tokyo, Japan).

Black Si

Two gases were used for the DRIE (Adixen SE, Alcatel): SF_6 at 500 sscm flow, etch time of 1 sec; and for deposition C_4F_8 at 200 sccm, 0.2 sec. Pulse alternation took place with 10 msec - "on" *vs* 90 msec - "off". The inductively coupled plasma (ICP - a coil with current that is controlling the plasma generation) was set to 1.5 kW, stage height to 200 mm, temperature at the chuck to 10°C and pressure of He at 10 mbar. The processing time was varied: 6 min or 10 min.

Carbon nanofibers

On a clean 4" one side polished Si wafer was deposited 10 nm Ta, adhesion layer, and 25 nm Ni (Sputterke). The wafer was diced (Disc DaD, Tokyo, Japan) applying a grid to result in square pieces 10x10 mm^2. These substrates were cleaned for 5 min in acetone with ultrasound, then rinsed with DI water and air dried. Next, five of the substrates were placed on a carrier close to the middle of a glass-tube, the tube was connected to a gas line and placed in an oven. The outlet of the tube was connected to an exhaust line. Inside the oven, a ramp was set of 5 °C min^{-1} till 500 °C. At this temperature the substrates were conditioned for 2 h with a mixed flow of H_2/N_2 (1 to 4). Next, the temperature was ramped up with 5 °C min^{-1} to 635 °C, and maintained during the synthesis; C_2H_4 and N_2 are purged simultaneously in ratio 1 to 4, for 30 min. Gradual cooling down was done at a rate of 10 °C min^{-1} until RT, the samples were taken out of the tube and used with no further modifications.

7.1.3 Characterization of the microevaporator

Using a home-build controller and an external thermocouple, clamped on the Si, the integrated heaters of each evaporator were calibrated by a voltage sweep over a range of 8 to 24 V, the nominal power of the evaporator is 1.5 W. The relation between the applied voltage and the actual temperature was recorded, and the coefficients from the linear fit were stored in the memory of the controller. Once this relationship was established further characterization of the microevaporator took place.

Evaporation of solvents and their mixtures

Initially, the evaporator was characterized by introducing common solvents (water, ethanol, hexane) at a pre-set temperature of the microevaporator and using light microscopy to observe the wetting/drying of the membrane. This allowed to determine the critical flow rate at which the surface was completely saturated with liquid. Consecutively, the temperature was raised and again the saturation point was estimated by observation after adjusting the new flow rate at which the membrane was completely wetted. Recorded were the saturation flow rates and their corresponding temperatures.

Evaporation of the pheromone acetate

The target product of the biocatalytic reaction, the pheromone acetate, was evaporated from a 10 ng μL^{-1} solution in hexane or aq. soln containing 4% of DMSO. The temperature of the evaporator was fixed at 120°C as the flow rates were varied from 0.65 to 20 μL min^{-1}. For each flow rate,

the evaporated fraction was adsorbed on a column by Poropack, then extracted and quantified in a GC-MS using an internal standard, dodecadien acetate (3.2 ng μL^{-1}).

Moth flight bioassay

During the behavioral experiment, the evaporator was placed in the far end of a wind tunnel and *S. littoralis* males were released from a platform at the closer end(140). The pheromone, (*Z,E*)-9,11-14:OAc 10 ng μL^{-1} in aq. solution containing 4% DMSO, was introduced into the system with a flow rate of 2 μL min^{-1}. The release rate of the microevaporator was also assessed through a comparative study of the behavioral responses of 20-30 *S. littoralis* males towards : (*i*) 3 virgin females, (*ii*) 10 μg of (*Z,E*)-9,11-14:OAc in hexane deposited on filter paper, and (*iii*) the evaporator emitting the pheromone or the blank, an aq. solution containing only 4%DMSO, was measured in a flight tunnel assay.

7.1.4   Characterization of the chemoemitter

The chemoemitter is characterized with EAG. During the experiment, two of the biomicroreactors were connected inline to effectively increase the residence time in and to reach higher level of conversion. The biomicroreactors were utilized at constant flow provided by a syringe pump (Harvard PhD 2000, Harvard Apparatus) with various flow rates in the two assays. The temperature on the microevaporator was maintained at 120°C throughout the tests.

Antenna collected from male *S. littoralis* were placed on tungsten electrodes under a gas-flow line. The gas line was connected to a carrier gas and an additional compensation line, to avoid shift of the baseline during the measurement. In a third connection, the vapors from the microevaporator were fed into the gas-flow through a Y-junction. Those vapors were generated from the heated membrane and caught by the PMMA cap. The gap with the Si was sealed with a gasket of PDMS and the gas flow was kept constant by a gas balloon connected on one side of the capped microevaporator, shown in Fig. 7.4. The temperature was fixed to 120°C, the air outlet was connected to the tube for the stimulus arrival to the antenna and the air inlet was connected to a 3-way stopcock to produce a puff with the specific stimuli or to clear out the pheromone molecules with a continuous stream of air.

For each stimulus (blank and the pheromone released from the microreactor) 4 replicates and 10 male antennae were considered, and between stimuli the system was continuously cleaned of pheromone molecules by passing an air flow for at least 5 min. The EAG response to the blank corresponds to the precursor alcohol (*Z,E*)-9,11-C14:OH. The EAG responses were normalized to that obtained for 10 μg of synthetic (*Z,E*)- 9,11-C14:OAc, deposited on a filter paper, which was recorded just before each experiment to avoid differences in response due to the use of different antennae or measurements at 5 different lifetimes of the same antenna.
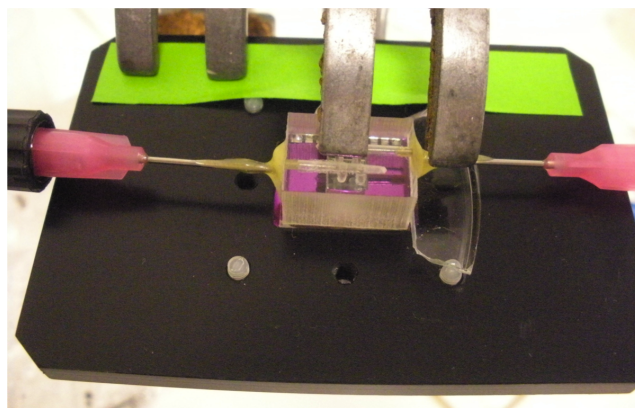
Figure 7.4: Image of the microevaporator placed inside a holder. A PMMA cap is clamped for gas convection; this is the basic assembly of the microevaporator implemented during the EAG and characterization assays.

7.2 Results and discussion

7.2.1 Studying the evaporation from modified surfaces

The evaporation from flat, or relatively flat surfaces in the case of "black Si" and CNFs, was studied in order to determine the influence of surface morphology on the evaporation rate. Surface modifcations that increase the surface to volume rations were deliberately chose in order to gain a vast area of evaporation on top of the membrane. It was considered that for low flow rates, which did not flood the membrane surface, a larger area would improve the rates of evaporation. The main purpose of this experiment was to evaluate the evaporation rates from several surface modifications and determine the one that would enhance the passive evaporation from the membrane. All of the studied surfaces can be implemented on the membrane as it is composed of silicon, just like the flat substrates. The surface with the fastest evaporation rate could be implemented in a microfluidic device to enhance evaporation of liquids with different partial pressures already at room temperature.

The HR-SEM images acquired from each surface modification are summarized in Figure 7.5. Evaporation time lines measured for the different surfaces are shown in Figure 7.6. As expected the different morphologies have different evaporation rates of the pheromone acetate ((Z,E)-9,11-C14:OAc).

According to the work of Tiggelaar *et al.*, the porosity of a 5% HF generated surface should have a BET surface area of 300 m^2/cm^3 opposed to 140 m^2/cm^3 for a 20% HF treated sample(139). In comparison to the polished flat Si sample, that had less surface area than the porous surfaces, the slope observed in Fig. 7.6 is less steep, which is a proof of the interaction between the polar molecule of the pheromone acetate and the Si. The size of the pores did not influence strongly the amount of remaining pheromone as the recovered amounts are similar for the two surfaces treated in 5 % and 20 % HF. Based on the results it can be stated that the porous Si slows the evaporation of pheromone acetate. The increase of surface area within the porous layer, by a factor of 2 according
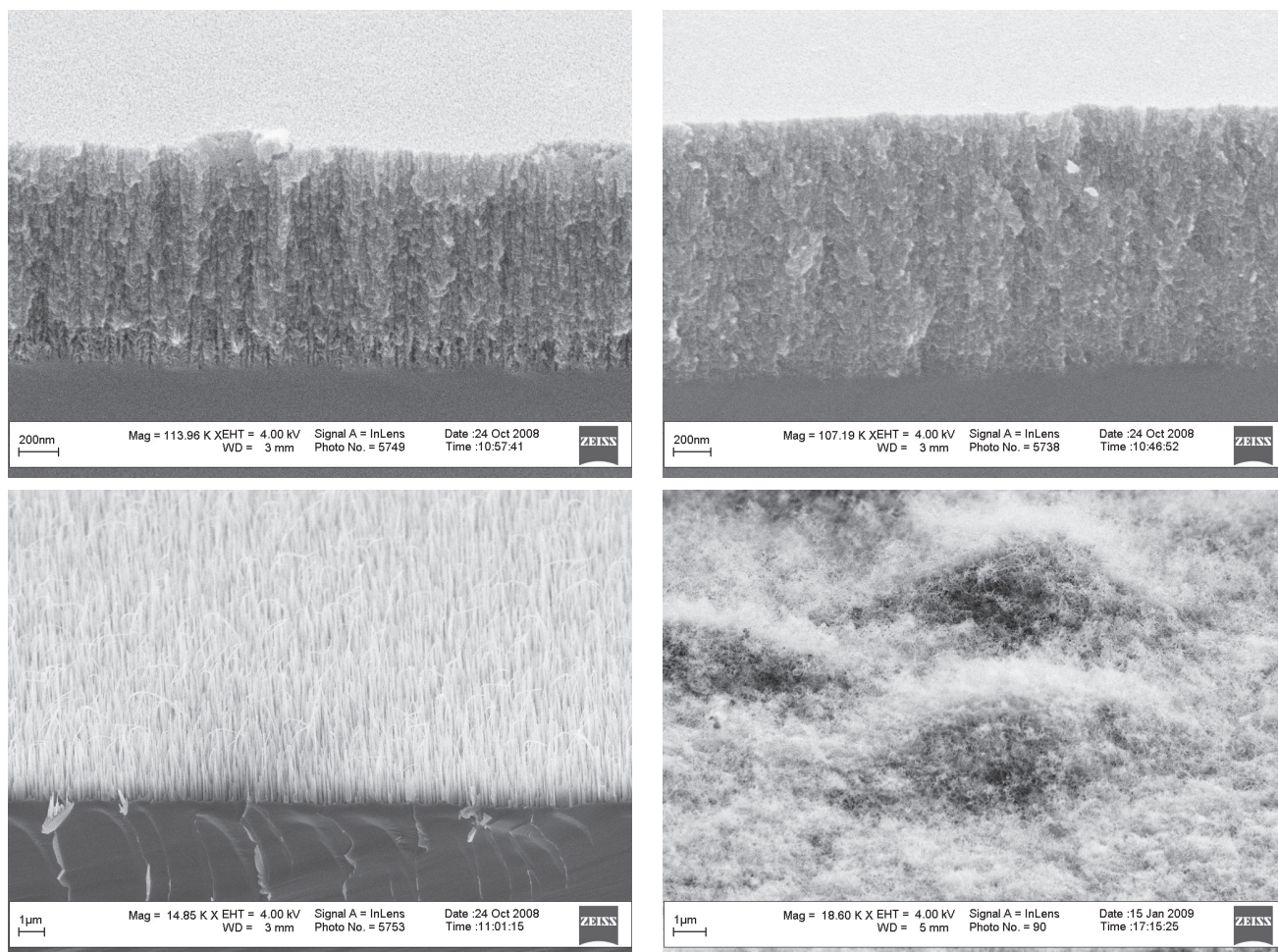
Figure 7.5: Surface modifications used in the evaporation rate studies of (Z,E)-9,11-C14:OAc. On the top, a cross-sections of the porous Si obtained with the 5% HF and the thicker one with 20% HF etching; at the bottom, micrographs of the bSi and the mesh of carbon nano fibers (CNFs).

to BET, is increasing the adsorption and thus hampering the evaporation. This observation confirms our previous findings (Chapter 3 and 4) that the pheromone acetate interacts with silicon.

Next, surfaces were studied with black Si generated after 6 min or 10 min of DRIE. The surfaces demonstrated close evaporation rates, 6.9 versus 7.2 μg cm^{-2} h^{-1}. The thickness of the layer is not changing significantly with longer etching times. Moreover, the evaporation rates are close to the one determined for the polished Si (6.9 μg cm^{-2} h^{-1}). Despite the fact that evaporation occurs only from the surface of the liquid, the evaporation rate is not influenced so much by the increase of area of evaporation. The tendency is supported in the final set of results as the CNFs showed identical evaporation rate as the black Si and marginally lower rate than the polished Si surface. The CNFs have less affinity towards the pheromone acetate than the porous Si. The evaporation rate was less than the one determined from the "black" Si (10 min). Because the process for CNF synthesis is more complex and requires an additional shadow mask for sputtering of Ta and Ni on the membrane,

† The

average evaporation rate is determined from the linear fit to the points as, $\mu\mathbf{g}\ \mathbf{cm^{-2}}\ \mathbf{h^{-1}}$.
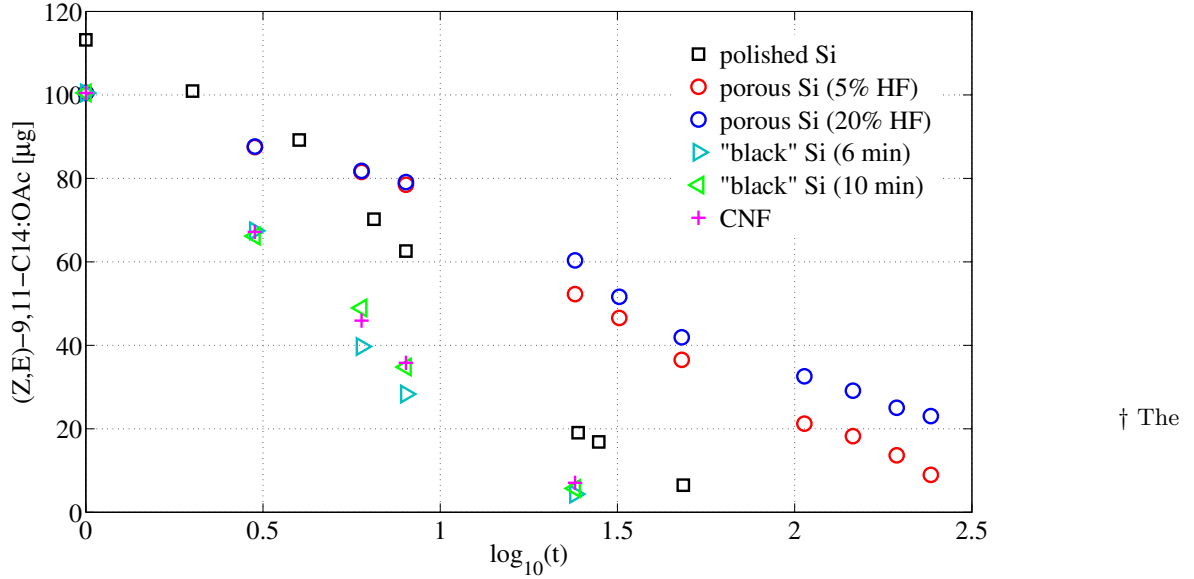
$a\cdot\log_{10}(t)+b$	Polished Si	pSi, 5%HF	pSi, 20%HF	bSi, 6 min	bSi, 10 min	CNF
a	-69.3	-41.2	-34.9	-68.9	-71.9	-68.3
b	121.6	107.9	105.1	99.9	98.9	99.6
R^2	0.9784	0.9829	0.9964	0.9954	0.9864	0.9983
$V^\dagger$	6.9	4.1	3.5	6.9	7.2	6.8

Figure 7.6: Evaporation of dienyl acetate from flat surfaces after modification. In the table the fitting parameters obtained from straight lines through the first four time points are given.

CNFs were discarded as an option for membrane modification.

It is important to note that during the passive evaporation, the effect of the increased surface would diminish when working with volumes of liquid that could cover the surface completely. In that case the evaporation rate would depend only on the area of the membrane and not on the specific surface of evaporation. Considering all of the above arguments it was decided to test two designs: a membrane with polished Si and one modified with black Si. The last choice is based on the argument that the black Si is extremely hydrophobic and would give droplet formation of aqueous solutions on top of the membrane, thus propagating the evaporation from droplets. On the other hand, organic components would spread flat on the surface and would evaporate from the total membrane area.

7.2.2 Initial characterization of the device via evaporation of solvents

Each device was calibrated initially with the purpose to determine the exact temperature as a function of the applied voltage. At low flow rates and without flow, it was observed that the evaporation occurred already from the under-membrane cavity in the case of ethanol and hexane, as they have lower vapor pressure. Wetting of the membrane can be seen in the images of Figure 7.7. Stopped flow

conditions were used to illustrate the retracting evaporation line. Even under the studied conditions, when only two inlets were used to fill the cavity, it can be seen that evaporation takes place both from the chamber and the membrane surface. Therefore, for several flow rates the temperature at which the membrane was completely wetted was registered as characteristic for the studied flow (Fig. 7.7).
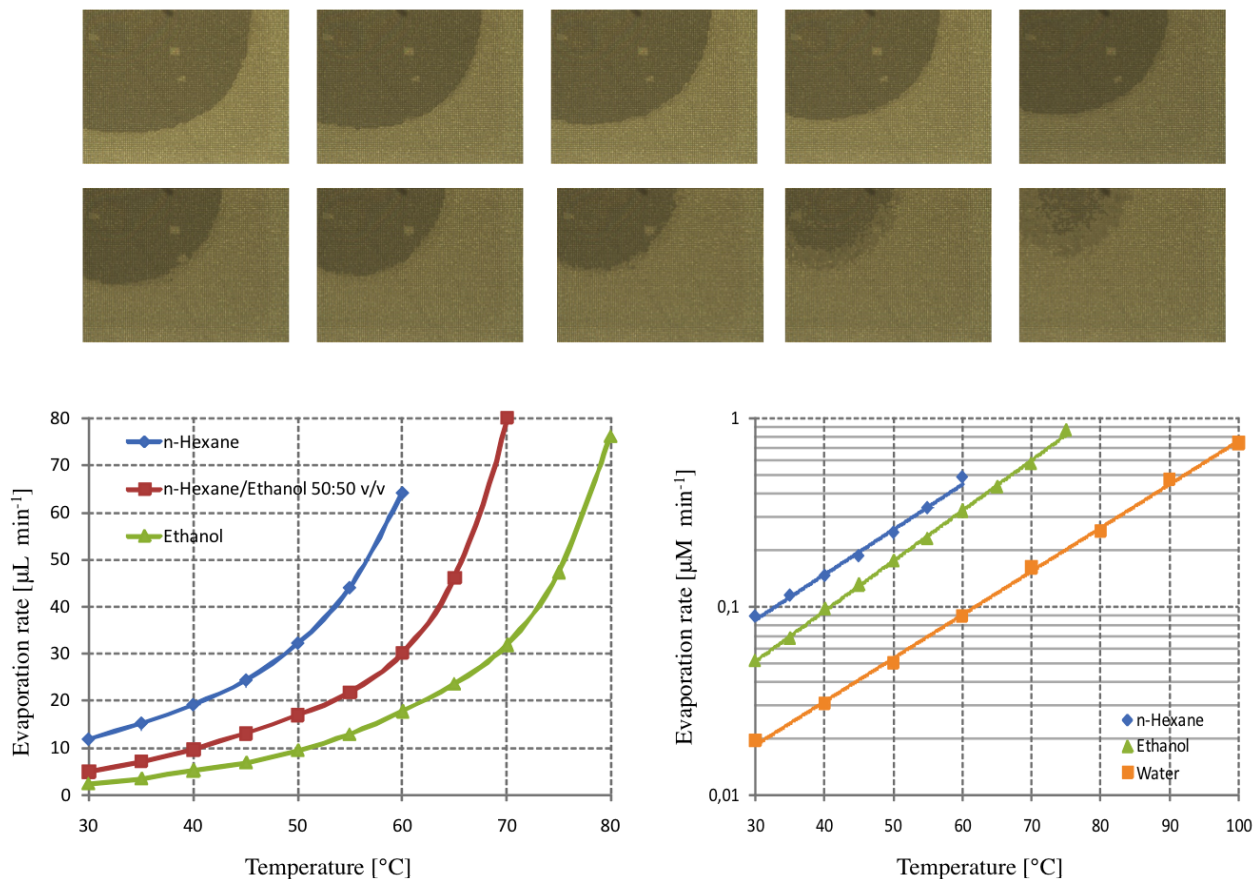
Figure 7.7: Determination of the evaporation rates for water, ethanol and hexane. On top, images of the membrane were acquired every 4 s in a stopped flow mode while evaporating at constant temperature. At the bottom, results obtained by a similar set of observations but for a completely wetted membrane in continuous mode with flow and temperature increase.

In this way the device was tested until the boiling point of each component was reached, e.g. hexane at $69°$C and ethanol at $78°$C. Above the boiling point evaporation took place from the channels. Further increase of the temperature did not influence the evaporation rate; the flow rate could be increased. Even though the flow rate could be increased, 80 μL min^{-1} was considered sufficient when compared to the flow through a functioning biomicroreactor (20 μL min^{-1}) with immobilized *atf*. A mixture of the two solvents resulted in a curve lying between the curves of the pure components, which was expected if one takes into consideration the nature of the solvents (Fig. 7.7). For better visualization, the same results were presented also in semi logarithmic plot (log on the ordinate, μM min^{-1}) to demonstrate linear dependence between the amount of the evaporated solvent and the temperature. In a straight-forward way, an evaporation curve can be generated for

any volatile solvent at atmospheric pressure.

To prove the device applicable for the pheromone, a modification was introduced that restricted the headspace above the membrane and supplied a carrier gas (Fig. 7.4). Variations of the flow rate would influence the temperature on the membrane, however, the PID loop compensates instantaneously and reduces the fluctuations to a minimum. In this configuration the compounds evaporated by the device were quantified after extraction.
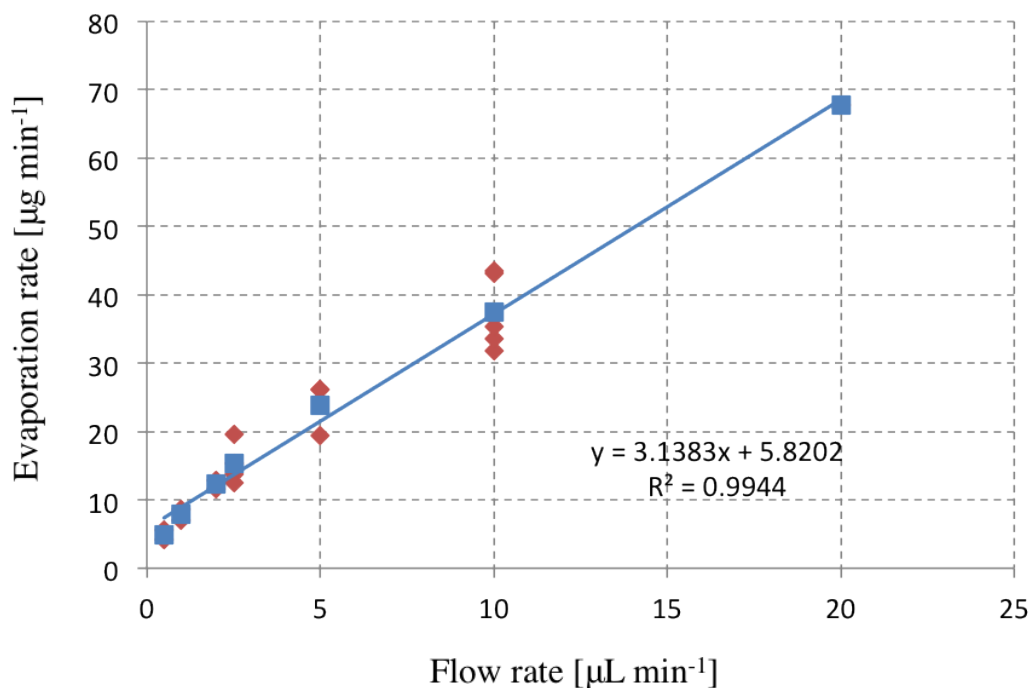
Figure 7.8: Evaporation rate of pheromone as a function of the flow rate. The measurements were conducted at constant temperature (t = 120°C). Rectangles denote the evaporated pheromone from aq. soln. and the rhombs from hexane. A straight line ($R^2 = 0.9944$) was fitted to the experimental data for aq. soln.

The evaporation rate of the pheromone from a glycerol-free solution was determined at a temperature of 120°C as a function of the flow rate. Linear dependence on the evaporation rate for the pheromone acetate from the flow rate was established (Fig. 7.8). Moreover, the straight line is shifted up from the diagonal of the plot by the initial concentration of the solution. This trend emphasizes the fact that no loss occur during the evaporation. To expand on this, the capillaries were coated with the PEM (see chapter 4) to prevent adsorption. On the other hand, the increased temperature of the microevaporator did not promote retention of the pheromone. As a result no loss of the pheromone acetate was observed during the dissipation.

7.2.3   Behavioral response

Insects were subjected to the following attractant sources: three virgin females; the evaporator releasing the pheromone; a paper lure soaked in pheromone; and the evaporator dispensing an aqueous solution containing 4% DMSO, as blank. The pheromone released from the evaporator elicited a similar attraction as the 3 virgin females for most of the flight parameters considered: 97% *vs* 100% taking flight; 90% *vs* 85% males flying to the middle of the tunnel from which 73% *vs* 85% closely approached the platform with the source. Insects failed to contact the source, which is likely related to the high working temperature (120°C) of the microevaporator (Fig. 7.9). In contrast, only 4 insects out of 20 (20%) took off from the platform but neither showed an attractive response nor followed an oriented flight.
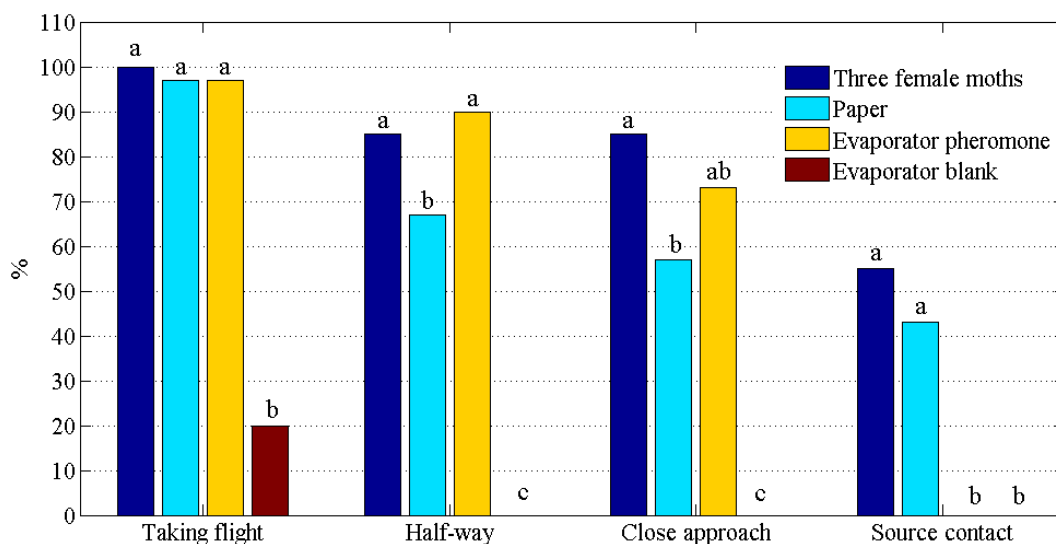
Figure 7.9: Behavioral response of *S. littoralis* males (N=20 for each assay) towards different pheromone sources. Within the same response category, for bars with the same letter marking, the behavior is not significantly different (χ^2 test, P<0.05).

The male moths were as attracted to the micromachined emission as to the 3 virgin female moths. Establishing the exact amount of pheromone released from the three female moths would require a number of additional experiments, whereas its concentration in the evaporator is already known. A blend of volatiles can be tested with the same setup by exchanging the substances on inlet or by adding a compound to the evaporated mixture. Consequently, any assay that involves evaporation and requires a larger number of volatiles, has the advantage of dynamic control over the rates of evaporation of the different compounds by simply regulating the flows.

7.2.4 Electro Antenno Graphy (EAG)

The performance of the entire chemoemitter was assessed by electroantennography. To this purpose, two microreactors, evaporator and EAG were connected to synthesize, evaporate and detect simultaneously the pheromone. The response of the pheromone produced by the two microreactors, connected in series to increase conversion, and to the blank, directly introduced into the evaporator from the syringe pump without passing through the microreactors, was measured using a flow rate of 2 μL min^{-1}. The EAG responses were normalized to the signal obtained from 10 μg of synthetic (Z,E)-9,11-C14:OAc, deposited on a filter paper, which was recorded just before each experiment to avoid differences in response due to the use of different antennae or measurements at different lifetimes of the same antenna. Representative EAG traces of the blank and the pheromone delivered by the microreactor are shown in Figure 7.10 (a). Plotted in Figure 7.10 (b) are the mean responses of 10 male antennae to the probe emerging from the microreactors after partial conversion of (Z,E)-9,11-C14:OH into (Z,E)-9,11-C14:OAc and to the blank. The difference of the mean responses was found to be significant (Student t test, P $<$ 0.01). Hence, it is proved that the signal from the chemoemitter can be detected by EAG and differentiated from the blank sample.
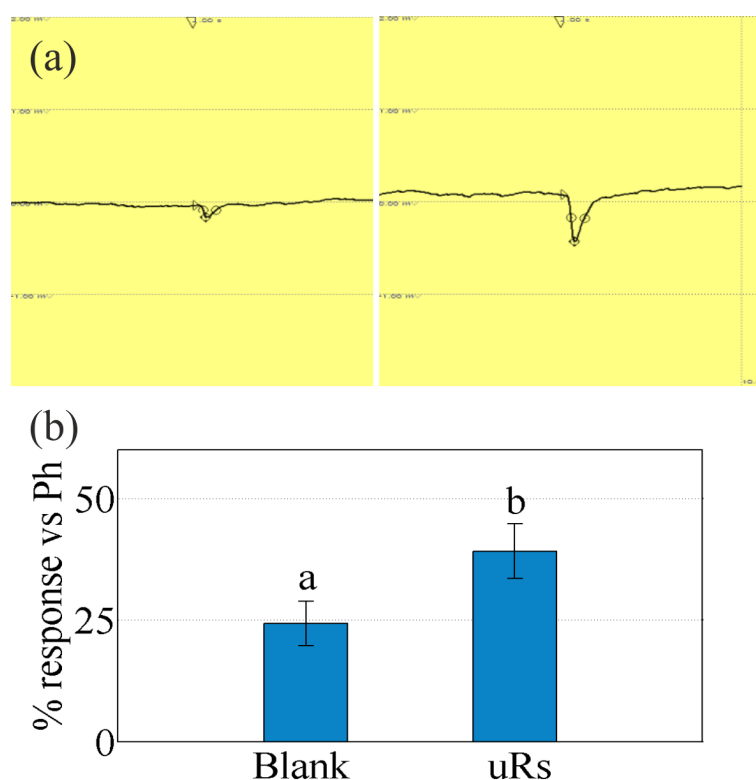
Figure 7.10: Electroantennographic detection of the pheromone produced by two microreactors. Ratios were emitted by the evaporator, in (a) EAG trace of the blank (left) and of the pheromone delivered by the microreactor (right). Mean percentage (b) of the EAG response from 10 insect antennae to the blank and the pheromone released from the microreactors normalized by the response to a filter paper containing 10 μg of synthetic (Z,E)-9,11-14:OAc.

In order to quantify the amount of pheromone released from the microreactor a calibration was performed. A straight line ($y = 1.0658 \cdot x + 3.3392$, $R^2 = 0.9877$) was fitted to the corrected EAG response (pheromone minus blank) to a 10 ng μL^{-1} aqueous soln of pheromone containing 4% DMSO at different flow rates (0.01 to 2 μL min^{-1}). Substitution of the mean EAG corrected response to the pheromone from the microreactor in the plot provided a concentration of pheromone of approximately 5 ng μL^{-1}. This result is consistent with the GC-MS analysis of an aliquot of the pheromone solution coming out of the inline microreactors (3.2 ng μL^{-1}). Thus, the result is corroborating the hypothesis that the chemoemitter can be implemented in quantitative EAG experiment.

Furthermore, by varying the flows through the chemoemitter the ratio of precursor alcohol to pheromone acetate will change. As was demonstrated the EAG is a sensitive technique to detect and quantify those ratios. Most importantly, the great advantage of EAG over the behavioral response is that ratiometric signaling could be observed and statistically argumented.

7.3   Conclusions

We have studied evaporation of pheromone from modified surfaces and established the investigated surface modifications to be significant only at low flow rates and during passive evaporation, without any energy input. We have demonstrated a chemoemitter system consisting of a microreactor and an evaporator that is capable to produce pheromone acetate/alcohol ratios. Furthermore, the chemoemitter pertinence was demonstrated towards behavioral and EAG studies. The implementation of this integrated chemoemitter is expected to contribute strongly to the field of entomology by offering an universal tool for creating plumes of volatiles with a precise control on evaporation rate, concentration and temporal coding.

8

Summary and Outlook

Recent advances in the understanding of pheromone biosynthesis pathways and how pheromone molecules are detected and decoded in a single animal, have inspired the development of a novel class of technology for infochemical communication. Using microreactor technology to design and mimic the final reaction of the biosynthesis of *Spodoptera littoralis*, we investigate and develop a biomicroreactor capable of generating a precise mix of predefined volatile compounds. Coupled to the biomicroreactor is a state-of-the-art microevaporator, capable of creating temporally controlled plumes of volatiles, thus establishing a novel technology for information coding by chemicals. This technological platform will facilitate entomological assays and will enhance neurobiological and behavioral studies as it will ease transmission of time-sensitive and time-registered information through infochemicals.

8.1   From synthesis pathway to microreactor module

The complexity of infochemical communication between insects is presented in **Chapter 2**, together with a short overview of the mechanisms for synthesis and dissipation of volatiles. *In vivo* synthesis employs compartmentalization, each type of cell fulfills different biological functions, also a micoreactor can be designated to a specific biosynthetic function. Using this biomicroreactor approach, modules can be combined and/or rearranged to create a variety of volatile molecules. Moreover, these modules can be multipurpose. For instance the same module can be used for determination of the kinetics of immobilized enzymes or optimization of the reaction conditions. The chapter is introducing examples of the allelochemical communication, the enzymological studies inside microreactors and the current state of technology in volatile dissipation. It accents on the motivation behind the study, namely to provide a toolbox for infochemical research.

A key aspect of the project is immobilization of recombinant enzymes, therefore **Chapter 3** explores strategies for functionalization of Si surfaces. The main consideration is to create a ho-

mogeneous layer with complete coverage by using organosilanes bound via linkers to nitrilotriacetic acid. To achieve this goal three silanes (APTES, TMSPEDA and EDSPA) with varying chemical structure were applied in combination with two linkers (GA and DITC), terminating the layer with chelating compounds. Detailed analysis on the layer build-up is conducted via XPS after each stage of modification. A reference model is used to assess the layer formation and surface coverage. The resulting modified layers deviated from the suggested model structure. Nevertheless, sufficient amount of active sites for immobilization is determined for APTES and TMSPEDA with both of the linkers. Additionally, the interaction between the (Z,E)-9,11-tetradecadienyl acetate and non-treated Si surface is addressed. Evidence is found for the influence of adsorption and importance of surface coating for preventing it.

In the next **Chapter 4**, the established surface modification protocols are implemented inside a silicon-glass microreactor. The resulting layers are investigated by visualization with hexahistidine-tagged enhanced green fluorescent protein (EGFP) and high resolution scanning electron microscopy. Instead of a single layer a multilayer is formed inside the microreactor. In some cases of high organosilane concentration (4% TMSPEDA) the layers detach from the surface. On the contrary the APTES generated layers remain bound to the surface but also with a multilayer aggregation. Despite those layer imperfections the system was considered suitable for enzyme immobilization. However, enzymatic assays show low conversion of the substrate in product, due to partitioning inside the microreactor. This indicates the necessity of a protective layer on the microreactor inner walls and connecting capillaries.

Chapter 5 deals with the adsorption issue, by design and investigation of a polyelectrolyte multilayer coating based on branched polyethylenimine and dextransulfate (PEI/DSS) and layer-by layer deposition (lbl). Initially, the layer is explored after deposition on flat Si substrates with XPS and AFM measurements. Layer formation as a function of molecular weight, pH and time of deposition is explored. The layers show stability after 14 days under working conditions. Being stable and predictable in terms of thickness and morphology, 5 layers are deposited inside the microreactor, then EGFP is used to study the protein adsorption. No fluorescent protein adsorbs on the surface, from which it is deduced that acetyl transferase (*atf*) does not adsorb either. Activity assays with immobilized *atf* on agarose beads inside the microreactor show reduction of the partitioning with only 40% adsorption for the pheromone acetate and about 15% for the pheromone alcohol. Although, the protective layer is not preventing the retention of substrate and product it is sufficient for the functionality of the biomicroreactor.

Characterization of the immobilized enzyme and the performance of the biomicroreactor is conveyed in **Chapter 6**. To investigate the system its components are studied separately. First, the

activity is explored of the *atf* immobilized on the agarose beads. The result from the long-term assays shows medium stability of the enzyme, as it became inactive after 32 h; moreover, it is found that the agarose beads adsorb substrate and/or product. Based on the results, parameters related to the enzyme performance after immobilization are determined. A numerical model is suggested to estimate the reaction mechanism and conversion inside the biomicroreactor. The model is verified by comparison to the experimental data from a continuous flow-through experiment at various flow rates. The model follows fairly well the substrate depletion, however, it deviates strongly from the actual product formation. The reasons for the low conversion and the deviation of the product component are not completely understood. Nevertheless, the apparent Michaelis-Menten constant is close to the experimental one for enzyme in solution, and conversion of 6% from the initially expected substrate concentration in an ideal system. In this configuration the biomicroreactor is used for the integration in the complete chemoemitter system.

The integrated chemoemitter is discussed in **Chapter 7**, where details in the microfabrication of the evaporator are also described. The functionality of the microevaporator is characterized separately with common solvents. Pheromone acetate evaporates from a solution with predefined concentrations and using a head-space technique the vapors are collected and quantified. The amount of evaporated pheromone is as expected proportional to the flow rate without loss of the evaporated compound. Having proved its functionality, the microevaporator is connected consecutively with two biomicroreactors, which together comprise the chemoemitter. Next, the chemoemitter is challenged against traditional lures in a wind-tunnel experiment with live male moths. Although, none of the animals contacted the microevaporator, possibly due to its heated surface, it triggered the same behavioral response as the three virgin female moths. The results from an additional well-established entomological method, electroantennography, proved that feasibility of applying the chemoemitter in quantitative studies. These findings close the chapter on chemoemitter characterization and lead to the final of the monograph.

8.2   Chemical communication outlook

It should be noted that the chemoemitter is essential, but only one part of a more complicated system. Together the biosynthesis and detection pathways, implemented within the frame of the european project (FP6 IST-032275), form a new type of microdevice technology for chemical communication. This project involved five renowned european universities with leading researchers from six diverse scientific fields to provide expertise in: entomology (IQAC(CSIC), Barcelona); microfluidics (University of Twente); sensing (Warwick University); molecular biology (University of Leicester); insect-neurobiology (MPI, Jena); and numerical modeling (University of Leicester). The partners on the project agree that the moth is the ideal model for the development of such a system since

this animal uses a blend of infochemicals, i.e. pheromone blend, in a precisely controlled mix (141), these infochemicals are well-known (142), the biosynthesis steps are well characterized (143; 144), the infochemical mediated behaviour in the animal is robustly reproducible (145; 146), the candidate G-protein coupled receptors (GPCRs) responsible for infochemical detection have recently been identified (150), and the subsequent blend ratio decoding in the animal is well understood (151; 152). Furthermore, the male moth is highly sensitive to the infochemical blend of the female. Chemical communication can be effected with as few as 5-10 molecules hitting the antenna and over distances of several hundreds of meters in favorable conditions.

However, it all starts in IQAC laboratories with the cloning, expression and purification of recombinant enzymes, orthologs to the enzymes involved in the biosynthetic pathways of the moth, in model microorganisms; for the CmAAT1(153) and *atf* (154; 155) *E. coli*; for the desaturase(156) *S. cervisiae* are used. The purified enzymes are immobilized inside the biomicroreactor modules of the chemoemitter, discussed in this thesis. Further, by implementation of the enzymatic reactions inside microfluidic platforms, an original idea to mimic the biosynthetic pathways for pheromone production in a single animal *S. littoralis* was conceptualized. The aim was to realize several bioreactor modules, and each module to host one or more specific reactions such as: chain shortening; desaturation; reduction and acetylation (Figure. 8.1). Hierarchical combination of these modules would closely resemble the processes taking place *in vivo*, as described elsewhere (143; 157).
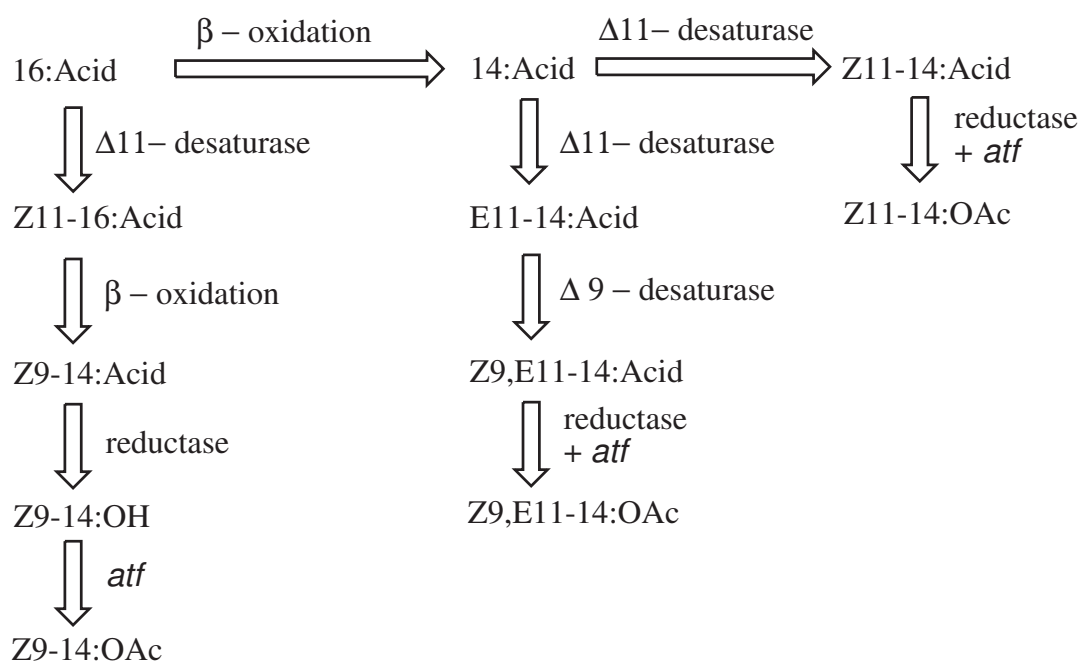
Figure 8.1: The scheme is showing a number of characteristic reactions proposed in the pheromone biosynthesis of *Spodoptera littoralis*.

Some of the concepts were never investigated before, such as the desaturase module had to be realized by generating microsomes that would be entrapped directly inside a microreactor or

in a hydrogel supporting matrix. However, the desaturation takes place in the beginning of the biocatalytic pathway and the product of desaturation module requires a number of intermediate steps before pheromone production, also valid for the β-oxidation. Therefore, a higher priority was granted to the acylation module, exploring the *atf*, which was the highest in the biosynthesis lather and directly yielded the pheromone. Two major factors, that were discussed earlier in this book, influenced the output number of modules: the availability of the enzyme, and the choice of immobilization strategy. Nevertheless, the module-biomicroreactor approach has the potential to match the requirements for controlled ratiometric yield of semiochemicals and is proved by the acylation module described in this thesis.

The evaporated semiochemicals are carried with an air stream towards a sensor device, where a surface acoustic wave (SAW) based detection of volatiles takes place (147; 148). This chemoreceiver is envisaged for the determination of ratiometric and temporal patterns because of its function during binding events. The coated with biological material device would allow to measure minor mass changes on the surface. Moreover, the specificity of detection towards the volatile molecules is enhanced by receptor expressing cell-line that would selectively bind to a given molecule and at the same time would remain dormant towards other molecules. The key specificity in the response of pheromones is considered to be due to the ligand binding 7 transmembrane domain receptors. Pheromone ligands in the moth are thought to have complementary GPCRs, as olfactory receptors (OR) are identified which interface with messenger molecules (149). In a more recent study the GPCRs are proven highly specific detectors of the volatile compound, as evidenced by electrophysiological recordings (150). At final a model mimicking the neuronal-network interactions in moth processes the data from the SAW device. Together the SAW biosensor and the numerical model guarantee, in theory, instantaneous and specific detection of the pheromone.

As stated earlier, the main goal of the project was to establish communication between devices utilizing ratios of volatile molecules, i.e. pheromones. Intriguingly, the interception of biology and technical application gives rather controversial outcomes because communication in nature meets rather different criteria from the widely accepted to-date communication technology. It is required for the communication between two devices to be fast, reliable and independent from outside factors. In contrast, the semiochemical communication is relatively slow, often works on short distances and is influenced by stream and diffusion conditions. In a fundamental research based on the alarm pheromone of ants and sex pheromones of Lepidoptera, Bossert and Wilson suggest mathematical models based on diffusion that prove the low range and temporal dependence of the signal (158). Another discussion from the same work analyses the fade-out effects of trail signals and maximum effect of alarm pheromone in ants; the signal fade-out occurs in minutes and outreaches in the centimeter scale from the source. In contrast, the sex pheromone of the gypsy moth (*Porthetria dispar*) emitted from twelve virgin female moths triggered a response at 3.72 km from the source (159). This and several other examples help Bossert and Wilson to formulate their hypothesis that the

emission rate of a semiochemical as well as the lower limit of detection are evolutionary optimized with respect to a target function. To this end, the chemical communication is possible between devices, if suitable emitter, volatile compounds and sensor are engaged in the process.

9

Samenvatting

Recente ontwikkelingen in methodes voor feromoon biosynthese routes alsmede hoe een insect feromoon moleculen detecteert en decodeert hebben geleid tot de ontwikkeling van een nieuwe technologie voor info-chemische communicatie. Met behulp van microreactor-technologie kunnen systemen ontworpen worden die de laatste reactie van de biosynthese van *Spodoptera littoralis* nabootsen. In dit proefschrift is de ontwikkeling van een dergelijk chemo-emitter systeem beschreven: een biomicroreactor die gekoppeld is aan een micro-verdamper. Met de biomicroreactor kan een nauwkeurig mengsel van vooraf gedefinieerde vluchtige stoffen gemaakt worden die met de micro-verdamper gecontroleerd en accuraat in damp-wolkjes worden omgezet. Het geheel is een nieuwe technologie voor het coderen van informatie middels chemicaliën. Dit technologische platform versnelt entomologische analyses en verbetert neurobiologische en gedragsstudies, daar het middels info-chemicaliën de overdracht vergemakkelijkt van tijdsgevoelige en tijd geregistreerde informatie.

In **hoofdstuk 2** wordt de complexiteit van info-chemische communicatie tussen insecten besproken, en dit hoofdstuk bevat tevens een overzicht van de mechanismes voor synthese en verdamping van vluchtige stoffen. In vivo synthese behelst zogenaamde compartimentering, d.w.z. dat elk compartiment (of module) van een systeem een eigen (biologische) functie heeft. Dit principe kan ook worden toegepast op een chemo-emitter systeem: een microreactor heeft dan de specifieke biosynthetische functie. Door het combineren van dergelijke microreactor-modules (modulaire biomicroreactoren) kan een verscheidenheid aan vluchtige stoffen gemaakt worden. Daarnaast hebben deze modules meerdere functies. Een biomicroreactor kan bijvoorbeeld gebruikt worden voor het bepalen van de kinetiek van geïmmobiliseerde enzymen, maar ook voor het optimaliseren van reactie parameters. In hoofdstuk 2 worden voorbeelden gegeven van allelochemische communicatie, het gebruik van microreactoren voor enzymologisch onderzoek en de huidige stand van zaken met betrekking tot technieken voor het verdampen van vluchtige stoffen. Dit alles in het kader van het doel van dit proefschrift: het ontwikkelen van een toolbox voor info-chemisch onderzoek.

Een belangrijk aspect van het project is het immobiliseren van recombinante enzymen. In **hoofdstuk 3** zijn methodes voor het functionaliseren van silicium oppervlakken beschreven. Het is noodzakelijk om met organosilanen (verbonden aan nitrilo-azijnzuur middels linkers) een homogene laag te

maken die het gehele oppervlak bedekt. Om dit te bereiken zijn silanen met verschillende chemische structuren (APTES, TMSPEDA en EDSPA) gebruikt in combinatie met 2 linkers (GA en DITC) die resulteren in chelaatvormende eindgroepen. Met behulp van XPS is de opbouw van deze lagen onderzocht, en een referentiemodel is gebruikt om de kwaliteit van de laag opbouw en dekkingsgraad te beoordelen. Hoewel de gevormde lagen afwijken van het model, zijn er in geval van APTES en TM-SPEDA met genoemde linkers voldoende actieve plaatsen voor immobilisatie. Tevens is de interactie tussen (Z,E)-9,11-tetradecadienyl acetaat en niet-behandelde silicium oppervlakken onderzocht: er is informatie gevonden omtrent de invloed van adsorptie en het belang van oppervlaktelagen om dit te voorkomen.

Deze oppervlaktemodificatie protocollen zijn vervolgens toegepast in silicium-glas microreactoren (**hoofdstuk 4**). De laagopbouw is onderzocht middels visualisatie van hexahistidine-gelabeld versterkt groen fluorescent eiwit (EGFP) en hoge resolutie elektronenmicroscopie. In de microreactor wordt een multilaag gevormd, en geen monolaag. In geval van een hoge organo-silaan concentratie (4% TMSPEDA) laat deze laag soms los van de wanden van het vloeistofkanaal, in tegenstelling tot op APTES gebaseerde lagen. Ondanks deze onvolkomenheden zijn microreactoren met deze lagen geschikt voor het immobiliseren van enzymen. Echter, deze systemen hebben een relatief lage enzymatische omzetting vanwege verliezen door wand-adsorptie. Dit onderbouwt het belang van een beschermende laag op de kanaalwanden van de microreactor en capillairen voor vloeistof aansluitingen.

Hoofdstuk 5 gaat over deze adsorptie-kwestie. Beschermende multilagen van polyelektroliet op basis van vertakt poly-ethylenimine en dextransulfaat (PEI/DSS) alsmede laag-voor-laag depositie zijn onderzocht. Na depositie van deze lagen op vlakke silicium substraten is onderzoek gedaan met XPS en AFM. De laagopbouw is getoetst als functie van het molecuulgewicht, zuurgraad en depositie tijd. Alle lagen zijn stabiel aan blootstelling aan de reactiecondities gedurende 14 dagen. Vanwege de stabiliteit en voorspelbaarheid van de beschermende lagen, in termen van dikte en morfologie, zijn 5 verschillende lagen aangebracht in microreactoren, en is vervolgens EGFP gebruikt voor het bestuderen van eiwit adsorptie. Fluorescent eiwit adsorbeert niet aan het oppervlak, en op basis hiervan is geconcludeerd dat acetyl transferase (atf) ook niet adsorbeert. Activiteitsanalyses van atf gemmobiliseerd op agarose deeltjes in de microreactor geven een verlaging van de wand-adsorptie tot slechts 40% voor feromoon acetaat, en ca. 15% voor feromoon alcohol. Hoewel deze beschermende laag de retentie van substraat en product dus niet volledig verhindert, is het voldoende voor de functionaliteit van de biomicroreactor.

Onderwerp van **hoofdstuk 6** is de karakterisatie van het geïmmobiliseerde enzym en de prestaties van de biomicroreactor. Hiervoor zijn verschillende componenten van het system apart bestudeerd. Ten eerste is de activiteit van atf op agarose deeltjes bepaald. Lange-termijn analyses tonen aan dat het enzym middelmatig stabiel is: het wordt inactief na 32 uur; tevens is gebleken dat substraat en/of product adsorbeert aan de agarose deeltjes. Op basis van deze resultaten zijn parameters

vastgesteld voor de enzymatische prestaties na immobilisatie. Het model is gevalideerd met data van experimenten met continue vloeistofstromen voor variërende stroomsnelheden. Het model vertoont een redelijke overeenkomst inzake de afname van het substraat, echter, er is een sterke afwijking ten opzichte van de hoeveelheid daadwerkelijk gevormd product. De redenen van de lage conversie en het verschil in hoeveelheid product (tussen model en meting) zijn niet duidelijk. Desondanks ligt de gevonden Michaelis-Menten constante dichtbij de waarde voor enzymen in oplossing, en 6% conversie komt overeen met de initiële substraat concentratie in een ideaal systeem. In deze configuratie is de biomicroreactor geïntegreerd in een volledig chemo-emitter systeem.

Hoofdstuk 7 bevat een discussie over de geïntegreerde chemo-emitter, inclusief de fabricage van de micro-verdamper. De werking van deze micro-verdamper is getest met algemeen gangbare oplos-middelen. Feromoon acetaat is verdampt uit oplossingen met vooraf vastgelegde concentraties, en met een zogenaamde head-space techniek zijn dampen verzameld en gekwantificeerd. De hoeveel-heid feromoon die verdampt wordt, is zoals verwacht proportioneel met het debiet, zonder verlies van verdampte materie. Na het aantonen van de functionele werking is de micro-verdamper gekop-peld aan 2 biomicroreactoren. Vervolgens is de werking van dit chemo-emitter systeem vergeleken met traditionele lokmiddelen, middels windtunnel experimenten en levende mannelijke motvlinders. Hoewel geen van de vlinders de micro-verdamper aanraakte, waarschijnlijk vanwege het verwarmde oppervlak, bereikte de chemo-emitter bij de mannelijke motvlinders eenzelfde gedragsrespons als drie maagdelijke vrouwelijke motvlinders. De resultaten van een gerenommeerde entomologische methode, electro-antennografie, bevestigden de toepasbaarheid van dit chemo-emitter systeem voor kwantitatief onderzoek.

Bibliography

[1] D. Nordlund, W. Lewis, J. Chem. Ecol. **2**, pp. 211–220 (1976) 3

[2] Beth, Naturwissenschaften **20**, pp. 177–183 (1932) 3

[3] L. Noldus, J. Lenteren, W. Lewis, Physiological Entomology **16**, pp. 313–327 (1991) 3

[4] E. Wilson, Sci. Am. **208**, pp. 100–114 (1963) 3

[5] E. Wilson, Science **149**, pp. 10064–71 (1965) 3

[6] M. Beroza, J. Chromat. Sci. **13**, pp. 314–321 (1975) 4

[7] A. Carlson, B. Hanson, Chemical Senses **28**, p. 269 (2003) 4

[8] A. Christensen, M. Pawlowski, H. Lei, G. Hildebrand, Nat. Neurosci. **3**, pp. 927–931 (2000) 4

[9] J. Vickers, A. Christensen, C. Baker, G. Hildebrand, Nature **410**, pp. 35–56 (2001) 4

[10] A. Raina, W. Wergin, C. Murphy, E. Erbe, Arthropod Structure and Development **29**, pp. 343–353 (2000) 5

[11] P. Ma, S. Ramaswamy, edited by G. Blomquist, R. Vogt, *Insect pheromone biochemistry and molecular biology: The biosynthesis and detection of pheromones and plant volatiles*, pp. 19–51 (2003, Acad. Press) 4, 5, 6

[12] W. Leal edited by G. Blomquist, R. Vogt, *Insect pheromone biochemistry and molecular biology: The biosynthesis and detection of pheromones and plant volatiles*, pp. 447–476 (2003, Acad. Press) 5

[13] J. Murlis, A. Willis, T. Corde, Physiol. Entomol. **25**, pp. 211–222 (2000) 5

[14] S. Olsson, L. Kuebler, D. Veit, K. Steck, A.Schmidt, M. Knaden, B. Hansson, J. Neuroscience Methods **195**, pp. 1–9 (2011) 5, 9

[15] C. Noirot, A. Quenedey, Ann. Rev. Entomol. **19**, pp. 61–80 (1974) 5

[16] R. Howard, G. Blomquist, Annu. Rev. Entomol. **50**, pp. 371–393 (2005) 6

[17] J. Nardi, P. Dowd, R. Bartelt, Tissues and Cell **28**, pp. 43–52 (1996) 6

[18] J. Ferveur, F. Savarit, C. O'Kane, G. Sureau, R. Greenspan, J. Jallon, Science **276**, pp. 1555–1558 (1997) 6

[19] M. Lee, A. Srinivasan, B. Ku, J. Dordick, Biotech. Bioeng. **83**, pp. 20–28 (2003) 6

[20] M. Cazolas, L. Juberthie–Jupeau, Can. J. Zool. **61**, pp. 673–681 (1983) 6

[21] J. Zhu, M. Kozlov, P. Philipp, W. Franke, C. Löfstedt, J. Chem. Ecol. **21**, pp. 29–43 (1995) 6

[22] Y. Li, J. Lee, R. Corn, Nucleic acids research **34**, pp. 6416–6424 (2006) 7

[23] Q. Xiang, B. Xu, D. Li, Biomedical microdevices **9**, pp.443–449 (2007) 7

[24] D. Wang, S. Bodovitz, Trends in biotechnology **28**, pp. 281–290 (2010) 7

[25] J. El-Ali, P. Sorger, K. Jensen, Nature **442**, pp. 403–411 (2006) 7

[26] J. Lim, H. Donahue, Tissue engineering **13**, pp. 1879–1891 (2007) 7

[27] D. Huh, B. Matthews, A. Mammoto, M. Montoya-Zavala, H. Hsin, D. Ingber, Science **328**, p. 1662 (2010) 7

[28] V. Srinivasan, V. Pamula, M. Pollack, R. Fair, *Clinical diagnostics on human whole blood, plasma, serum, urine, saliva, sweat, and tears on a digital microfluidic platform*, Proc. μTAS (2003), pp.1287–1290 7

[29] F. Myers, L. Lee, Lab Chip **8**, pp. 2015–2030 (2008) 7

[30] L. Cao, *Carrier-bound immobilized enzymes: principles, applications and design*, Vch Verlagsgesellschaft Mbh (2005) 7, 11

[31] J. Kricka, G. Thorpe, Trends in Biotech. **4**, pp. 253–258 (1986) 7

[32] W. Tischer, F. Wedekind, Biocatal. Discov. Appl., pp. 95–126 (1999) 7, 69

[33] L. Wong, F. Khan, J. Micklefield, Chem. Rev **109**, pp. 4025–4053 (2009) 7, 8

[34] L. Cao, Current opinion in chemical biology **9**, pp.217–226 (2005) 7

[35] T. Vong, S. Schoffelen, S.F.M. Dongen, T.A. van Beek, H. Zuilhof, J.C.M. van Hest, Chem. Sci. **2**, pp. 1278–1285 (2011) 7

[36] E. Hochuli, W. Bannwarth, H. Dobeli, R. Gentz, D. Stuber, Nat. Biotechnol. **6**, p.1321 (1988) 7

[37] A. Bornhorst, J. Falke, Methods Enzymol. **326**, p. 245 (2000) 7

[38] M. Miyazaki, H. Maeda, Trends in Biotechnology **24**, pp.463–470 (2006) 8

[39] C. Wang, R. Oleschuk, F. Ouchen, J. Li, P. Thibault, D. Harrison, Rapid Communications in Mass Spectrometry **14**, pp. 1377–1383 (2000) 8

[40] V. Gaberc-Porekar, V. Menart, Chem. Eng. Technol. **28**, p. 1306 (2005) 7

[41] I. Paramban, R. Burgos, W. Su, Biotechnol. Bioeng. **86**, p. 687 (2004) 7

[42] T. Laurell, J. Drott, L. Rosengren, Biosens. Bioelectron. **10**, pp. 289–299 (1995) 8

[43] T. Laurell, L. Rosengren, Sens. Actuat. B **19**, pp. 614–617 (1994) 8

[44] G. Seong, J. Heo, R. Crooks, Anal. Chem. **75**, pp. 3161–3167 (2003) 8

[45] Y. Chen, A. Carrol, L Scampavia, J. Ruzicka, Analytical sciences **22**, pp. 9–14 (2006) 8

[46] M. Lilly, E. Hornby, E. Crook, Biochemical Jouurnal **100**, p. 718 (1966) 8

[47] M. Kerby, R. Legge, A. Tripathi, Analytical Chemistry **78**, pp. 8273–8280 (2006) 9

[48] A. Özdural, D. Tonyolac, Z. Demircan, I. Boyaci, M. Mutlu, C. Webb, Chem. Engin. Sci, **56**, pp. 3483–3490 (2001) 9

[49] A. Hadd, D. Raymond, J. Halliwell, S. Jacobson, J. Ramsey, Anal. Chem. **69**, pp. 3407–3412 (1997) 9

[50] R. Girling, R. Cardé, J. Chemical Ecology **33**, pp. 1927–1945 (2007). 9

[51] G. Spangler, M. Greenfield, A. Takessian, Physiological entomology **9**, pp. 87–95 (1984). 9

[52] P. Trematerra, G. Pavan, J. Stored Products Research **31**, pp.43–48 (1995). 9

[53] G. Svensson, N. Skals, C. Löfstedt, Entomologia Experimentalis Applicata **106**, pp. 187–192 (2003). 9

[54] J. Cometto-Muniz, W. Cain, M. Abraham, Chemical senses **28**, p. 467 (2003) 9

[55] M. White, *Heterogeneous Catalysis* (Prentice-Hall, 1990) 12

[56] A. Mills, J. Hockey, J. Chem. Soc., Faraday Trans. 1 **71**, pp. 2398–2404 (1975) 12

[57] A. Dabrowski and V. Tertykh, *Adsorption on new and modified inorganic sorbents*(Elsevier Science, 1996) 12

[58] B. Arkles, Chemyech **7**, pp. 766–778 (1977) 14, 31

[59] G. Hermanson, *Bioconjugate techniques* (Academic press, 1996) 18

[60] J. Russat, Surf. Interface. Anal. **11**, 414 (1988) 24, 26

[61] D. Miller, M. Biesinger, N. McIntyre, Surf. Interface Anal. 33, 299 (2003) 25

[62] T. Yoshida, Bull. Chem. Soc. Jpn. **51**, 3257 (1978) 26

[63] D. Hendrickson, J. Hollander, W. Jolly, Inorg. Chem. **8**, 2642 (1969) 26

[64] M. White, *Heterogeneous Catalysis* (Prentice-Hall, 1990)

[65] A. Mills, J. Hockey, J. Chem. Soc., Faraday Trans. 1 **71**, pp. 2398–2404 (1975)

[66] M. Cho, S. Lee, S. Han, J. Park, M. Rahman, Y. Shim, C. Ban, Nucleic Acid Research **34**, e75 (2006) 25

[67] N. Graf, E. Yegen, T. Gross, A. Lippitz, W. Weigel, S. Krakert, A. Terfort, W. Unger, Surface Science **603**, pp. 2849–2860 (2009) 25, 26, 35

[68] D. Walt and V. Agayn, TrAC Trends in Analytical Chemistry **13**, pp. 425–430 (1994) 18

[69] F. Richards and J. Knowles, J. Mol. Biol. **36**, 231 (1968) 19

[70] D. Rivera, P. Poston, R. Uibel, J. Harris, Analytical Chemistry **72**, pp. 1543–1554 (2000) 28, 29

[71] H. Luckarift, G. Johnson, J. Spain, Journal of Chromatography B **843**, pp. 310–316 (2006) 31

[72] B. Arkles, Chemyech **7**, pp. 766–778 (1977) 14, 31

[73] J. Taylor, H. Swaisgood, Biochim. Biophys. Acta **284**, pp. 268–277 (1972) 31

[74] D. Pappin, J. Coull, H. Koester, J. Villafranca, Current Research in Protein Chemistry pp. 191–202 (1990) 31

[75] D. Walt, V. Agayan, TrAC Trends in Analytical Chemistry **13**, pp. 425–430 (1994) 31

[76] M. Lee, A. Srinivasan, B. Ku, J. Dordick, Biotechnology and bioengineering **83**, pp. 20–28 (2003) 31

[77] B. Smith, Methods in molecular biology **1**, pp.41–55 (1984) 34

[78] N. Graf, E. Yegen, T. Gross, A. Lippitz, W. Weigel, S. Krakert, A. Terfort, W. Unger, Surface Science **603**, pp. 2849–2860 (2009) 25, 26, 35

[79] A. Faure, C. Hoffmann, R. Bazzi, F. Goubard, E. Pauthe, C. Marquette, L. Blum, P. Perriat, S. Roux, O. Tillement, ACS nano **11**, pp. 2273–2282 (2008) 19

[80] A. Chauhan, D. Aswal, S. Kiory, S. Gupta, J. Yakhmi, C. Surgers, D. Guerin, S. Lenfant, D. Vuillaume, Applied Physics A–Material Science and Processing **90**, 581 (2008) 35

[81] P. Poston, D. Rivera, R. Uibel, J. Harris, Applied spectroscopy **52**, pp.1391–1398 (1998) 27

[82] L. Muñoz, G. Rosell, C. Quero, A. Guerrero, Physiological Entomology **33**, p. 275 (2008) 43

[83] M. Cole, J. Gardner, Z. Racz, S. Pathak, A. Guerrero, L. Muñoz, G. Carot, T. Pearce, and J. Challiss *et al.*, in textitSensors , 2009 IEEE (IEEE, 2010) pp. 1358-1361 43

[84] S. Uthoff, T. Stoveken, N. Weber, K. Vosmann, E. Klein, R. Kalscheuer, and A. Steinbuchel, Applied and environmental microbiology **71**, p. 790 (2005) 44, 49, 92

[85] J. Melin, and S.R. Quake, Biophysics **36**, p. 313 (2007) 44

[86] D. Peterson, T. Rohr, F. Svec, J. Fréchet, Anal. Chem **74**, p. 4081 (2002) 44

[87] K. Sakai-Kato, M. Kato, and T. Toyoóka, Anal. Chem **75**, 388 (2003) 44

[88] J. Drott, K. Lindström, L. Rosengren, T. Laurell, Journal of micromechanics and microengineering **7**, p. 14 (1997) 44

[89] T. Honda, M. Miyazaki, H. Nakamura, and H. Maeda, Chemical communications **2005**, p. 5065 (2005) 44

[90] G. Seong, J. Heo, and R.M. Crooks, Anal. Chem **75**, p. 3161 (2003) 44, 60

[91] H. Holmes and J. Kelevy, The Journal of Physical Chamistry **32**, p. 1522 (1928) 44

[92] A. Dabrowski and V. Tertykh, *Adsorption on new and modified inorganic solvents* (Elsevier Science, 1996) 44

[93] R. Iler, Journal of Colloid and Interface Science **21**, p. 569 (1966) 44

[94] G. Decher, J. Hong, and J. Schmitt, Thin solid films **210**, p. 831 (1996) 44, 45

[95] H. Kim, and M. Urban, Langmuir **14**, p. 7235 (1998) 44, 45

[96] N. Hoogeveen, M. Stuart, G. Fleer, and M. Bömer, Langmuir **12**, p. 3675 (1996) 44, 53

[97] S. Shiratori and M. Rubner, Macromolecules **33**, p. 4213 (2000) 44

[98] P. Bieker and M. Schönhoff, Macromolecules **43**, p. 5052 (2010) 44, 53

[99] M. Müller, T. Rieser, K. Lunkwitz, and J. Meier-Haack, Macromolecular Rapid Communications **20**, p. 607 (1999) 44

[100] M. Müller, T. Rieser, P. Dubin, and K. Lunkwitz, Macromolecular Rapid Communications **22**, p. 390 (2001) 44, 56

[101] G. Lindquist and R. Stratton, Journal of Colloid and Interface Science **55**, p. 45 (1976) 44

[102] G. Koper, R. van Duijvenbode, D. Stam, U. Steuerle, and M. Borkovec, Macromolecules **36**, p. 2500 (2003) 44

[103] R. Mészáros, I. Varga, and T. Gilányi, Langmuir 20, p. 5026 (2004) 44

[104] R. Mészáros, L. Thompson, M. Bos, and P. de Groot, Langmuir 18, p. 6164 (2002) 44

[105] M. Müller and S. Paulik, Macromol. Symp., p. 77 (2007) 44, 52, 53, 56

[106] J. Yakovleva, R. Davidsson, A. Lobanova, M. Bengtsson, S. Eremin, T. Laurell, and J. Emnéus, Analytical chemistry **74**, p. 2994 (2002) 44

[107] S. Chang, K. Gooding, and F. Regnier, Journal of Chromatography A **120**, p. 321 (1976) 45

[108] G. Fleer, *Polymers at interfaces* (Springer, 1993) 51

[109] T. Lee, and A. Feig, RNA **14**, p. 514 (2008) 56

[110] B. Derjaguin, and L. Landau, Acta Physicochim. USSR **14**, p. 633 (1941) 55

[111] E. Verwey, and J. Overbeek, *Theory of the stability of lyophobic colloids* (Elsevier, 1948) 55

[112] T. Stoveken, R. Kalascheuer, U. Malkus, R. Reichelt, and A. Steinbuchel, Journal of Bacteriology **187**, p. 1369 (2005) 56, 92

[113] K. Kubiak-Ossowska and P. Mulheran, Langmuir **26**, p. 7690 (2010) 56

[114] J. Qiao, Q. Li, M. Xiaoyu, Yi Chen, Analyst **136**, pp. 2077–2083 (2011) 59

[115] M. Ganesana, G. Istarnboulie, J-L. Marty, Biosensors and Bioelectronics **30**, pp. 43–48 (2011) 59

[116] G. Stojkoviĉ, I. Plazl, P. Ẑnidarŝiĉ-Plazl, Microfluid Nanofluid. **10**, pp. 627–635 (2011) 59

[117] M. Miyazaki, H. Nakamura, H. Maeda, Chemistry letters **30**, p. 442 (2001) 59

[118] M. Kerby, R. Legge, A. Tripathi, Analytical chemistry **78**, pp. 8273-8280 (2006) 59, 60

[119] W.E. Hornby, M.D. Lilly, E.M. Crook, Biochem. J. **98**, p.420 (1966) 59, 68

[120] P. Urban, M. David, N. Goodall, C. Bruce, Biotechnology Advances **24**, pp. 42–57 (2006) 59

[121] L. Goldstein, Methods Enzymol. **44**, p 397 (1976) 59, 66

[122] M. Gloger, W. Tischer (1983), Methods of Enzymatic analysis, 3^d edn. WCH, vol. 1, pp. 143–163 59, 66

[123] J. Wirth, K. Unger, M. Hearn, Anal. Biochem. **208**, pp. 16–25 (1993) 60

[124] G. Seong, J. Heo, and R.M. Crooks, Anal. Chem **75**, p. 3161 (2003) 44, 60

[125] L. Menten, M. Michaelis, Biochem Z **49**, pp. 333-369 (1913) 60, 64

[126] N. Dimov, L. Muñoz, G. Carot-Sans, M. Verhoeven, W. Bula, G. Kocer, A. Guerrero, H. Gardeniers, Biomicrofluidics **5**, pp. 034102 (2011) 61

[127] L.A. DeLouise, B.L. Miller, Analytical chemistry **77**, pp.1950-1956 (2005) 66

[128] R. Garcìa, T. Garcìa, M. Martìnez, J. Aracil, Bioch. Eng. J **5**, pp. 185–190 (2000) 67

[129] W. Chen, M. Niepel, P. Sorger, Genes and Development **24**, pp. 1861–1875 (2010) 68

[130] M. Ladero, A. Santos, F. Garcìa-Ochoa, Enz. and Microbial Technology **27**, pp. 583–592 (2000) 68

[131] C.R. Carrara, E.J. Mammarella, A.C. Rubiolo, Chemical Engineering Journal **92**, pp. 123–129 (2003) 68

[132] D. Swaine, A. Daugulis, Biotechnology Progress **4**, pp. 134–148 (1988) 68

[133] W. Koh, M. Pishko, Sensors and Actuators B **106**, pp. 335–342 (2005) 68

[134] H. Jiang, H. Zou, H. Wang, J. Ni, Q. Zhang, Y. Zhang, Journal of Chromatography A **903**. pp. 77–84 (2000) 68

[135] R. Girling, R. Cardé, J. Chemical Ecology **33**, pp. 1927–1945 (2007). 73

[136] G. Spangler, M. Greenfield, A. Takessian, Physiological entomology **9**, pp. 87–95 (1984). 73

[137] P. Trematerra, G. Pavan, J. Stored Products Research **31**, pp.43–48 (1995). 73

[138] G. Svensson, N. Skals, C. Löfstedt, Entomologia Experimentalis Applicata **106**, pp. 187–192 (2003). 74

[139] R. Tiggelaar, V. Verdoold, H. Eghbali, G. Desmet, J. Gardeniers, Lab Chip **9**, pp. 456–463 (2008). 77, 80

[140] C. Quero, P. Lucas, M. Renou, A. Guerrero, J. Chemical Ecology **22**, pp. 1087–1102 (1996). 79

[141] C. Löfstedt, M. Bengtsson, J. Biol. Chem. **265**, pp. 1381–1387 (1998) 92

[142] C. Linn Jr, W. Roelofs, *Pheromone communication in moths and its role in the speciation process. In Speciation and the Recognition Concept Theory and Application*, ed. D. Lambert, and H. Spencer (John Hopkins University Press, 1995) 92

[143] J. Tillman, S. Seybold, R. Jurenka, G. Blomquist, Insect Biochem. Mol. Biol. **29**, pp. 481–514 (1999) 92

[144] T. Martinez, G. Fabriás, F. Camps, J. Biol. Chem. **265**, pp. 1381–1387 (1990) 92

[145] N. Hillier, N. Vickers, Chem Senses **29**, pp. 499–511 (2004) 92

[146] T. Baker, S. Ochieng, A. Cossé, S. Lee, J. Todd, C. Quero, N. Vickers, J. Comp. Physiol. A, **190(2)**, pp. 155-65 (2004) 92

[147] O. Yamazaki, T. Mitsuyu, K. Wasa, IEEE Trans. Sonics and Ultrasonics, **27**, pp. 369–379 (1980) 93

[148] H. Meier, T. Baier, G. Riha, Microwave Theory and Techniques, IEEE Transactions on **49**, pp. 743–748 (2001) 93

[149] L. Buck, R. Axel, Cell **65**, pp. 175–187 (1991) 93

[150] J. Krieger, E. Grosse-Wilde, T. Gohl, H. Breer, Eur. J. Neurosci. **21**, pp. 2167–76 (2005) 92, 93

[151] J. Meijerink, M. Carlsson, B. Hansson B, J. Comp. Neurol **467**, pp. 11–21 (2003) 92

[152] M. Sadek, B. Hansson, J. Rospars, S. Anton, J. Exp. Biol. **205**, pp. 1363–1376 (2002) 92

[153] L. Lucchetta, D. Manriquez, I. El-Sharkawy, F. Flores, P. Sanchez-Bel, M. Zouine, C. Ginies, M. Bouzayen, C. Rombaldi, J. Pech, and others, J. Agricul. Food Chem. **55**, pp. 5213–5220 (2007) 92

[154] T. Stöveken, R. Kalscheuer, U. Malkus, R. Reichelt, A. Steinbuchel, J. Bacteriology **187**, pp. 1369–1375 (2005) 56, 92

[155] S. Uthoff, T. Stöveken, N. Weber, S. Vosmann, E. Klein, R. Kalscheuer, A. Steinbüchel, Appl. Environm. Microbiology **71**, pp. 760–769 (2005) 44, 49, 92

[156] K. Tripodi, L. Buttigliero, S. Altabe, A. Uttaro, FEBS Journal **273**, pp. 271–280 (2006) 92

[157] L. Roelofs, Proceedings of the National Academy of Science **92**, p. 44 (1995) 92

[158] W. Bossert, E. Wilson, J. Theoretical Biol. **5**, pp. 443–469 (1963) 93

[159] C. Colins, S. Potts, Technical Bulletin **336**, (1932) 93

Appendix A

Elemental analysis and XPS data

- **Calculation of the Oxygen originating from the surface modification** It was established from the survey XPS spectra that the Si originates from SiO_2 as it was detected from the Si 2p at 103.7 eV. Based on the stoichiometric ratio 1:2 (Si:O) in the SiO_2, and on the determined Si from APTES treated surface 26.69 (% at.), the amount of O bound to Si is determined, as 2 x 26.69 = 53.38 % at. Then the difference between the total amount of Oxygen measured on the surface and the calculated value results in, 55.46 - 53.38 = 2.08 % at., that is due to the organosilane, e.g. APTES, which has 3 Oxygen atoms per molecule (in the case of no cross-linking). All values were calculated using two digits after the float, despite the sensitivity of the method towards C, maximum one digit accuracy after the float.

- **Correction of the Carbon originating from the surface modification** The amount of C originating from the layer modifications is calculated as the difference between the C content in a given sample and the C content from the blank (non-treated surface). For instance, the C on the APTES surfcae is determined as, C $1s(_{APTES})$ – C 1s $(_{BLK})$ = 17.04 – 6.07 = 10.97 % at. This value of the C content is later implemented for the ratio calculations.

- **Ratios from the measurements** The elemental ratios from the measurements were calculated as the corrected C versus the element of interest (i.e. N, S, Ni). For example after *Stage I* on the APTES surface was determined 0.80 ± 0.39 % at. N and 10.97 % at. C, after correction, the ratio is calculated as N:C and equals 1:11.72 also the reverse ratios are sometimes considered to avoid working with small decimal numbers.

- **Ratios from the model** The number of atoms was counted and the ratios were calculated from the hypothetical model. For instance in a monolayer of APTES with a single attachment to the surface, no elimination of ethoxy groups, there would be one N atom per 12 C. The reverse ratio can be found in the text also written as C:N is 12.

Spec Band   Pos PosSep B_FWHM FWHM Height %Gauss Area %Area ChiSquared
  1   1 284.79   0.00   1.85 1.85   9624   95 19377 81.80   0.85
       2 286.57   1.79   1.85 1.85   1546   78 3360 14.18
       3 288.39   3.61   1.85 1.85   483   100   951 4.01

Spec Band   Pos PosSep B_FWHM FWHM Height %Gauss Area %Area ChiSquared
  1   1 284.82   0.00   1.90 1.90 11370   83 24775 84.05   0.69
       2 286.69   1.88   1.90 1.90   1689   98 3439 11.67
       3 288.42   3.60   1.90 1.90   625   100 1263 4.29

Spec Band   Pos PosSep B_FWHM FWHM Height %Gauss Area %Area ChiSquared
  1   1 284.83   0.00   1.85 1.85 10856   84 23017 82.46   0.54
       2 286.57   1.74   1.85 1.85   1624   100 3205 11.48
       3 288.36   3.53   1.85 1.85   778   79 1691 6.06

Spec Band   Pos PosSep B_FWHM FWHM Height %Gauss Area %Area ChiSquared
  1   1 284.85   0.00   1.71 1.71 18627   80 37147 82.92   1.01
       2 286.57   1.73   1.71 1.71   3007   100 5468 12.20
       3 288.62   3.77   1.71 1.71   1202   100 2186 4.88

Figure A.1: C1s spectra determined from the surface of a flat Si sample at each stage of the surface modification, as shown in Fig. 3.1 (a).

Table A.1: Element spectra scans on C, N, O, Si and Ni (At. %) are measured from the Si wafer samples for surface (Fig. 3.1 (a)) after each modification stage.

Element	Stage I	Stage II	Stage III	Stage IV
C	17.0 ± 3.3	20.6 ± 1.7	19.0 ± 0.6	32.9 ± 4.4
N	0.8 ± 0.4	0.7 ± 0.1	1.1 ± 0.3	0.8 ± 0.1
O	55.5 ± 2.8	52.7 ± 1.4	53.6 ± 0.9	44.7 ± 2.7
Si	26.7 ± 0.9	26.0 ± 0.4	26.3 ± 0.1	21.2 ± 1.8
Ni	—	—	—	0.3 ± 0.2
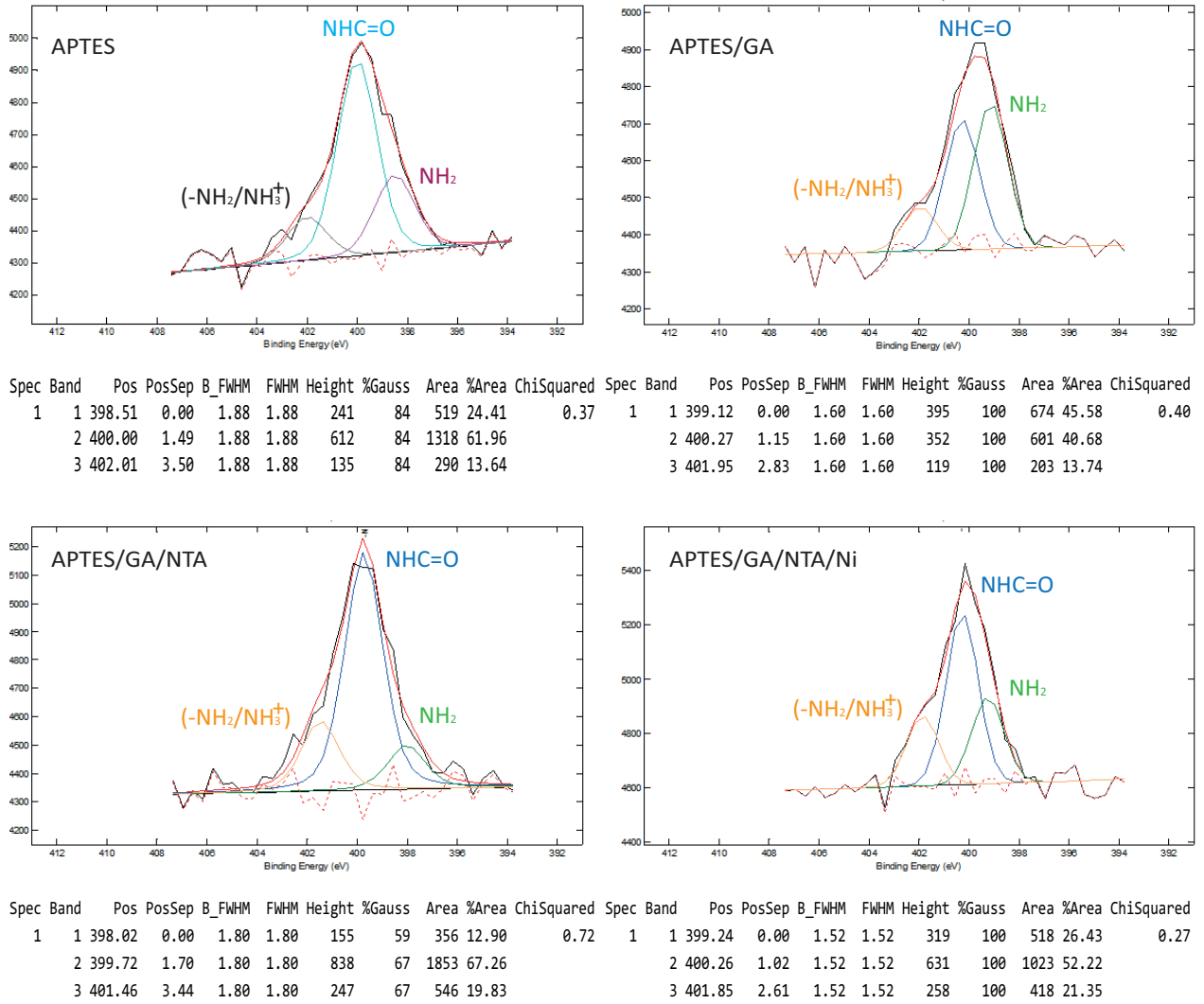
Figure A.2: N1s spectra determined from the surface of a flat Si sample at each stage of the surface modification, as described in Fig. 3.1 (a).

APTES

Spec	Band	Pos	PosSep	B_FWHM	FWHM	Height	%Gauss	Area	%Area	ChiSquared
1	1	398.51	0.00	1.88	1.88	241	84	519	24.41	0.37
	2	400.00	1.49	1.88	1.88	612	84	1318	61.96	
	3	402.01	3.50	1.88	1.88	135	84	290	13.64	

APTES/GA

Spec	Band	Pos	PosSep	B_FWHM	FWHM	Height	%Gauss	Area	%Area	ChiSquared
1	1	399.12	0.00	1.60	1.60	395	100	674	45.58	0.40
	2	400.27	1.15	1.60	1.60	352	100	601	40.68	
	3	401.95	2.83	1.60	1.60	119	100	203	13.74	

APTES/GA/NTA

Spec	Band	Pos	PosSep	B_FWHM	FWHM	Height	%Gauss	Area	%Area	ChiSquared
1	1	398.02	0.00	1.80	1.80	155	59	356	12.90	0.72
	2	399.72	1.70	1.80	1.80	838	67	1853	67.26	
	3	401.46	3.44	1.80	1.80	247	67	546	19.83	

APTES/GA/NTA/Ni

Spec	Band	Pos	PosSep	B_FWHM	FWHM	Height	%Gauss	Area	%Area	ChiSquared
1	1	399.24	0.00	1.52	1.52	319	100	518	26.43	0.27
	2	400.26	1.02	1.52	1.52	631	100	1023	52.22	
	3	401.85	2.61	1.52	1.52	258	100	418	21.35	

Table A.2: Element spectra scans on C, N, O, Si, S and Ni (At. %) are measured from the Si wafer samples for surface (Fig. 3.2 (b)) after each modification stage.

Element	Stage I	Stage II	Stage III	Stage IV
C	17.0 ± 3.3	12.5 ± 2.2	16.0 ± 3.9	24.4 ± 3.9
N	0.8 ± 0.4	0.9 ± 0.2	1.0 ± 0.3	1.3 ± 0.5
O	55.5 ± 2.8	58.8 ± 1.6	56.3 ± 2.7	50.0 ± 2.9
Si	26.7 ± 0.9	27.8 ± 0.8	26.8 ± 1.5	25.9 ± 1.4
S	—	10.2 ± 1.5	5.6 ± 1.7	3.7 ± 0.6
Ni	—	—	—	$0^{\dagger}$

† Traces of Ni are found but considered insignificant, as the measured values are close to the limit of detection.

Spec	Band	Pos	PosSep	B_FWHM	FWHM	Height	%Gauss	Area	%Area	ChiSquared	Spec	Band	Pos	PosSep	B_FWHM	FWHM	Height	%Gauss	Area	%Area	ChiSquared
1	1	284.79	0.00	1.85	1.85	9624	95	19377	81.80	0.85	1	1	284.78	0.00	1.86	1.86	7194	82	15471	80.20	0.80
	2	286.57	1.79	1.85	1.85	1546	78	3360	14.18			2	286.53	1.75	1.86	1.86	1387	100	2750	14.25	
	3	288.39	3.61	1.85	1.85	483	100	951	4.01			3	288.53	3.75	1.86	1.86	513	89	1071	5.55	

Spec	Band	Pos	PosSep	B_FWHM	FWHM	Height	%Gauss	Area	%Area	ChiSquared	Spec	Band	Pos	PosSep	B_FWHM	FWHM	Height	%Gauss	Area	%Area	ChiSquared
1	1	284.85	0.00	1.87	1.87	9306	86	19793	81.69	1.04	1	1	284.83	0.00	1.73	1.73	14479	82	29024	82.72	0.83
	2	286.73	1.88	1.87	1.87	1651	100	3290	13.58			2	286.56	1.73	1.73	1.73	2418	100	4457	12.70	
	3	288.87	4.02	1.87	1.87	572	99	1147	4.73			3	288.68	3.85	1.73	1.73	871	100	1606	4.58	

Figure A.3: C1s elemental spectra determined from the surface of a flat Si sample at each stage of the surface modification shown in Fig. 3.1 (b).

Table A.3: Element spectra scans on C, N, O, Si and Ni (At. %) are measured from the Si wafer samples for surface (Fig. 3.1 (c)) after each modification stage.

Element	Stage I	Stage II	Stage III	Stage IV
C	14.4 ± 0.9	25.4 ± 4.9	25.8 ± 6.9	31.1 ± 3.2
N	2.1 ± 0.1	2.5 ± 0.9	3.2 ± 0.9	2.4 ± 0.8
O	56.6 ± 0.7	49.1 ± 3.9	48.6 ± 5.3	45.4 ± 1.9
Si	26.7 ± 0.1	23.1 ± 1.9	22.4 ± 2.6	10.8 ± 2.3
Ni	—	—	—	0.3 ± 0.2

APTES

Spec	Band	Pos	PosSep	B_FWHM	FWHM	Height	%Gauss	Area	%Area	ChiSquared
1	1	398.51	0.00	1.88	1.88	241	84	519	24.41	0.37
	2	400.00	1.49	1.88	1.88	612	84	1318	61.96	
	3	402.01	3.50	1.88	1.88	135	84	290	13.64	

APTES/DITC

Spec	Band	Pos	PosSep	B_FWHM	FWHM	Height	%Gauss	Area	%Area	ChiSquared
1	1	398.15	0.00	1.89	1.89	267	84	579	28.38	0.36
	2	399.63	1.48	1.89	1.89	580	100	1166	57.18	
	3	401.45	3.30	1.89	1.89	146	100	294	14.44	

APTES/DITC/NTA

Spec	Band	Pos	PosSep	B_FWHM	FWHM	Height	%Gauss	Area	%Area	ChiSquared
1	1	398.37	0.00	1.60	1.60	165	43	356	14.74	0.56
	2	399.75	1.38	1.60	1.60	709	51	1484	61.49	
	3	401.13	2.76	1.60	1.60	274	51	574	23.77	

APTES/DITC/NTA/Ni

Spec	Band	Pos	PosSep	B_FWHM	FWHM	Height	%Gauss	Area	%Area	ChiSquared
1	1	399.70	0.00	1.84	1.84	770	84	1629	65.17	0.40
	2	400.71	1.01	1.84	1.84	292	92	596	23.83	
	3	402.30	2.60	1.84	1.84	135	92	275	11.00	

Figure A.4: N1s spectra determined from the surface of a flat Si sample at each stage of the surface modification shown in Fig. 3.1 (b).

Table A.4: Element spectra scans on C, N, O, Si, S and Ni (At. %) are measured from the Si wafer samples for surface (Fig. 3.1 (d)) after each modification stage.

Element	Stage I	Stage II	Stage III	Stage IV
C	14.4 ± 0.9	13.9 ± 1.3	26.9 ± 4.2	39.9 ± 3.6
N	2.1 ± 0.1	1.8 ± 0.4	2.8 ± 0.8	4.2 ± 0.4
O	56.6 ± 0.7	57.3 ± 1.1	47.4 ± 3.5	38.1 ± 2.7
Si	26.7 ± 0.1	27.0 ± 0.5	22.9 ± 1.5	17.6 ± 1.1
S	—	6.0 ± 0.4	3.7 ± 1.0	2.7 ± 0.4
Ni	—	—	—	$0^{\dagger}$

† Traces of Ni are found but considered insignificant, as the measured values are close to the limit of detection.

TMSPEDA

TMSPEDA/GA

Spec	Band	Pos	PosSep	B_FWHM	FWHM	Height	%Gauss	Area	%Area	ChiSquared	Spec	Band	Pos	PosSep	B_FWHM	FWHM	Height	%Gauss	Area	%Area	ChiSquared
1	1	284.71	0.00	1.88	1.88	7116	97	14458	69.42	0.80	1	1	284.80	0.00	1.90	1.90	12258	91	25839	71.13	1.11
	2	286.35	1.64	1.88	1.88	2254	90	4727	22.70			2	286.39	1.59	1.90	1.90	3266	84	7135	19.64	
	3	288.18	3.47	1.88	1.88	765	85	1641	7.88			3	288.11	3.31	1.90	1.90	1478	75	3352	9.23	

TMSPEDA/GA/NTA

TMSPEDA/GA/NTA/Ni

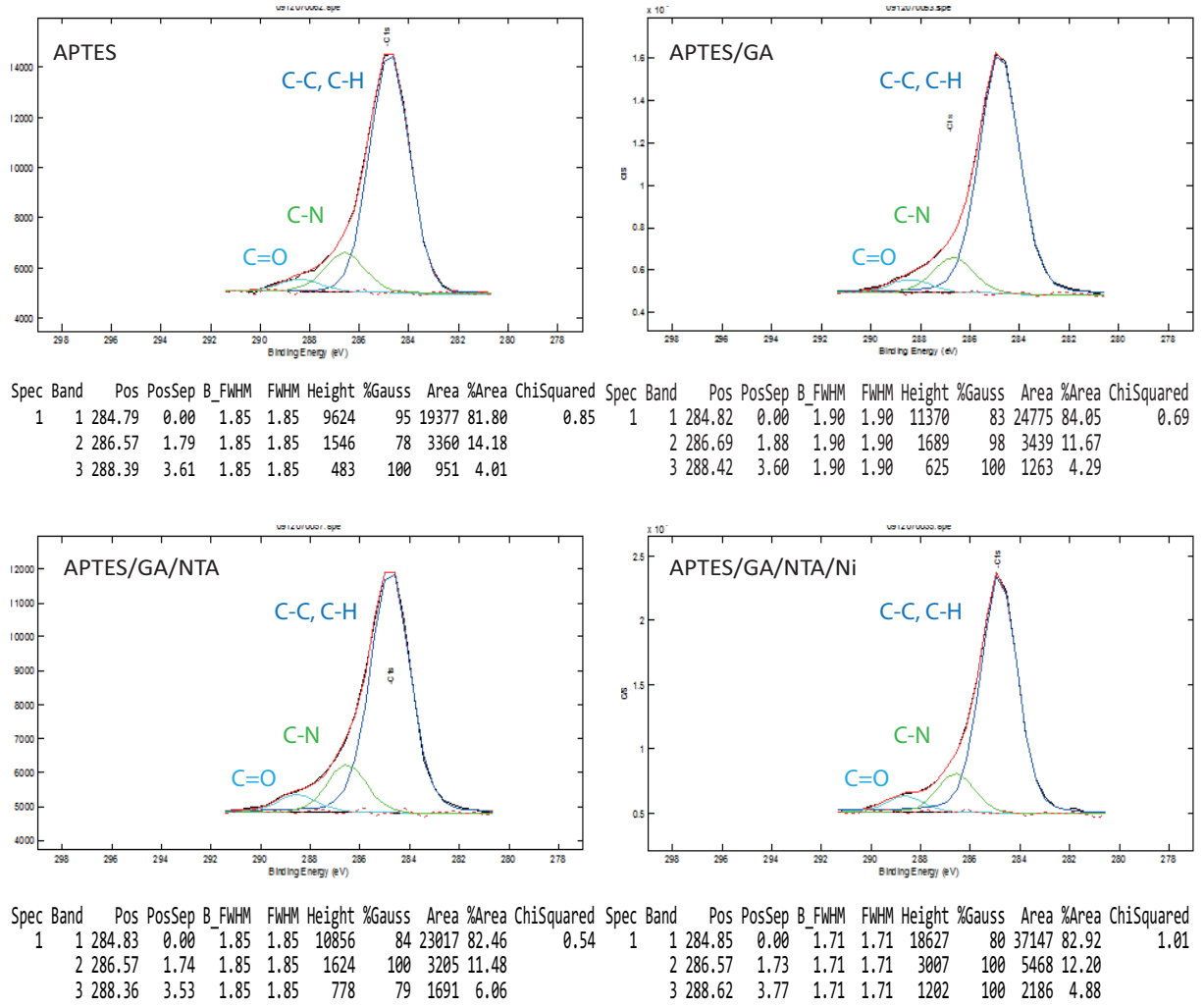| Spec	Band	Pos	PosSep	B_FWHM	FWHM	Height	%Gauss	Area	%Area	ChiSquared	Spec	Band	Pos	PosSep	B_FWHM	FWHM	Height	%Gauss	Area	%Area	ChiSquared
1	1	284.70	0.00	1.97	1.97	11350	88	25116	69.35	0.91	1	1	284.81	0.00	1.87	1.87	16165	83	34827	79.98	0.63
	2	286.28	1.59	1.97	1.97	3727	90	8187	22.61			2	286.40	1.59	1.87	1.87	3133	100	6242	14.33	
	3	288.13	3.43	1.97	1.97	1390	100	2912	8.04			3	288.15	3.34	1.87	1.87	1243	100	2477	5.69	

Figure A.5: C1s spectra determined from the surface of a flat Si sample at each stage of the surface modification shown in Fig. 3.1 (c).

Table A.5: Element spectra scans on C, N, O, Si and Ni (At. %) are measured from the Si wafer samples for surface (Fig. 3.1 (e)) after each modification stage.

Element	Stage I	Stage II	Stage III	Stage IV
C	15.9 ± 1.0	18.6 ± 3.4	17.7 ± 0.7	26.4 ± 1.4
N	0.6 ± 0.1	0.6 ± 0.1	0.9 ± 0.2	1.2 ± 0.1
O	56.8 ± 0.7	55.2 ± 2.4	55.6 ± 0.5	49.1 ± 1.0
Si	26.2 ± 0.5	25.6 ± 1.1	25.9 ± 0.4	23.1 ± 0.5
Ni	—	—	—	$0^{\dagger}$

† Traces of Ni are found but considered insignificant, as the measured values are close to the limit of detection.

```
        TMSPEDA                           TMSPEDA/GA

Spec Band    Pos PosSep B_FWHM  FWHM Height %Gauss  Area %Area ChiSquared   Spec Band    Pos PosSep B_FWHM  FWHM Height %Gauss  Area %Area ChiSquared
  1    1 399.02   0.00   2.02   2.02    700     51  1859 35.36       0.51      1    1 398.76   0.00   2.09   2.09    495     76  1227 21.46       0.55
       2 400.22   1.20   2.02   2.02   1265     80  2986 56.81                      2 400.02   1.25   2.09   2.09   1735     89  4060 71.03
       3 401.52   2.50   2.02   2.02    191    100   412  7.84                      3 401.72   2.95   2.09   2.09    193    100   429  7.51
```



```
        TMSPEDA/GA/NTA                      TMSPEDA/GA/NTA/Ni

Spec Band    Pos PosSep B_FWHM  FWHM Height %Gauss  Area %Area ChiSquared   Spec Band    Pos PosSep B_FWHM  FWHM Height %Gauss  Area %Area ChiSquared
  1    1 398.74   0.00   1.83   1.83    862     43  2127 28.60       0.43      1    1 398.79   0.00   1.83   1.83    634     76  1376 28.36       0.53
       2 399.86   1.12   1.83   1.83   1992     80  4245 57.06                      2 400.03   1.24   1.83   1.83   1459     96  2888 59.55
       3 401.23   2.50   1.83   1.83    492     76  1067 14.34                      3 401.35   2.56   1.83   1.83    290     92   586 12.08
```
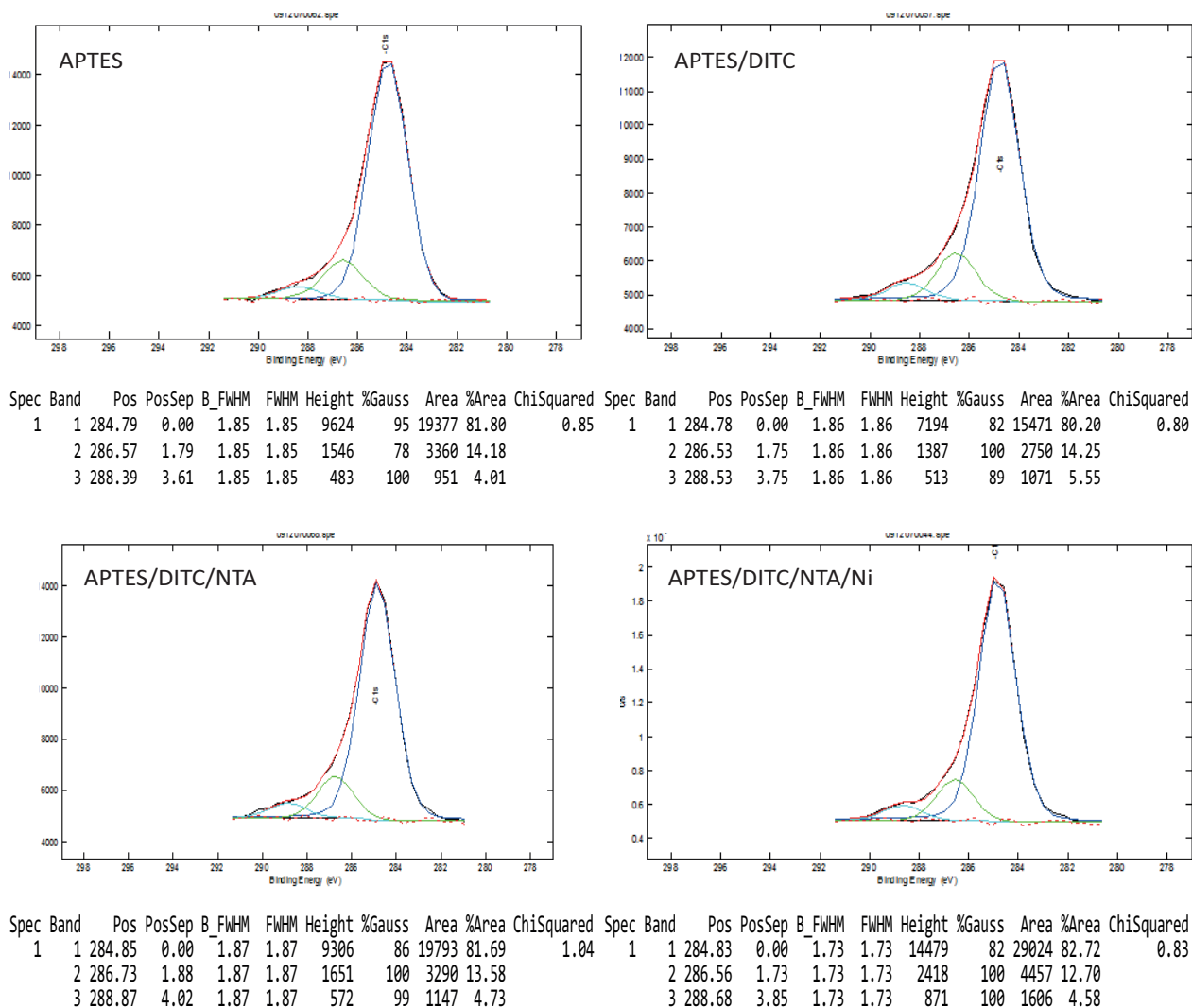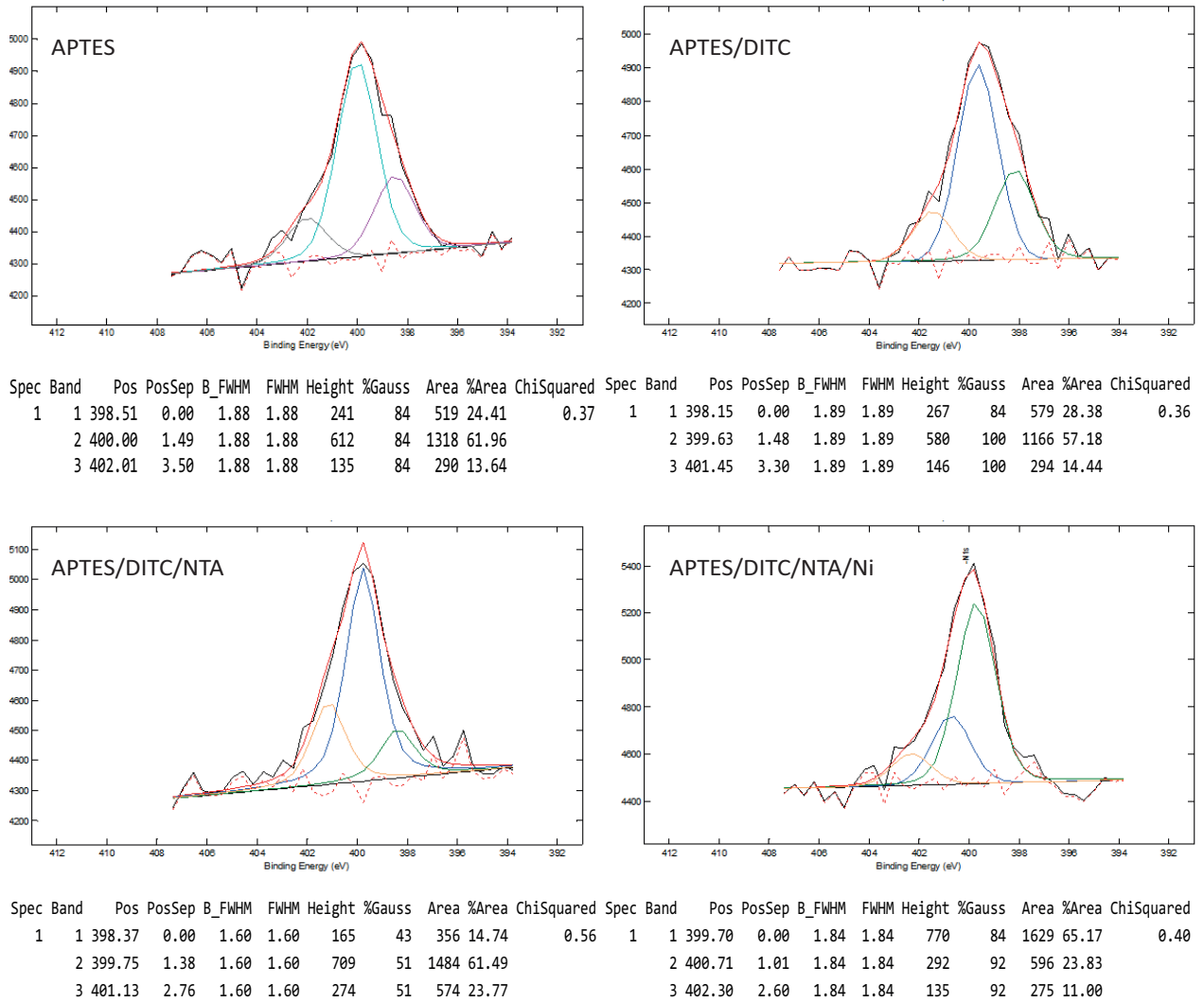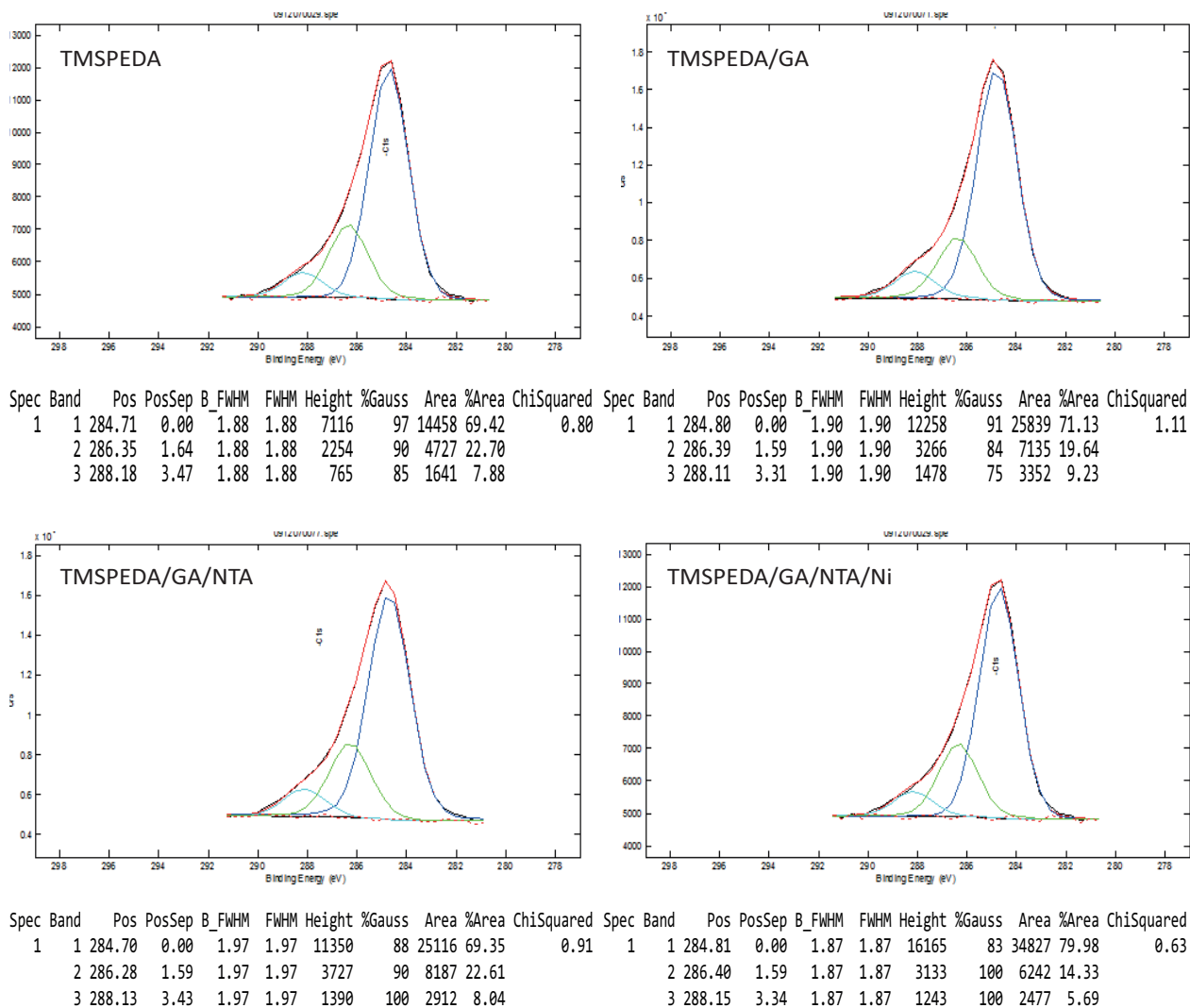
Figure A.6: N1s spectra determined from the surface of a flat Si sample at each stage of the surface modification, as shown in Fig. 3.1 (c).

Table A.6: Element spectra scans on C, N, O, Si, S and Ni (At. %) are measured from the Si wafer samples for surface (Fig. 3.1 (f)) after each modification stage.

Element	Stage I	Stage II	Stage III	Stage IV
C	15.9 ± 1.0	9.8 ± 2.3	13.7 ± 2.7	28.2 ± 8.0
N	0.6 ± 0.1	0.5 ± 0.2	0.8 ± 0.3	1.3 ± 0.6
O	56.8 ± 0.7	61.5 ± 1.7	58.5 ± 2.2	48.4 ± 6.2
Si	26.2 ± 0.5	28.2 ± 0.8	27.7 ± 0.8	22.2 ± 2.3
S	—	9.3 ± 1.8	7.0 ± 1.4	5.1 ± 1.8
Ni	—	—	—	$0^\dagger$

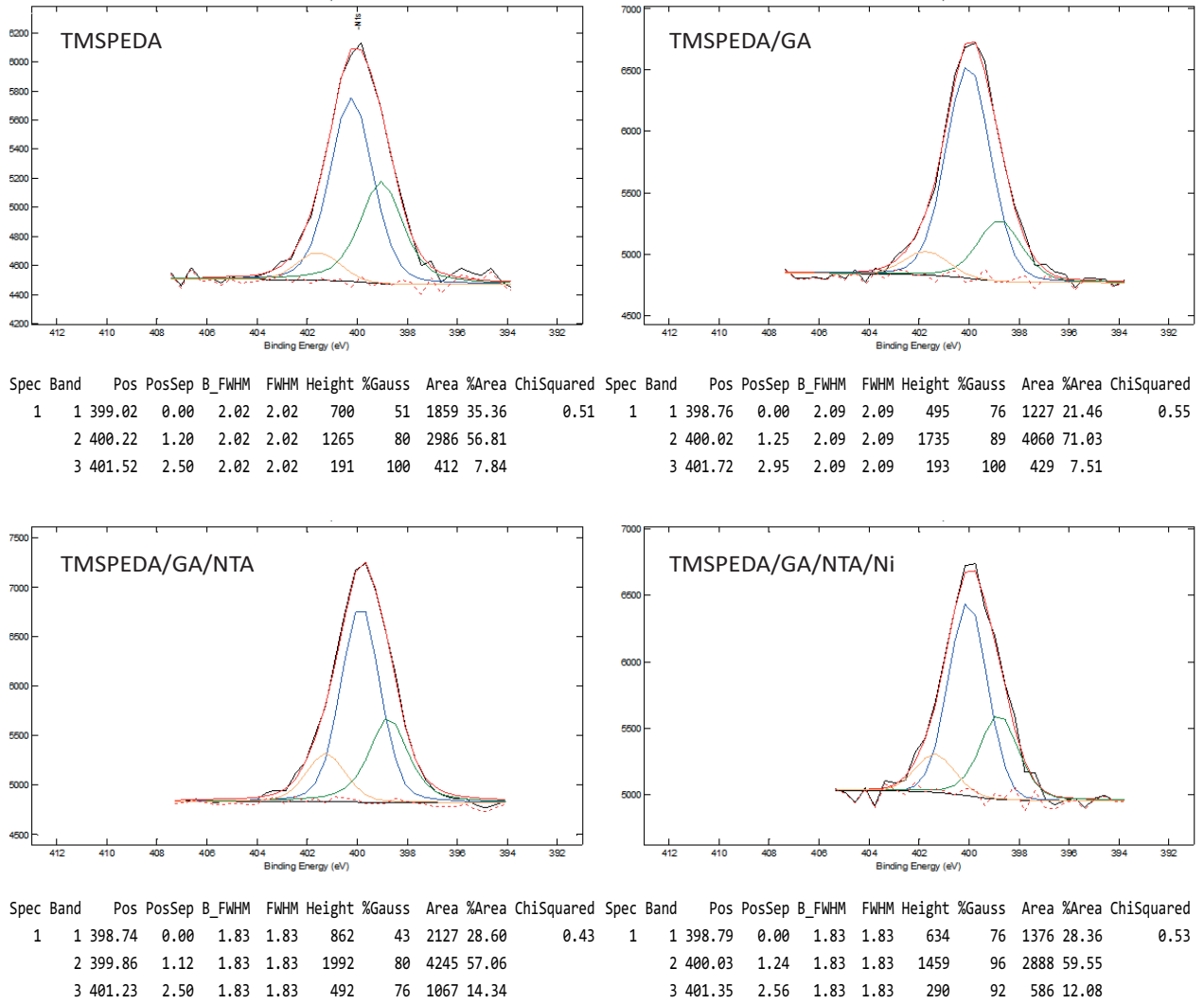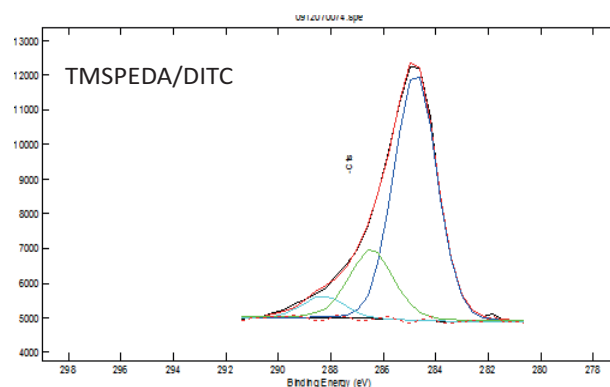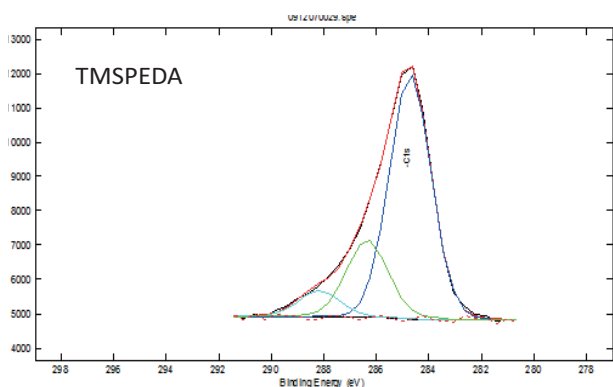† Traces of Ni are found but considered insignificant, as the measured values are close to the limit of detection.

Spec	Band	Pos	PosSep	B_FWHM	FWHM	Height	%Gauss	Area	%Area	ChiSquared
1	1	284.71	0.00	1.88	1.88	7116	97	14458	69.42	0.80
	2	286.35	1.64	1.88	1.88	2254	90	4727	22.70	
	3	288.18	3.47	1.88	1.88	765	85	1641	7.88	

Spec	Band	Pos	PosSep	B_FWHM	FWHM	Height	%Gauss	Area	%Area	ChiSquared
1	1	284.77	0.00	1.93	1.93	7197	94	15215	71.35	0.71
	2	286.45	1.68	1.93	1.93	2039	73	4729	22.18	
	3	288.29	3.52	1.93	1.93	639	89	1380	6.47	
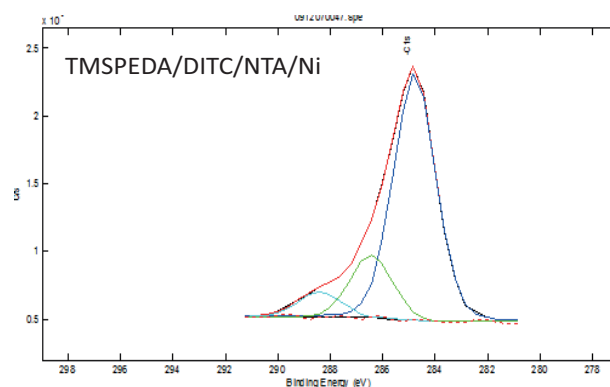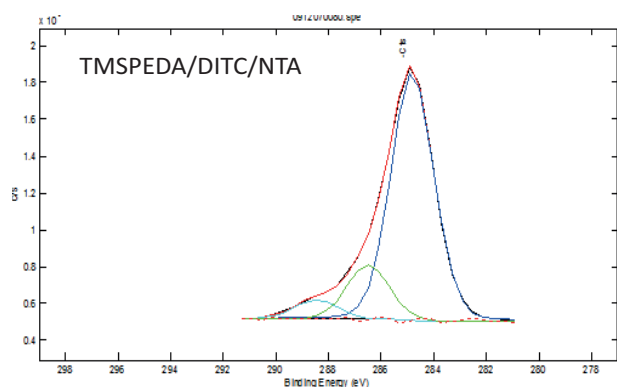
Spec	Band	Pos	PosSep	B_FWHM	FWHM	Height	%Gauss	Area	%Area	ChiSquared
1	1	284.80	0.00	1.91	1.91	13481	91	28609	78.06	0.83
	2	286.50	1.70	1.91	1.91	2923	100	5950	16.23	
	3	288.46	3.66	1.91	1.91	1027	100	2091	5.70	

Spec	Band	Pos	PosSep	B_FWHM	FWHM	Height	%Gauss	Area	%Area	ChiSquared
1	1	284.79	0.00	1.90	1.90	18162	88	38813	74.75	0.90
	2	286.46	1.67	1.90	1.90	4645	100	9376	18.06	
	3	288.42	3.63	1.90	1.90	1850	100	3735	7.19	

Figure A.7: C1s spectra determined from the surface of a flat Si sample at each stage of the surface modification, described earlier in Fig. 3.1 (d).

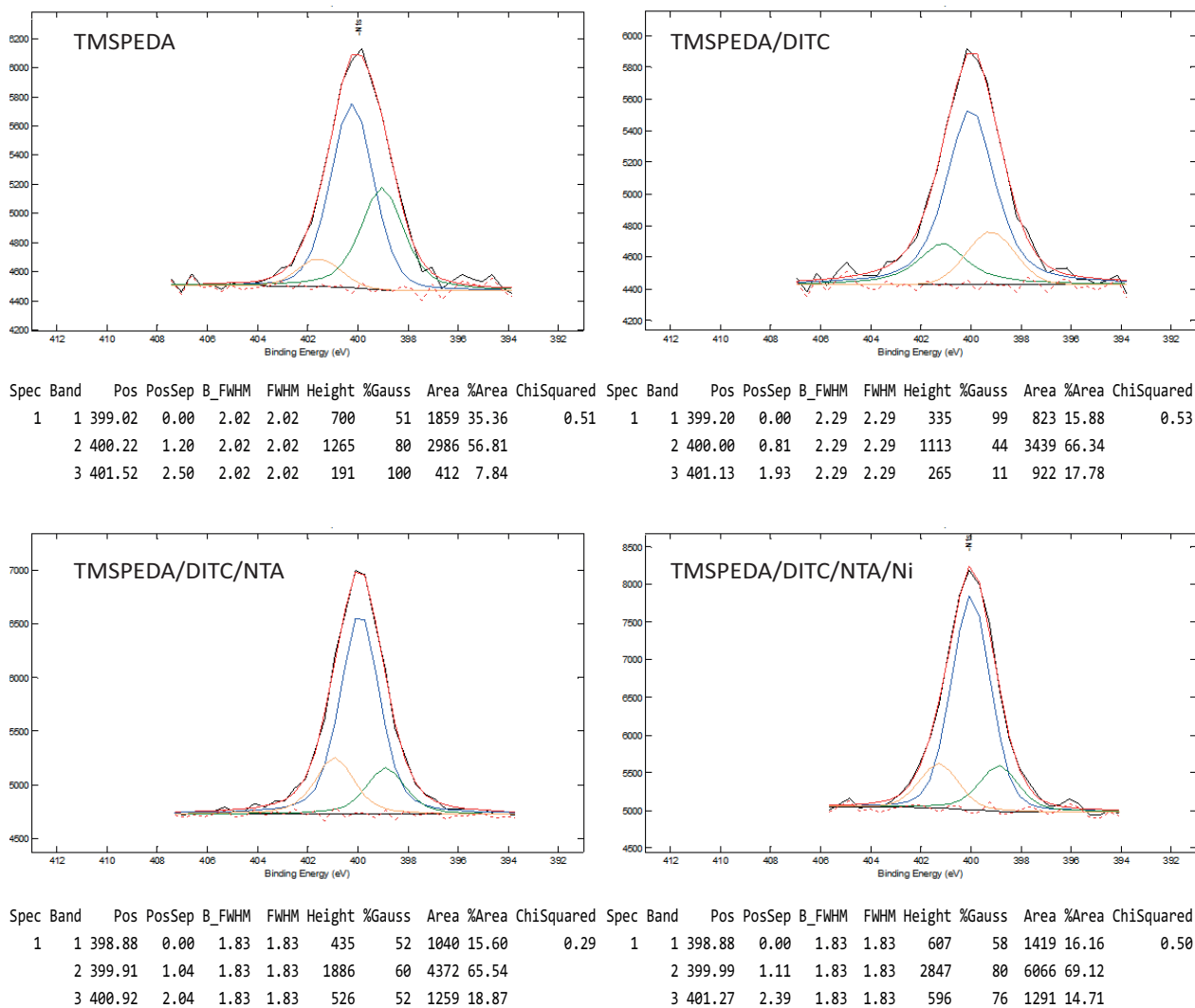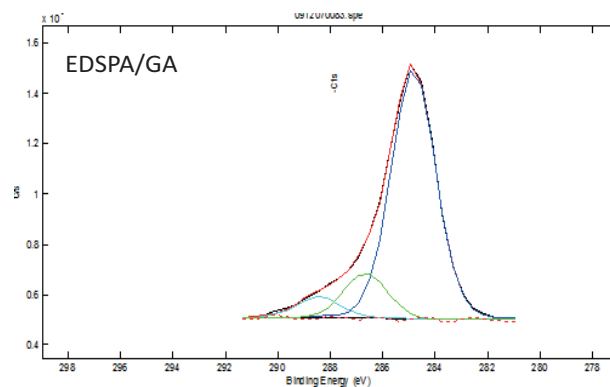| Spec	Band		Pos	PosSep	B_FWHM	FWHM	Height	%Gauss	Area	%Area	ChiSquared
1	1	399.02	0.00	2.02	2.02	700	51	1859	35.36	0.51
	2	400.22	1.20	2.02	2.02	1265	80	2986	56.81	
	3	401.52	2.50	2.02	2.02	191	100	412	7.84	

Spec	Band		Pos	PosSep	B_FWHM	FWHM	Height	%Gauss	Area	%Area	ChiSquared
1	1	399.20	0.00	2.29	2.29	335	99	823	15.88	0.53
	2	400.00	0.81	2.29	2.29	1113	44	3439	66.34	
	3	401.13	1.93	2.29	2.29	265	11	922	17.78	

Spec	Band		Pos	PosSep	B_FWHM	FWHM	Height	%Gauss	Area	%Area	ChiSquared
1	1	398.88	0.00	1.83	1.83	435	52	1040	15.60	0.29
	2	399.91	1.04	1.83	1.83	1886	60	4372	65.54	
	3	400.92	2.04	1.83	1.83	526	52	1259	18.87	

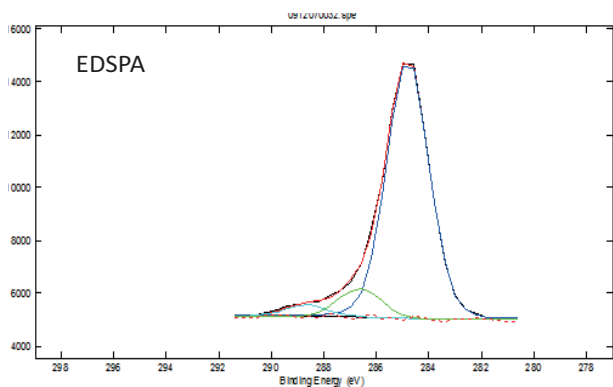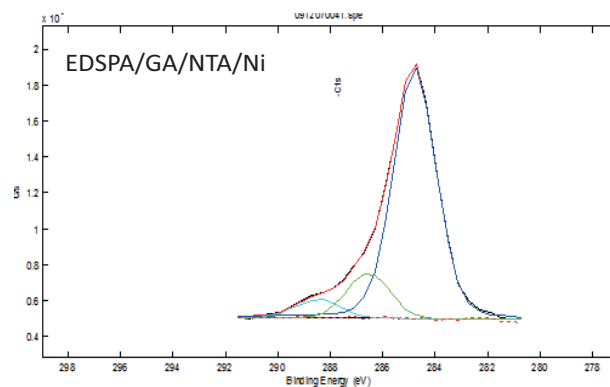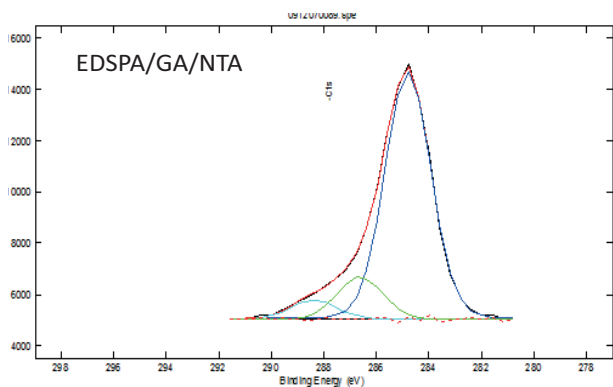| Spec	Band		Pos	PosSep	B_FWHM	FWHM	Height	%Gauss	Area	%Area	ChiSquared
1	1	398.88	0.00	1.83	1.83	607	58	1419	16.16	0.50
	2	399.99	1.11	1.83	1.83	2847	80	6066	69.12	
	3	401.27	2.39	1.83	1.83	596	76	1291	14.71	

Figure A.8: N1s spectra determined from the surface of a flat Si sample at each stage of the surface modification shown in Fig. 3.1 (d).

Spec	Band	Pos	PosSep	B_FWHM	FWHM	Height	%Gauss	Area	%Area	ChiSquared
1	1	284.80	0.00	1.88	1.88	9845	89	20685	87.11	0.56
	2	286.64	1.84	1.88	1.88	1088	100	2173	9.15	
	3	288.73	3.93	1.88	1.88	444	100	888	3.74	

Spec	Band	Pos	PosSep	B_FWHM	FWHM	Height	%Gauss	Area	%Area	ChiSquared
1	1	284.82	0.00	1.99	1.99	9926	90	22083	79.39	0.64
	2	286.67	1.84	1.99	1.99	1786	100	3788	13.62	
	3	288.47	3.65	1.99	1.99	836	80	1943	6.99	

Spec	Band	Pos	PosSep	B_FWHM	FWHM	Height	%Gauss	Area	%Area	ChiSquared
1	1	284.79	0.00	2.05	2.05	9678	92	21967	80.78	0.56
	2	286.63	1.84	2.05	2.05	1645	100	3596	13.22	
	3	288.40	3.61	2.05	2.05	743	99	1631	6.00	

Spec	Band	Pos	PosSep	B_FWHM	FWHM	Height	%Gauss	Area	%Area	ChiSquared
1	1	284.76	0.00	1.92	1.92	13985	82	30998	81.15	0.63
	2	286.56	1.80	1.92	1.92	2503	100	5116	13.39	
	3	288.50	3.73	1.92	1.92	1021	100	2086	5.46	

Figure A.9: C1s spectra determined from the surface of a flat Si sample at each stage of the surface modification, as shown in Fig. 3.1 (e).

Spec	Band	Pos	PosSep	B_FWHM	FWHM	Height	%Gauss	Area	%Area	ChiSquared
1	1	398.91	0.00	1.83	1.83	215	52	514	34.70	0.71
	2	400.27	1.36	1.83	1.83	359	100	699	47.20	
	3	402.11	3.21	1.83	1.83	119	68	268	18.10	

Spec	Band	Pos	PosSep	B_FWHM	FWHM	Height	%Gauss	Area	%Area	ChiSquared
1	1	399.42	0.00	1.83	1.83	366	84	766	59.28	0.47
	2	400.97	1.55	1.83	1.83	214	100	416	32.23	
	3	402.52	3.10	1.83	1.83	56	100	110	8.50	
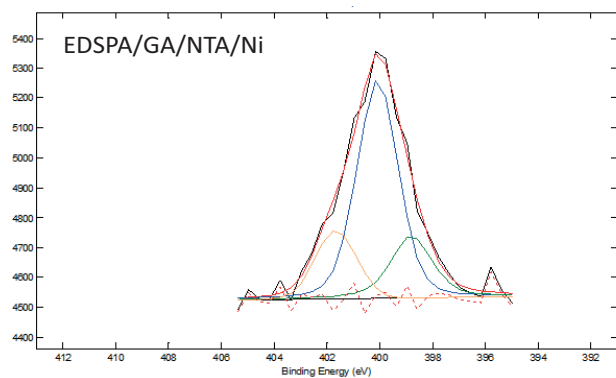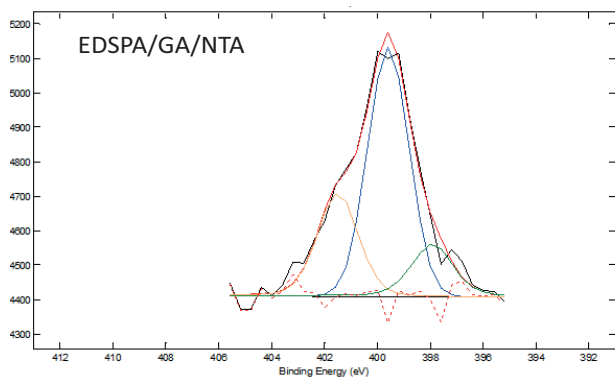
Spec	Band	Pos	PosSep	B_FWHM	FWHM	Height	%Gauss	Area	%Area	ChiSquared
1	1	397.92	0.00	1.83	1.83	154	68	345	14.53	0.47
	2	399.57	1.66	1.83	1.83	724	100	1408	59.25	
	3	401.49	3.57	1.83	1.83	297	84	623	26.22	

Spec	Band	Pos	PosSep	B_FWHM	FWHM	Height	%Gauss	Area	%Area	ChiSquared
1	1	398.79	0.00	1.83	1.83	209	52	500	19.66	0.23
	2	400.07	1.28	1.83	1.83	734	76	1593	62.70	
	3	401.65	2.87	1.83	1.83	230	100	448	17.63	

Figure A.10: N1s spectra determined from the surface of a flat Si sample at each stage of the surface modification shown in Fig. 3.1 (e).

Spec	Band	Pos	PosSep	B_FWHM	FWHM	Height	%Gauss	Area	%Area	ChiSquared
1	1	284.80	0.00	1.88	1.88	9845	89	20685	87.11	0.56
	2	286.64	1.84	1.88	1.88	1088	100	2173	9.15	
	3	288.73	3.93	1.88	1.88	444	100	888	3.74	

Spec	Band	Pos	PosSep	B_FWHM	FWHM	Height	%Gauss	Area	%Area	ChiSquared
1	1	284.82	0.00	1.94	1.94	5768	87	12642	82.37	0.52
	2	286.61	1.79	1.94	1.94	977	100	2018	13.15	
	3	288.35	3.53	1.94	1.94	318	90	688	4.48	
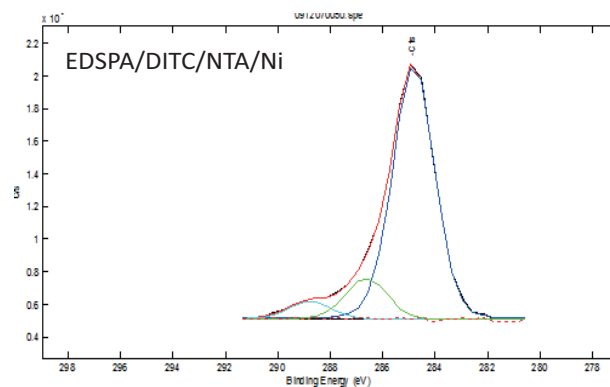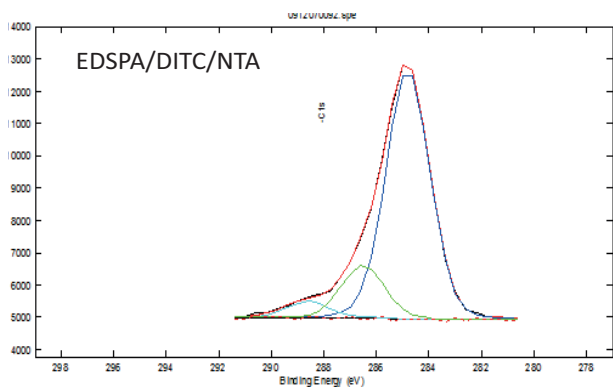
Spec	Band	Pos	PosSep	B_FWHM	FWHM	Height	%Gauss	Area	%Area	ChiSquared
1	1	284.79	0.00	1.94	1.94	7779	91	16740	77.87	0.36
	2	286.51	1.71	1.94	1.94	1633	88	3565	16.58	
	3	288.64	3.85	1.94	1.94	506	70	1193	5.55	

Spec	Band	Pos	PosSep	B_FWHM	FWHM	Height	%Gauss	Area	%Area	ChiSquared
1	1	284.83	0.00	1.86	1.86	15508	90	32238	82.20	0.59
	2	286.64	1.81	1.86	1.86	2476	100	4910	12.52	
	3	288.78	3.95	1.86	1.86	1044	100	2070	5.28	

Figure A.11: C1s spectra determined from the surface of a flat Si sample at each stage of the surface modification, presented in Fig. 3.1 (f).

Figure A.12: N1s spectra determined from the surface of a flat Si sample at each stage of the surface modification, as demonstrated in Fig. 3.1 (f).

Spec	Band	Pos	PosSep	B_FWHM	FWHM	Height	%Gauss	Area	%Area	ChiSquared
1	1	398.91	0.00	1.83	1.83	215	52	514	34.70	0.71
	2	400.27	1.36	1.83	1.83	359	100	699	47.20	
	3	402.11	3.21	1.83	1.83	119	68	268	18.10	

Spec	Band	Pos	PosSep	B_FWHM	FWHM	Height	%Gauss	Area	%Area	ChiSquared
1	1	398.34	0.00	1.83	1.83	78	76	170	12.51	0.44
	2	399.84	1.49	1.83	1.83	446	100	869	63.95	
	3	401.53	3.19	1.83	1.83	164	100	320	23.54	
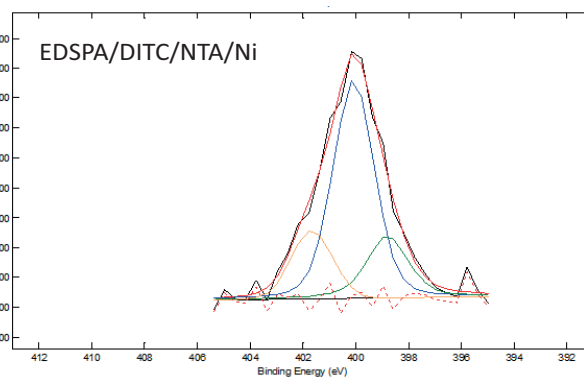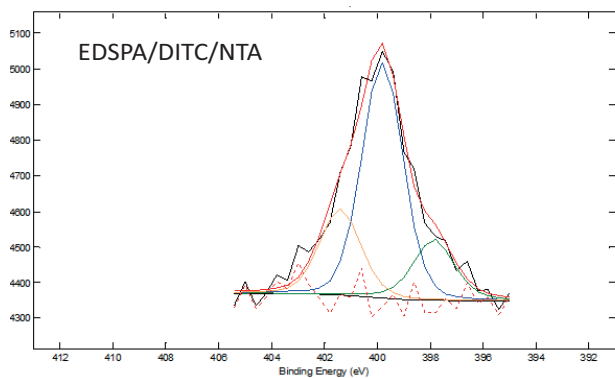
Spec	Band	Pos	PosSep	B_FWHM	FWHM	Height	%Gauss	Area	%Area	ChiSquared
1	1	397.85	0.00	1.83	1.83	171	60	397	17.18	0.68
	2	399.79	1.94	1.83	1.83	662	84	1388	59.99	
	3	401.39	3.54	1.83	1.83	243	76	528	22.83	

Spec	Band	Pos	PosSep	B_FWHM	FWHM	Height	%Gauss	Area	%Area	ChiSquared
1	1	398.79	0.00	1.83	1.83	209	52	500	19.66	0.23
	2	400.07	1.28	1.83	1.83	734	76	1593	62.70	
	3	401.65	2.87	1.83	1.83	230	100	448	17.63	

Appendix B

Numerical simulation code

```
function [t,x,y,z] = Sys3ODEsRK4(a, b, h, x1, y1, z1)
```

%This MATLab function, Sys3ODEsRK4, will answer most of your questions, if they are somehow related to solving a system of three first-order initial values ODEs using fourth-order Runge-Kuta method.
%The independent variable is t, and the dependent variables are x, y and z
%Input variables:
%ODE1 Name for the function that calculates dx/dt.
%ODE2 Name for the function that calculates dy/dt.
%ODE3 Name for the function that calculates dz/dt.
%a The first value of t.
%b The last value of t.
%h Size of a increment.
%x1 The initial value of x.
%y1 The initial value of y.
%z1 The initial value of z.
%Output variables:
%t A vector with the coordinates of the solution points.
%x A vector with the x coordinate of the solution points.
%y A vector with the y coordinate of the solution points.
%z A vector with the z coordinate of the solution points.

```
prompt={'Enter the Kf:',...
'Enter the Kb:',...
'Enter the Kr'};
name='Input free parameters';
numlines=1;
```

```matlab
defaultanswer={'0.2', '4.3', '20'}; %defines initial values
answer=inputdlg(prompt,name,numlines,defaultanswer); %allows to change the variables through
"user-friendly interface".

global Kf; Kf = str2double(answer1);fprintf('Kf= %5.4f\n',Kf); %the variables resulting from the
input dialog are transformed from str2double.
global Kb; Kb = str2double(answer2);fprintf('Kb= %5.4f\n',Kb); %IMPORTANTLY, they must be
declared as global variables so they could be reached
global Kr; Kr = str2double(answer3);fprintf('Kr= %5.4f\n',Kr); % from a function which is not
nested in the main function (outside function).
global Fad; Fad = 0.34;fprintf('Fad= %5.4f\n',Fad); %Coefficients determined from the experimental
data: for the adsorption, Fad;
global Kdeg; Kdeg = 1.017;fprintf('Kdeg= %5.4f\n',Kdeg); % E deactivation, Kdeg.


%ODE1 = @(t,x,y,z) -(Kr*x*(Kdeg*z))/((Kb+Kr)/Kf + x);
ODE1 = @SubstrateDienol; %handle of the function SubstrateDienol with a name ODE1
function dxdt = SubstrateDienol(t,x,y,z) % defines the function with its input arguments the same
as for the function Sys3ODEsRK4
dxdt = - (Kr*x*(Kdeg*z))/((Kb+Kr)/Kf + x); %relates the diff eq. with the function.
end
ODE2 = @(t,x,y,z) Fad*(Kr*x*(Kdeg*z))/((Kb+Kr)/Kf + x); %another option is to use anonymous
function to describe the diff. eq.
% function dxdt = ProductDienOAc(t,x,y,z)
% dxdt = Fad*(Kr*x*(Kdeg*z))/((Kb+Kr)/Kf + x);
% end


ODE3 = @(t,x,y,z) -Kdeg*z;
% function dzdt = EnzymeDegrad(t,x,y,z)
% dzdt = -Kdeg*z;
% x is the [S]; and z is the [E]
% end


t(1) = a; x(1) = x1; y(1) = y1; z(1) = z1;
n = (b - a)/h;
for i = 1:n
t(i+1) = t(i) + h;
tm = t(i) + h/2;
```
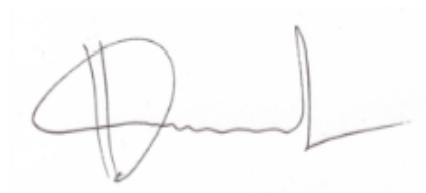
```
Kx1 = ODE1(t(i), x(i), y(i), z(i));
Ky1 = ODE2(t(i), x(i), y(i), z(i));
Kz1 = ODE3(t(i), x(i), y(i), z(i));
Kx2 = ODE1(tm, x(i)+Kx1*h/2, y(i)+Ky1*h/2, z(i)+Kz1*h/2);
Ky2 = ODE2(tm, x(i)+Kx1*h/2, y(i)+Ky1*h/2, z(i)+Kz1*h/2);
Kz2 = ODE3(tm, x(i)+Kx1*h/2, y(i)+Ky1*h/2, z(i)+Kz1*h/2);
Kx3 = ODE1(tm, x(i)+Kx2*h/2, y(i)+Ky2*h/2, z(i)+Kz2*h/2);
Ky3 = ODE2(tm, x(i)+Kx2*h/2, y(i)+Ky2*h/2, z(i)+Kz2*h/2);
Kz3 = ODE3(tm, x(i)+Kx2*h/2, y(i)+Ky2*h/2, z(i)+Kz2*h/2);
Kx4 = ODE1(tm, x(i)+Kx3*h/2, y(i)+Ky3*h/2, z(i)+Kz3*h/2);
Ky4 = ODE2(tm, x(i)+Kx3*h/2, y(i)+Ky3*h/2, z(i)+Kz3*h/2);
Kz4 = ODE3(tm, x(i)+Kx3*h/2, y(i)+Ky3*h/2, z(i)+Kz3*h/2);
x(i+1) = x(i) + (Kx1 + 2*Kx2 + 2*Kx3 + Kx4)*h/6;
y(i+1) = y(i) + (Ky1 + 2*Ky2 + 2*Ky3 + Ky4)*h/6;
z(i+1) = z(i) + (Kz1 + 2*Kz2 + 2*Kz3 + Kz4)*h/6;
end
end
```

Declaration

I herewith declare that I have produced this paper without the prohibited assistance of third parties and without making use of aids other than those specified; notions taken over directly or indirectly from other sources have been identified as such. This paper has not previously been presented in identical or similar form to any other Dutch or foreign examination board.

The thesis work was conducted from 01-Jan-2008 to 31-Dec-2011 under the supervision of prof. Han J.G.E. Gardeniers at University of Twente.